INAUGURAL - DISSERTATION

zur

Erlangung der Doktorwürde

der

Gesamtfakultät für Mathematik,

Ingenieur- und Naturwissenschaften der

Ruprecht-Karls-Universität

Heidelberg

vorgelegt von

M.Sc. Zhaoping Ying

aus Ningde, China

Tag der mündlichen Prüfung: 05.11.2024

Numerical Simulation of Monocomponent and Multicomponent Droplet Spray Laminar Flames in the Counterflow Configuration

Gutachter: Prof. Dr. Oriol Vendrell

Prof. Dr. Ing. Andreas Kempf

To my forever beloved grandfather, may you rest peacefully in heaven.
Your memory continues to inspire and guide me every day.

Abstract

Spray combustion is crucial in numerous energy conversion systems, characterized by complex interactions among fluid dynamics, heat transfer, chemical kinetics, and phase transitions. Understanding these interactions is essential for enhancing combustion efficiency and minimizing pollutant emissions. Numerical studies on spray flames are important for improving our knowledge of these systems. The flamelet approach is advantageous for its efficient and precise separation of chemical processes from turbulence dynamics. Utilizing laminar spray flame structures in counterflow configurations is instrumental in establishing spray flamelet libraries that incorporate detailed chemical reaction mechanisms.

Research on numerical solutions for multiple flame structures in spray combustion, particularly under fuel-rich conditions, is limited but essential for developing comprehensive flamelet libraries. Additionally, the interaction and dynamics of heating and evaporation in multicomponent droplets within spray flames remain inadequately explored. Detailed investigations are essential for understanding systems like hydrous ethanol droplet sprays and titanium(IV) isopropoxide (TTIP)/*p*-xylene precursor solutions used in flame spray pyrolysis.

The research begins with an analysis of monocomponent ethanol spray flames under local fuel-rich conditions. In-depth results discussed include the observation of double and triple structures in ethanol spray flames under various conditions, employing regime diagrams to map their existence relative to initial gas strain rates, equivalence ratios, and droplet sizes. Double flame structures are observed for initial droplet radii larger than 30 μm, while triple flame structures emerge exclusively under conditions of initial droplet radii ranging from 10 μm to 30 μm. Particularly, a flame structure with distinct evaporation and combustion zones is identified. A comprehensive analysis of these flame structures is presented, exploring the stability and transition mechanisms under differing operational conditions. Notably, stable spray flame structures with two chemical reaction zones are observed across all tested scenarios. The transition mechanisms among various spray flame structures underscore the critical interactions between energy-consuming vaporization processes, the positioning of droplets within the counterflow setup, and the exothermic nature of the chemical reactions involved.

A comprehensive numerical analysis of hydrous ethanol laminar spray flames is then conducted, comparing it with anhydrous counterparts. This analysis includes a validation of the extended multicomponent droplet spray flame model and an investigation of hydrous ethanol spray flame characteristics. Additionally, the study explores the multiple flame structures under identical conditions for hydrous ethanol sprays, highlighting the minor role of water content in the droplets on flame structure transitions.

Finally, a detailed investigation on TTIP/p-xylene spray flames explores the multicomponent heating, evaporation, and motion of the droplets, alongside thermal decomposition and the involved chemical reactions. A comparative analysis of pure p-xylene and TTIP/p-xylene spray flames indicates that p-xylene evaporates preferentially due to its higher volatility, thereby providing the necessary gaseous fuel for sustained combustion. In contrast, the thermal decomposition of TTIP which consumes energy essential for its phase change occurs in a relatively cooler zone, leading to a distinct separation of the reaction zones. The decomposition products of gaseous TTIP, notably C_3H_6 and CH_3, are primarily observed in the gas-sided flame zone. Multiple flame structures are identified during the simulations. Among these structures, the flame structure with a single reaction zone on the spray side exhibits the greatest stability as strain rates increase.

Zusammenfassung

Verbrennung von Sprays ist in zahlreichen Energieumwandlungssystemen von entscheidender Bedeutung und zeichnen sich durch komplexe Wechselwirkungen zwischen Strömungsdynamik, Wärmeübertragung, chemischer Kinetik und Phasenübergängen aus. Das Verständnis dieser Wechselwirkungen ist grundliegend, um die Verbrennungseffizienz zu verbessern und Schadstoffemissionen zu minimieren. Numerische Studien zu Sprayflammen sind wichtig, um unser Wissen über diese Systeme zu erweitern. Der Flamelet-Ansatz ist vorteilhaft aufgrund seiner effizienten und präzisen Trennung chemischer Prozesse von Turbulenzdynamiken. Die Nutzung laminarer Sprühflammenstrukturen in Gegenstromkonfigurationen ist entscheidend für die Erstellung von Sprühflamelet-Bibliotheken, die detaillierte chemische Reaktionsmechanismen enthalten.

Forschung zu numerischen Lösungen für mehrere Flammenstrukturen in der Verbrennung von Sprays, insbesondere unter brennstoffreichen Bedingungen, ist begrenzt, aber notwendig für die Entwicklung umfassender Bibliotheken von Flamelet-Ansätzen. Darüber hinaus sind die Wechselwirkungen und Dynamik von Erwärmung und Verdampfung in Mehrkomponententropfen innerhalb von Sprühflammen noch unzureichend erforscht. Detaillierte Untersuchungen sind unerlässlich, um Systeme wie hydratisierte Ethanol-Tropfensprays und Titanium(IV)-isopropoxid (TTIP)/p-Xylol-Präkursorgemische, die in der Flammensprühpyrolyse verwendet werden, zu verstehen.

Diese Forschung beginnt mit einer Analyse von einkomponentigen Ethanol-Sprühflammen unter lokalen, brennstoffreichen Bedingungen. In dieser Arbeit diskutierte Ergebnisse umfassen die Beobachtung von Doppel- und Dreifachstrukturen in Ethanol-Sprühflammen unter verschiedenen Bedingungen, wobei Stabilitätsdiagramme verwendet werden, um deren Existenz in Bezug auf anfängliche Gasdehnungsgeschwindigkeiten, Äquivalenzverhältnisse und Tröpfchengrößen zuzuordnen. Doppelte Flammenstrukturen werden bei anfänglichen Tropfenradien von mehr als 30 µm beobachtet, während dreifache Flammenstrukturen ausschließlich unter Bedingungen von Tropfenradien im Bereich von 10 µm bis 30 µm auftreten. Insbesondere wird eine Flammenstruktur mit getrennten Verdampfungs- und Verbrennungszonen identifiziert. Eine umfassende Studie dieser Flammenstrukturen, welche die Stabilität und Übergangsmechanismen unter verschiedenen Betriebsbedingungen untersucht, wird

präsentiert. Bemerkenswerterweise werden stabile Sprühflammenstrukturen mit zwei chemischen Reaktionszonen in allen getesteten Szenarien beobachtet. Die Übergangsmechanismen zwischen verschiedenen Sprühflammenstrukturen betonen die kritischen Wechselwirkungen zwischen energieverbrauchenden Verdampfungsprozessen, der Positionierung der Tropfen innerhalb der Gegenstromkonfiguration und der exothermen Natur der beteiligten chemischen Reaktionen.

Anschließend wird eine umfassende numerische Analyse der laminaren, hydratisierte Ethanol-Sprühflammen durchgeführt und mit wasserfreien Gegenstücken verglichen. Diese Analyse beinhaltet eine Validierung des erweiterten mehrkomponentigen Tropfensprühflammenmodells und eine Untersuchung der Eigenschaften von hydratisierte Ethanol-Sprühflammen. Zudem untersucht die Studi mehrere Flammenstrukturen unter identischen Bedingungen für hydratisierte Ethanol-Sprays und hebt die geringe Rolle des Wassergehalts in den Tropfen bei Flammenstrukturübergängen hervor.

Abschließend wird eine detaillierte Untersuchung zu TTIP/p-Xylol-Sprühflammen durchgeführt, die die Mehrkomponentenerwärmung, Verdampfung und Bewegung der Flüssigkeit sowie die thermische Zersetzung und die daran beteiligten chemischen Reaktionen erforscht. Eine vergleichende Analyse einer reinen p-Xylol- und einer TTIP/p-Xylol-Sprayflamme zeigt, dass p-Xylol aufgrund seiner höheren Flüchtigkeit schneller verdampft und somit den notwendigen gasförmigen Brennstoff für die Aufrechterhaltung der Verbrennung liefert. Im Gegensatz dazu erfolgt die thermische Zersetzung von TTIP, die Energie für den Phasenwechsel verbraucht, in einer vergleichsweise kälteren Zone, was zu einer deutlichen Trennung der Reaktionszonen führt. Die Zersetzungsprodukte von gasförmigem TTIP, insbesondere C_3H_6 und CH_3, werden hauptsächlich in der gasseitigen Flammenzone beobachtet. Mehrere Flammenstrukturen werden während der Simulationen identifiziert. Unter diesen Strukturen zeigt die Flammenstruktur mit einer einzigen Reaktionszone auf der Sprühseite die größte Stabilität bei zunehmenden Dehnungsgeschwindigkeiten.

Publications

The following peer-reviewed journals have been published

[1] Z. Ying, H. Olguin, and E. Gutheil. Multiple structures of laminar fuel-rich spray flames in the counterflow configuration. *Combustion and Flame*, 243:111997, 2022.

[2] Z. Ying and E. Gutheil. Multiple structures and transition mechanisms of laminar fuel-rich ethanol/air counterflowing spray flames. *International Journal of Spray and Combustion Dynamics*, 15(4):197–206, 2023.

[3] Z. Ying and E. Gutheil. Numerical simulation of TTIP/*p*-xylene precursor solution spray flames in the counterflow configuration. *Applications in Energy and Combustion Science*, 15:100161, 2023.

The following peer-reviewed conference proceedings have been published

[1] Z. Ying and E. Gutheil. Numerical investigation of triple structures of laminar fuel-rich ethanol/air spray flames in the counterflow configuration. 16th International Conference on Heat Transfer, Fluid Mechanics and Thermodynamics, 2022.

[2] Z. Ying and E. Gutheil. Multiple numerical solutions of laminar fuel-rich spray flame structures in the counterflow configuration. 31st Conference on Liquid Atomization and Spray Systems, ILASS–Europe, 2022.

[3] Z. Ying and E. Gutheil. Multiple structures and transition mechanisms of laminar fuel-rich ethanol/air counterflowing spray flames. 12th Mediterranean Combustion Symposium, 2023.

[4] Z. Ying and E. Gutheil. Numerical simulation of laminar counterflowing TTIP/*p*-xylene spray flames in air. 2023 Fall Technical Meeting of the Western States Section of The Combustion Institute, 2023.

[5] Z. Ying and E. Gutheil. Numerical simulation of laminar precursor solution spray flames in the counterflow configuration. 32nd Conference on Liquid Atomization and Spray Systems, 2023.

Contents

List of Tables

List of Figures

1. Introduction

1.1 Background

Spray combustion plays a pivotal role in a wide array of energy conversion systems, including industrial burners, internal combustion engines (ICE), aerospace propulsion systems [1], and flame spray pyrolysis (FSP) [2, 3], making it a critical area of study for improving combustion efficiency and reducing environmental impacts.

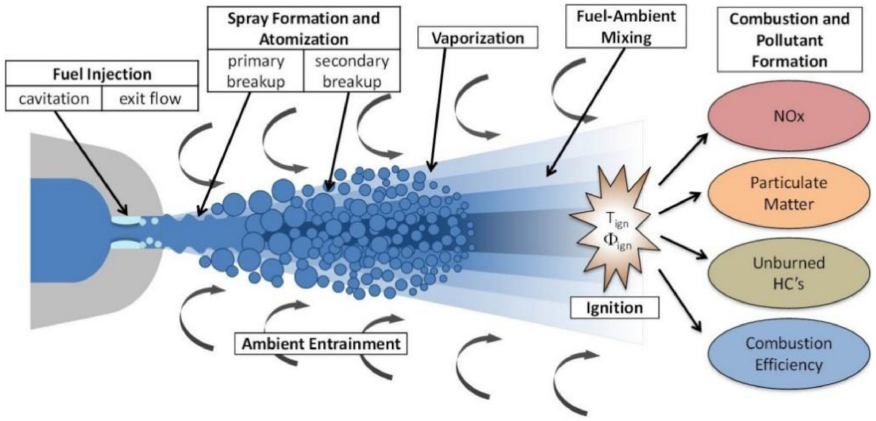

Figure 1.1: A schematic representation of the spray combustion process [4] (Open Access).

A series of critical processes are involved in spray combustion including fuel injection, atomization, evaporation, fuel-air mixing, and combustion, as depicted in Fig. 1.1. A detailed discussion of each process is presented as follows:

1. Fuel injection: The process begins with the injection of the liquid fuel into the combustion chamber. The design of the injector and the properties of the fuel largely determine the initial conditions of the atomization process and the subsequent combustion characteristics [5].

2. Atomization: This crucial step involves breaking down the bulk liquid fuel into fine droplets. The efficiency of atomization affects the surface area available for evaporation and thus significantly impacts the combustion efficiency [6]. Atomization can be further subdivided into primary and secondary stages, where primary atomization breaks the bulk liquid into ligaments and large droplets, and secondary atomization further reduces these droplets

into finer particles. Once atomized, the droplets disperse into the combustion chamber. The dispersion pattern is influenced by the chamber's aerodynamics and the droplets' physical properties [7].

3. Evaporation: Evaporation is a critical step wherein the liquid droplets transition into vapor. The rate of evaporation is a function of the droplet size, ambient temperature, and pressure, as well as the fuel's properties [8].

4. Fuel-air mixing: Effective mixing of the fuel vapor with ambient air is essential for efficient combustion. The quality of mixing dictates the stoichiometry of the reaction zones, which in turn affects the combustion efficiency and formation of pollutants [9].

5. Combustion: The final stage is the actual combustion of the vapor-air mixture, leading to heat release. The combustion can be either premixed or non-premixed depending on when the mixing of the fuel and air occurs [4].

The complexity inherent in spray combustion arises from the sophisticated interaction between fluid dynamics, heat transfer, chemical kinetics, and phase transition phenomena. A thorough comprehension of these interactions is critical for improving combustion efficiency and reducing emissions of pollutants [10]. This understanding encompasses both monocomponent and multicomponent spray combustion scenarios [8, 11].

1.2 Monocomponent Spray Combustion

Monocomponent spray combustion involves the combustion of atomized droplets composed of a single liquid fuel type. These systems, characterized by their homogeneity in chemical composition, are relatively simpler to analyze compared to their multicomponent counterparts and have traditionally served as foundational models for theoretical exploration in spray combustion dynamics [8, 11, 12]. The behavior of these sprays is significantly influenced by the fuel's thermophysical properties, including density, viscosity, thermal conductivity, and specific heat capacity, as well as by the operating conditions, such as ambient temperature and pressure [8, 11]. Among various monocomponent fuels, ethanol (C_2H_5OH), categorized as a biofuel, is acknowledged for its considerable potential to reduce greenhouse gas emissions and enhance air quality [13]. Additionally, it presents a viable alternative to fossil fuels due to its potential for sustainable production [13, 14, 15, 16].

Bioethanol is synthesized from various feedstocks, and categorized into four generations based on their source and conversion efficiency. First-generation bioethanol is generally obtained from food crops, which have lower processing expenses but high feedstock costs. Second-generation bioethanol utilizes cost-effective lignocellulosic materials, whereas third-generation bioethanol is derived from algae. Fourth-generation bioethanol employs genetically modified algae to enhance ethanol yields [17, 18]. This sustainable

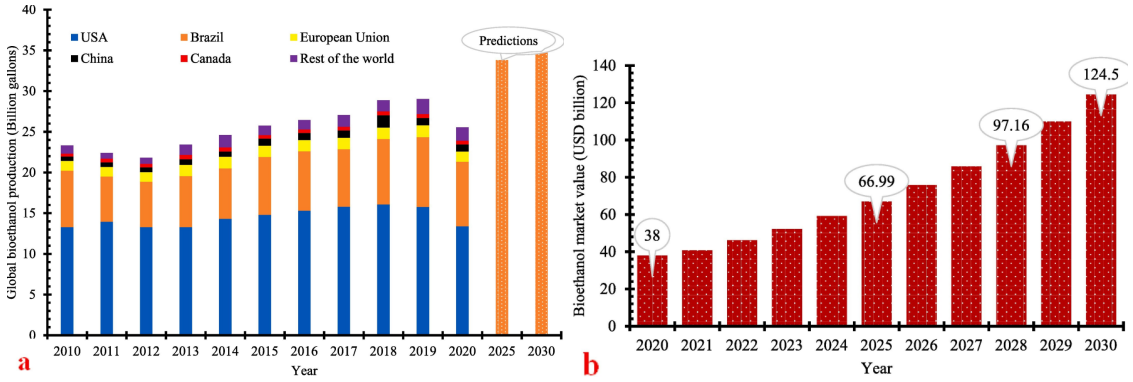

Figure 1.2: (a) Global bioethanol production in different regions and countries. (b) Bioethanol market value from 2020 to 2030 [30] (Copyright Permitted).

fuel is compatible with existing fuel infrastructure and offers the benefit of lower production costs, which has led to its increased adoption over the years [15, 17]. With the increasing economic and ecological advantages, as presented in Fig. 1.2, the production of bioethanol has experienced significant growth and is projected to continue expanding. From 2010 to 2019, global ethanol production rose from 23.31 to 29.03 billion gallons (1 gallon equals 3.785 liters), with projections indicating a rise to 33.8 by 2025 and 34.87 billion gallons by 2030 [19]. Furthermore, the market value of bioethanol, which stood at United States dollar (USD) 38 billion in 2020, is anticipated to increase to USD 66.99 billion by 2025, USD 97.16 billion by 2028, and USD 124.5 billion by 2030, reflecting a continuing rise in demand for this renewable fuel [20]. The utilization of bioethanol not only aids in mitigating greenhouse gas emissions and other pollutants but also supports economic growth and creates significant employment opportunities, particularly in rural areas [21]. Ethanol blends in gasoline significantly decrease sulfur oxide emissions, a major cause of acid rain and a known carcinogen, owing to the minimal sulfur content in ethanol [16]. However, challenges such as ethanol's corrosiveness and lower energy density necessitate significant modifications to engines [22, 23]. The behavior of ethanol spray combustion, which affects engine performance and emissions, depends on factors like droplet size distribution, spray velocity, ambient temperature, and pressure [24, 25, 26, 27, 28, 29]. Consequently, the sustained pursuit of research and the development of advanced predictive methodologies are imperative for a comprehensive assessment of the fundamental characteristics inherent in ethanol spray combustion.

The investigation of combustion phenomena in (monocomponent) spray systems widely utilizes theoretical frameworks derived from flamelet models [31, 32]. This methodology is particularly effective at characterizing the conditions in non-premixed or partially premixed environments often observed in spray combustion [31, 32]. By describing the complex interactions in turbulent flows, the flamelet approach facilitates the efficient integration of

detailed chemical kinetics, thus separating the study of chemistry from turbulence dynamics [33]. This approach is particularly beneficial in scenarios with high Damköhler numbers where combustion reaction zones are markedly thin compared to the scale of turbulent eddies [32].

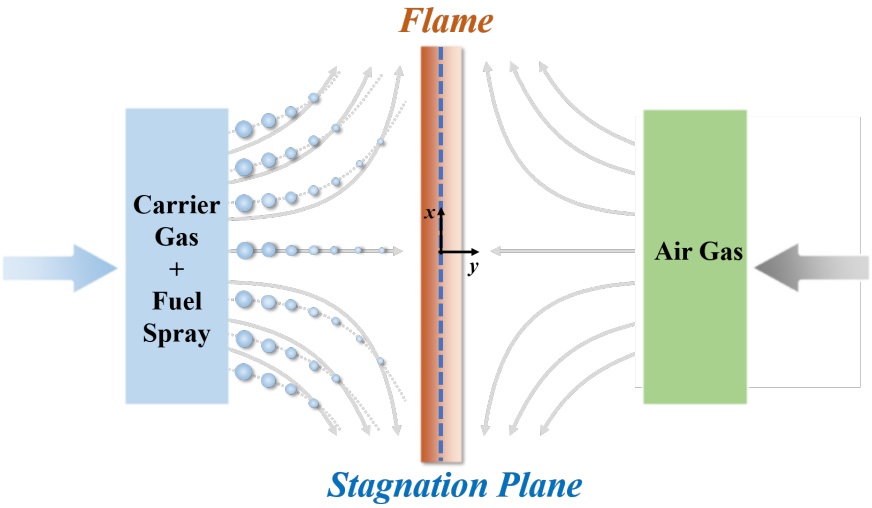

Figure 1.3: Schematic diagram of the spray flame in the counterflow configuration.

Laminar diffusion flames serve as the foundational element for flamelet models, as proposed by Peters [31], which are designed to efficiently simulate turbulent gas flames [34, 35, 36]. A significant benefit of employing laminar flame structures, particularly in a counterflow configuration, is the ability to simplify two-dimensional differential equations into a one-dimensional form through a similarity transformation [31]. This approach allows for the integration of complex chemical reaction mechanisms, enhancing the models' accuracy and predictive capabilities. The counterflow configuration is characterized by its mean velocity movement and arises from the interface dynamics typical of shear and mixing layers, as discussed in [37]. Conventional combustion chambers frequently exhibit similar local counterflow configurations, typically forming around the stagnation point near the injector exit where vortex breakdown occurs in the swirling air-feed stream, detailed in [38]. This configuration is extensively used in laboratory experiments to investigate both reacting and non-reacting spray flows, as evidenced by multiple studies [39, 40, 41, 42, 43, 44, 45]. These configurations are also prevalent in numerical simulations that examine the impact of strain on spray flames, further highlighting their significance in the field [26, 28, 29, 42, 46, 47, 48, 49, 50, 51, 52, 53, 54, 55, 56, 57, 58, 59, 60, 61, 62, 63, 64]. Therefore, this configuration is employed in this study. As illustrated in Fig. 1.3, the standard setup consists of an axissymmetric two-dimensional fuel/air spray flame. An air stream carries the fuel spray from the left side of the counterflow configuration, while a pure air stream flows from the right side.

The current state of the art, research gap, and the detailed mathematical modeling of monocomponent and multicomponent droplet sprays in a counterflow configuration are extensively discussed in Chapter 2. Compared to monocomponent spray combustion, multicomponent spray combustion more accurately represents real-world combustion systems, as practical fuels consist of multiple components with varying volatilities and chemical properties [65]. Comprehensive research in this field is essential due to its significant implications for practical applications.

1.3 Multicomponent Spray Combustion

Multicomponent spray combustion encompasses the atomization and combustion of fuel droplets consisting of multiple chemical species. This type of spray is more representative of practical combustion systems where fuels often comprise multiple components with distinct volatilities and chemical properties [65]. The complexity of multicomponent sprays surpasses that of monocomponent sprays due to the differential evaporation rates of the components during combustion [66]. In multicomponent sprays, the interaction between different fuel components can significantly affect the combustion characteristics. For example, the presence of heavier or more complex hydrocarbons can influence the ignition behavior and the formation of soot [9]. Research in multicomponent spray combustion has focused on developing computational models that can handle the added complexity of multiple evaporating components [54, 67, 68, 69, 70, 71, 72, 72]. These models require sophisticated algorithms to simulate the transport properties, chemical reactions, and phase changes of each component accurately. In this dissertation, two multicomponent systems are examined: a hydrous ethanol solution and a precursor solution composed of titanium(IV) isopropoxide (TTIP) and *p*-xylene. Hydrous ethanol is selected as it is ideally suited for the numerical validation of the proposed extended multicomponent spray combustion model employed in this work (see Subsection 2.2.4). It also facilitates direct comparison with monocomponent ethanol, also referred to as ethanol, pure ethanol, or anhydrous ethanol. The TTIP/*p*-xylene precursor solution is chosen for investigating multicomponent spray combustion within the scope of FSP.

Hydrous ethanol demonstrates significant potential for direct application in ICE, presenting notable economic and technological advantages over anhydrous ethanol [73, 74]. As previously mentioned, the production of fuel-grade anhydrous ethanol can utilize a variety of raw materials; however, the core production processes typically involve fermentation, distillation, and dehydration [17, 18]. It is important to note that the presence of azeotropic points in water-ethanol mixtures necessitates substantial energy expenditure during the dehydration phase. This step is critical for the removal of water, thereby facilitating the pro-

duction of anhydrous ethanol, which is essential for fuel applications [75, 76]. Utilizing hydrous ethanol at the azeotropic point of ethanol and water can result in an energy saving of up to 14% in the production of anhydrous ethanol, which equates to approximately 3.5 MJ/L [75, 76].

Informed by considerations of both energy efficiency and economic benefits, the direct application of hydrous ethanol in ICE has undergone extensive evaluation. Numerous experiments and simulations have been conducted to explore the operation of ICE fueled by hydrous ethanol, demonstrating the technology's applicability and enhanced system performance. Gainey et al. [77] conducted an experiment to explore the effect of injection strategy on the heat release process in thermally stratified compressions ignition, and they found a more homogeneous mixture of hydrous ethanol and air in the combustion chamber, indicating it is optimal for the single injection strategy. Stable engine operation was obtained for hydrous ethanol with hydration as high as 40 vol% (volume fraction), under stoichiometric operation [78, 79, 80]. Martins et al. [81] found 6.8% hydrous ethanol by mass emitted higher CO, HC, and NOx than compressed natural gas and commercial gasoline with 22% ethanol when they did engine steady-state experiments. The optical experiment performed by Koupaie et al. [82] showed that at the fixed spark timing of $-40°$after top dead center, the flame speeds decreased from 10.93 m/s for anhydrous ethanol to 8.2 m/s for hydrous ethanol with 20 vol% water. Besides flex-fuel vehicles, the inclusion of hydrous ethanol in the blends exhibited a favorable influence on brake-specific fuel consumption [83, 84]. Improvements in the brake thermal efficiency were also obtained for hydrous ethanol/gasoline blends [84, 85]. Dempsey et al. [86] numerically investigated the reactivity controlled compression ignition of hydrous ethanol in a heavy duty diesel engine, revealing that port-injected ethanol containing 30% mass water content achieved a peak gross cycle efficiency of 55% and minimal NOx and soot emissions. A numerical simulation analysis conducted by Boldaji et al. [87] revealed that in an engine configuration with a wide included angle of 150°, the hydrous ethanol spray targeted the piston bowl's squish region, enhancing thermal stratification for improved control of heat release rates. O'Donnell et al. [88] employed a computational fluid dynamics (CFD) model to explore the impact of hydrous ethanol direct injection at various timings during the intake stroke in a diesel engine, indicating the timing of intake stroke injection played a significant role in influencing the extent of hydrous ethanol/air mixing. While there are experimental and numerical researches on hydrous ethanol-fueled engine operation, few foundational combustion studies exist on hydrous ethanol, primarily focusing on laminar burning velocity [89, 90, 91, 92], ignition delay times [93], spray characteristics [87], and flame instability [94]. This limited scope underscores the need for additional research into hydrous ethanol combustion, particularly focusing on spray combustion [73, 74]. A comprehensive investigation is cru-

cial to enhance the understanding of the fundamental combustion characteristics of hydrous ethanol spray flames.

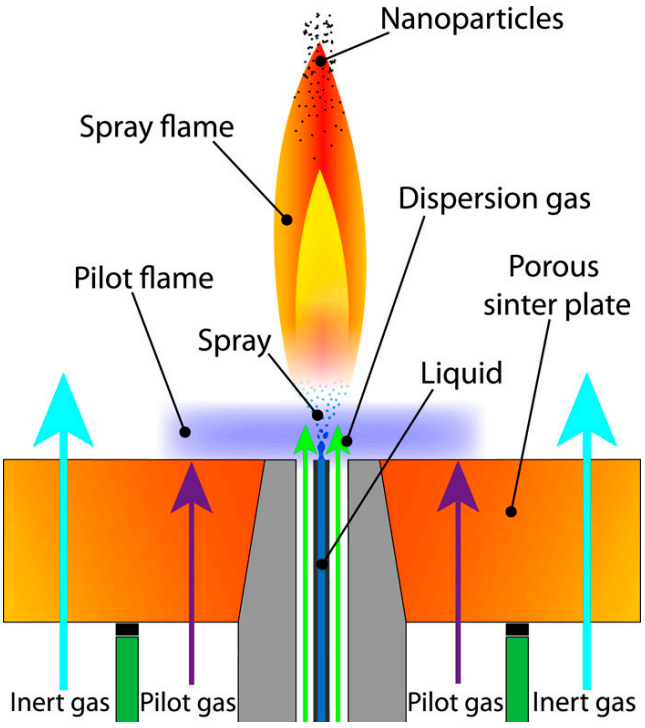

Figure 1.4: Schematic of SpraySyn burner designed by Schneider et al. [95] (Open Access).

Multicomponent precursor solutions are utilized in FSP for the synthesis of functional nanoparticles [2, 3]. The complex processes inherent in FSP, which include spray injection, the vaporization of multiphase droplets, combustion, and nanoparticle formation, as illustrated in Fig. 1.4, present substantial challenges to both experimental investigations and numerical simulations [2, 3]. TTIP is commonly utilized as a precursor in the production of TiO_2 nanoparticles via FSP [96, 97, 98, 99, 100]. This titanium(IV) alkoxide, with the chemical formula $Ti\{OCH(CH_3)_2\}_4$, is significant in both organic synthesis and materials science [101]. In nonpolar solvents, TTIP predominantly exists as a monomer [102]. Various precursor solutions of TTIP have been explored, including TTIP/ethanol [103, 104, 105, 106, 107] and TTIP/xylene [104, 105, 107, 108, 109, 110, 111, 112, 113], among others [114, 115]. Chang et al. [103] successfully synthesized TiO_2 nanoparticles by using the TTIP/ethanol precursor solution via FSP, and they found that a low precursor concentration in the solvent caused the formation of smaller nanoparticles. Bettini et al. [105] synthesized TiO_2 nanostructured powders with different structural properties by using either ethanol or xylene as a solvent for TTIP in FSP. They found the use of ethanol as the solvent made the powder with a higher photocatalytic activity. Li et al. [108] experimentally investigated the combustion behavior of single isolated droplets containing TTIP and xylene, observing their micro-explosions. Torabmostaedi and Zhang [109] conducted a numerical study on the

formation of TiO_2 nanoparticles via FSP using a mixture of TTIP, xylene, and acetonitrile. Their simulation results, validated by experimental data, demonstrated that using air instead of oxygen as the dispersion gas resulted in primary particle diameters that were equivalent or slightly smaller. Lindberg et al. [114] employed a two-step simulation method to model the synthesis of TiO_2 nanoparticles from TTIP doped in a premixed $C_2H_4/O_2/Ar$ stagnation flame, applying a detailed particle model to resolve the particle morphology, and the results of the primary and aggregate particle size distributions agreed well with their experimental data [115]. Variable liquid properties of the TTIP and *p*-xylene mixture at atmospheric pressure were measured by Keller et al. [110]. Gonchikzhapov and Kasper [104] investigated the thermal decomposition of the precursor solution spray of TTIP/*o*-xylene and TTIP/ethanol, and the stable coexistence of the precursor and the solvent was found to show no chemical interaction between them. Abdelsamie et al. [106] investigated the formation of TiO_2 particles in a configuration similar to the experiment [95], where an anhydrous ethanol spray was injected; the precursor was assumed to directly lead to the TiO_2 particles in a one-step reaction. In the recent study by Abdelsamie et al. [107], TTIP was mixed separately with *o*-xylene and ethanol to assess their effects on nanoparticle formation. Simulations revealed that ethanol promotes quicker agglomeration and results in larger nanoparticles. Narasu et al. [111] numerically investigated the heating and evaporation of a single precursor solution droplet of TTIP/*p*-xylene in hot oxidizing environments without combustion. Then they successfully developed a new model for the puffing and micro-explosion that may occur in single TTIP/*p*-xylene droplets [112]. Kunstmann et al. [113] used data from Li et al. experiments [108] to validate their one-dimensional model of heating and evaporation of pure xylene and TTIP/*p*-xylene droplets. They analyzed the superheating characteristics within these bicomponent droplets to explain the mechanism of micro-explosions.

In FSP, the dynamics of heating and evaporation in multicomponent precursor solution droplets interacting with spray flames remain underexplored, although multicomponent fuel sprays have been extensively studied in the context of liquid combustion processes [54, 67, 68, 69, 70, 71, 72, 72]. This gap emphasizes the necessity for an in-depth investigation to enhance our understanding of the fundamental combustion characteristics of precursor solutions spray flames. TTIP/*p*-xylene is chosen for this study due to the availability of detailed thermophysical properties and advanced chemical kinetics, as discussed in Subsection 2.2.5.

1.4 Research Objectives

The objective of this study is to perform numerical simulations of both monocomponent and multicomponent droplet spray flames within a counterflow configuration. Initially, this

research utilizes the established Eulerian-Lagrangian framework to investigate monocomponent ethanol spray flames, specifically under local fuel-rich conditions [46, 47]. This approach aims to identify and characterize multiple flame structures, enhancing understanding of how liquid fuel impacts flame structure beyond stoichiometric conditions [28, 29]. The second objective is to extend the monocomponent model to multicomponent scenarios by introducing the multicomponent droplet heating and evaporation model proposed by Brenn et al. [116]. This extended model is then validated with hydrous ethanol spray flames. The impact of water addition on flame characteristics is analyzed by comparing it to anhydrous ethanol. Finally, the extended multicomponent spray flame model is applied to a TTIP/*p*-xylene precursor solution to explore fundamental combustion characteristics influenced by variables such as initial gas strain rates, equivalence ratios, initial droplet radii, and precursor mass loadings in the solution.

The dissertation is organized into several chapters:

Chapter 2 presents the current state of the art, research gap, and mathematical model of monocomponent and multicomponent droplet spray flames in a counterflow configuration. This includes a detailed discussion of the governing equations that describe the gas and liquid phases, along with the spray source terms. The chapter also describes the extension of the model from monocomponent to multicomponent droplet sprays and the treatment of thermophysical properties and chemical kinetics relevant to the studied systems. Additionally, it concludes with a comprehensive description of the numerical solution methods employed.

Chapter 3 provides a comprehensive presentation of scientific findings from numerical simulations of both monocomponent and multicomponent droplet spray laminar flames in the counterflow configuration. This chapter initially focuses on detailed examinations of multiple laminar spray flame structures using monocomponent ethanol droplets under fuel-rich conditions. This study is the first to report the coexistence of three distinct spray flame structures under identical boundary and initial conditions. These variations are influenced by factors such as the gas strain rate, the equivalence ratio, and the initial droplet radius. This research examines the conditions that facilitate different flame structures and investigates the underlying physical and chemical mechanisms. Then, a numerical analysis of laminar spray flames of bicomponent hydrous ethanol in a counterflow setup is performed, expanding the monocomponent model to include multicomponent sprays. The typical flame structure within two chemical reaction zones of hydrous ethanol in the counterflow configuration is presented, accompanied by a comparative analysis of gas characteristics with monocomponent anhydrous ethanol spray flame. Fuel-rich and stoichiometric conditions are considered. The impact of water presence in ethanol droplet spray on the flame structure is discussed, considering the influence of endothermic evaporation and vapor chemical

kinetics. The extinction strain rate and its mechanism of the hydrous ethanol spray flame are analyzed. Lastly, it identifies multiple flame structures under the same conditions and analyzes the influence of component concentration within the droplets on these structures. As the last section of Chapter 3, a detailed numerical simulation of the heating, evaporation, and combustion of a laminar TTIP/p-xylene precursor solution spray in a counterflow configuration is undertaken. This simulation examines the variable physical properties of the precursor solution and integrates an advanced chemical reaction mechanism for the thermal decomposition of TTIP and the combustion of the blend. A parameter study is performed to investigate the fundamental combustion characteristics of the TTIP/p-xylene precursor solution, influenced by variables such as initial gas strain rates, equivalence ratios, initial droplet radii, and precursor mass loadings. Multiple flame structures are identified, with the flame structure featuring a single reaction zone on the spray side showing the greatest stability as strain rates increase.

Chapter 4 provides a comprehensive summary of the key findings, outlines the significant conclusions drawn from the study, and suggests potential directions for future research.

2. Mathematical Model

This chapter is dedicated to the mathematical modeling of monocomponent and multicomponent droplet spray flames in a counterflow configuration. Initially, it provides a review of the current state and research gap of numerical studies on both monocomponent and multicomponent spray flames, specifically emphasizing simulations of ethanol, hydrous ethanol, and TTIP/p-xylene spray flames. Further, the model that characterizes the monocomponent droplet spray flame in this specific configuration is detailed. This includes the presentation of both gas and liquid phase equations, linked via the coupling source term. Subsequently, the extension of this model from monocomponent to multicomponent systems is presented, incorporating multicomponent heating and evaporation equations along with the modified source term for each droplet group transitioning to the gas phase. Finally, an in-depth description of the chemical kinetics and thermophysical properties of various droplet systems is provided, followed by a detailed illustration of the numerical procedures employed in solving the governing equations.

2.1 State of the Art

Numerical research on spray flames is vital for advancing our understanding of various combustion systems, including industrial furnaces, aircraft engines, and ICE, among others [1, 10]. The concept of flamelets has been introduced to describe flame structures predominantly as one-dimensional laminar configurations, which are subsequently subjected to the influences of turbulence, being stretched and folded accordingly [32]. These laminar flame structures form the foundational basis for numerous flamelet models, which have been developed to simulate turbulent gaseous flames in a manner that is computationally efficient [34, 35, 36]. Turbulence-chemistry interactions are managed by averaging these structures using a probability density function that accounts for turbulent fluctuations [32, 34, 35, 36, 117].

Originally developed for non-premixed gas flames [31, 118, 119, 120], flamelet models have expanded to include premixed [119, 120, 121, 122, 123], partially premixed [124], and spray flames [125, 126, 127, 128, 129, 130, 131, 132, 133, 134, 135]. Continillo and

Sirignano [46] demonstrated that the similarity formulation for gas flames could also apply to dilute spray flames in a counterflow configuration, enabling their incorporation into spray flamelet simulations. This approach allows detailed chemical reactions and pollutant formation to be considered [31]. Flamelet models for spray combustion, including spray flamelet libraries, are inherently more complex than their gas flame counterparts. Unlike gas flamelets, which primarily depend on the mixture fraction and scalar dissipation rate, spray flamelets also depend on initial gas and spray velocities, equivalence ratio, and droplet size [47]. This complexity is further increased by the variability of these parameters, which has been studied across various fuels and configurations [26, 46, 47, 55, 126]. Moreover, while multiple numerical solutions for a set of characterizing parameters have been relatively understudied [56, 136, 137, 138, 139], their existence is crucial for the proper development of flamelet libraries, suggesting an area needing further research.

In their foundational study, Continillo and Sirignano [46] suggested that the governing equations for laminar spray flames in a counterflow configuration may not yield a unique numerical solution. This hypothesis was later validated by Gutheil [136], who identified two distinct solutions under identical initial and boundary conditions for stoichiometric methanol/air spray flames at low strain rates. Subsequent research by Vié et al. [56] on turbulent counterflow configurations using monodisperse n-dodecane sprays revealed the presence of multi-modal spray flame structures, challenging the integration of these findings into flamelet-based tabulation methods for turbulent combustion models due to the necessary information on boundary conditions and flamelet history. Further investigations by Xie et al. [138] demonstrated the coexistence of collocated, distributed, and cool flames in canonical counterflow n-dodecane spray at relatively low strain rates using various low-temperature chemical reaction mechanisms. This study highlighted the limitation of droplet reversal, a characteristic behavior in counterflow spray flames, where droplets evaporate before reaching the stagnation plane. Carpio et al. [137] explored dodecane spray flames with carrier nitrogen against an air stream in the counterflow setup, discovering two distinct combustion behaviors: a diffusion flame and flameless combustion. They identified a fundamental distinction between pure gas combustion and spray flames. In pure gas combustion, the controlling factor is the finite-rate chemistry, represented by the Damköhler number. However, in spray flames, the temperature-dependent vaporization rate critically limits the reactions. This limitation can result in the absence of a combustion zone due to insufficient vapor-phase fuel. Hu and Wang [139] conducted simulations of ethanol spray flames, where the sources for mass, momentum, and energy were simplified based on the fundamental principles of spray combustion physics. This simplification was numerically validated, revealing the presence of double flame structures within the spray. Despite existing studies in this field [56, 136, 137, 138, 139], the issue of multiple numerical solutions

for a single set of characterizing parameters requires further investigation. This is crucial due to its significant relevance and complexity in the development of flamelet libraries [56]. In practical applications involving spray flames, the equivalence ratio varies widely. Near the spray cone, flames are typically fuel-rich. Thus, understanding the fuel-rich condition is crucial for this study.

In the domain of multicomponent spray reacting flows, studies utilizing the spray flamelet approach are notably scarce [140, 141]. Zhang et al. [140] advanced this field by generating a spray flamelet library based on a model flame, employing enthalpy as an additional controlling variable to account for interphase heat transfer. The spray flamelet generated manifolds approach was validated against direct integration of finite rate chemistry, serving as a benchmark. Their findings highlighted the limitations of conventional single-phase generated manifolds, which use a fixed pre-vaporized composition at the fuel inlet and fail to accurately capture the preferential behavior of multicomponent fuels. Further contributions were made by Yi et al. [141], who conducted simulations on multicomponent spray reacting flows using a newly developed spray flamelet model integrated with a four-component jet fuel surrogate. This approach was implemented in the open-source CFD code OpenFOAM, integrating detailed reaction kinetics with large eddy simulations (LES) to improve computational efficiency in aero-engine combustor evaluations. The model demonstrated robust predictive capabilities, accurately reflecting experimental statistics in both gas and liquid phases, and capturing the complex dynamics of flame structures, including preferential evaporation effects and multi-regime combustion phenomena. This work underscores the potential of the spray flamelet approach to encapsulate the intricate interactions within multicomponent, two-phase combustion systems, offering novel insights into turbulent spray combustion dynamics. Compared to the research on monocomponent spray flames, studies on multicomponent spray flames are significantly less extensive within the context of spray flamelet theory. Therefore, further studies on multicomponent spray flames in counterflow configuration are necessary.

Numerical studies on hydrous ethanol are predominantly focused on its applications in engines [86, 87, 88] and fundamental combustion characteristics [89, 90, 91]. Dempsey et al. [86] investigated the reactivity controlled compression ignition (RCCI) of hydrous ethanol in a heavy-duty diesel engine, demonstrating that port-injected ethanol with 30% water by mass achieved a peak gross cycle efficiency of 55%, alongside significantly reduced NOx and soot emissions. Further research by Boldaji et al. [87] analyzed engine configurations with a wide included angle of 150°, showing that hydrous ethanol sprays targeting the piston bowl's squish region can enhance thermal stratification and control of heat release rates. Additionally, O'Donnell et al. [88] utilized a CFD model to assess the impact of various injection timings of hydrous ethanol during the intake stroke in a diesel

engine, highlighting the critical role of injection timing in optimizing ethanol/air mixing. While these studies provide valuable insights into hydrous ethanol's performance in engine systems, foundational research on its combustion, particularly in terms of laminar burning velocity and spray characteristics, remains limited. Existing studies such as those by Liang et al. [89], Treek et al. [90], and Xu et al. [91] focus on these basic parameters but do not extensively explore spray combustion dynamics. Liang et al. [89] conducted simulations of one-dimensional planar flames for ethanol-water–air mixtures, varying the equivalence ratios from 0.7 to 1.6 under conditions of 0.1 MPa and 383 K. The study aimed to investigate the impact of water addition on flame structure, laminar burning velocity sensitivity, and the net reaction rates of elementary reactions. By introducing a fictitious water model in the simulation, they distinguished the physical effects of water from its chemical effects. The results demonstrated that both unstretched flame speeds and laminar burning velocities decrease with increasing water content. Treek et al. [90] investigated the laminar burning velocities of ethanol-water-air mixtures using the heat flux method. The study involved aqueous ethanol with water content ranging from 0% to 40% by mole. Measurements were conducted at an initial gas temperature of 358 K and atmospheric pressure. Experimental data were compared with predictions from four kinetic models, which displayed consistent behavior across the range of ethanol dilution. However, significant discrepancies were noted between model predictions and experimental data from spherical flames. Further numerical analyses indicated that water addition significantly influences laminar burning velocities by interacting strongly with the H_2/O_2 and C1 oxidation/recombination pathways. Xu et al. [91] conducted an investigation into the laminar flame characteristics of hydrous ethanol through experiments performed in a constant volume combustion chamber. They measured the laminar burning velocity of ethanol with water content ranging from 0 to 20% by volume across a broad range of equivalence ratios (0.7 to 1.4) at initial conditions of 388 K and 0.1 MPa. Numerical simulations using CHEMKIN were based on Marinov's [142] and Olm's [143] ethanol oxidation mechanisms. Additionally, they examined the combustion of hydrous ethanol with 20% water by volume in oxygen-enriched air. The results demonstrated a consistent overall trend between the experimental and simulation data regarding laminar burning velocity versus equivalence ratio. They concluded that oxygen-enriched air can effectively reduce the negative impacts of water on combustion.

Despite its vital importance [73, 74], numerical studies on hydrous ethanol spray flames are notably limited [92]. Filho et al. [92] employed a recently proposed phase change model [144] to conduct numerical simulations of freely propagating flames in quiescent droplet mists with detailed chemistry descriptions. The study examined the impact of water addition in both gaseous and liquid phases under various scenarios. The results indicated that multicomponent phase change significantly affects flame speed in humid air and with

hydrous ethanol. Specifically, it was found that the flame speeds of hydrous ethanol are lower than those of pure ethanol droplets under the same atmospheric conditions. The limited exploration in this area underscores a significant research gap that needs to be addressed to better understand the fundamental combustion properties of hydrous ethanol, especially regarding its behavior in spray flames.

Numerical simulations of precursor solution droplets provide crucial insights that enable the modeling of complex processes within FSP, enhancing computational efficiency and fidelity [145]. Research on the combined effects of multicomponent droplet evaporation and spray flames in the context of FSP remains limited. Heine and Pratsinis [67] examined the spray combustion of multicomponent zirconium n-propoxide ethanol precursor solution droplets, specifically focusing on the influence of spray polydispersity and the relationship between evaporating mass flux and droplet surface composition. They utilized the zero-diffusion limit for multicomponent evaporation, an approach generally advised against under combustion conditions [8]. Building on this, Torabmostaedi et al. [146, 147] conducted a numerical study integrating CFD with particle dynamics to investigate the impact of processing parameters on the formation of zirconia nanoparticles via FSP. The simulation results were validated against experimental data. The findings indicate that increasing the pressure drop and the oxidant/mixture volume feed ratio reduces the residence time and sintering of nanoparticles in the flame. In contrast, variations in the inlet sheath gas feed had a negligible effect on fluid flow and final particle size. Torabmostaedi and Zhang [109] conducted a numerical study on the impact of processing parameters on the formation of TiO_2 nanoparticles via FSP using mixtures of TTIP, xylene, and acetonitrile. Their simulation results indicated that using oxygen as the dispersion gas increased the spray flame height from 12 to 22.5 cm as the TiO_2 production rate rose from 16 to 74 g/h. Additionally, the primary particle diameter was found to be equivalent or slightly smaller when air was used instead of oxygen as the dispersion gas. Ren et al. [148] developed a theoretical single-droplet model to describe multicomponent droplet combustion, incorporating precursor reactions and particle formation pathways. This model was validated through experiments on both pure-component and multicomponent droplet combustion [108]. Subsequently, it was applied to describe precursor decomposition and solid-phase formation within the droplet. The results indicate that smaller droplets in hotter environments produce more nanoparticles through gas-to-particle conversion. Abdelsamie et al. [149] conducted direct numerical simulations using a configuration akin to the SpraySyn burner [95], focusing on a polydisperse *o*-xylene spray without precursor, emphasizing the numerical representation of the injection nozzle. In a related study, Abdelsamie et al. [106] explored the formation of TiO_2 particles in a similar setup, where a pure ethanol spray served as a precursor in a one-step reaction leading directly to TiO_2 particle synthesis. In their recent investigation, Abdelsamie

et al. [107] investigated the influence of solvent choice on the behavior of TTIP by conducting simulations with two distinct solvents: *o*-xylene and ethanol. Their study systematically assesses the impact of each solvent on the kinetics of nanoparticle formation. Notably, they observe that ethanol significantly accelerates the agglomeration process, resulting in the formation of larger nanoparticles compared to those formed in *o*-xylene. Baik et al [150] investigated the formation of iron oxide nanoparticles from iron nitrate dissolved in a mixture of ethanol and ethyl hexanoic acid, using the SpraySyn burner configuration [95] and LES. The liquid droplets are modeled as Lagrangian particles and gas-phase combustion is simulated using the flamelet-generated manifold approach with adaptations for particle inception. Nanoparticle dynamics are examined using three models: monodisperse, bimodal, and sectional. Comparison of nanoparticle sizes with in-situ measurements indicates that the bimodal model can be an effective alternative to the computationally intensive sectional model. While whole process simulation is crucial for enhancing the efficiency and effectiveness of nanoparticle production via FSP [67, 106, 107, 109, 146, 147, 150], the detailed interactions between multicomponent heating, droplet evaporation, and spray flames are crucial yet relatively unexplored [2, 3].

Extensive research on multicomponent fuel sprays in liquid combustion has been conducted [54, 60, 68, 69, 70, 71, 72, 92, 141], although simulations typically utilize monocomponent surrogate fuels to simplify the modeling of chemical kinetics and droplet phase changes [151, 152]. Wang et al. [54] observed that finite evaporation rates affect peak temperatures and pre-flame pyrolysis processes in opposed-flow spray flames, differentiating them from pre-vaporized conditions. Further studies, such as those by Kitano et al. [68], explored the influence of various components of Jet-A and surrogate fuels on evaporation and combustion, finding that increased droplet mass loading extends droplet lifetimes. Govindaraju and Ihme [69] developed a multicomponent droplet evaporation model that accounts for the non-ideal behavior of mixtures and variations in pressure and temperature, which was further validated by Govindaraju et al. [71] in their study on the preferential evaporation effects in multiphase turbulent spray environments. Stagni et al. [70] investigated how preferential evaporation affects the interaction between evaporation and ignition when their timescales are comparable. Shastry et al. [72] noted that preferential evaporation alters spray flame structures by modifying the fuel vapor composition at the flame front. Bonanni and Ihme [60] examined the impact of preferential evaporation in laminar counterflow spray flames, though their results are limited to scenarios with small initial droplet diameters and low strain rates to avoid droplet crossing at the stagnation plane. The multicomponent spray flamelet approach proposed by Yi et al. [141] overcomes the constraints of traditional single-phase generated manifolds that rely on a constant pre-vaporized composition at the fuel inlet, which does not effectively represent the selective vaporization behavior of multicomponent

fuels. This study highlights the effectiveness of the spray flamelet model in capturing the complex interactions of multicomponent, two-phase combustion systems, providing new perspectives on the dynamics of turbulent spray combustion. Filho et al. [92] conducted numerical simulations of freely propagating flames in bicomponent quiescent droplet mists, utilizing detailed chemical descriptions. Their findings revealed that multicomponent phase changes significantly influence flame speed in humid air and with hydrous ethanol. Specifically, the flame speeds of hydrous ethanol were observed to be lower than those of pure ethanol droplets under identical atmospheric conditions. The study underscores that characterizing a hydrophilic fuel as a monocomponent substance fails to capture critical phenomena essential for understanding reacting two-phase flows.

This literature review identifies a critical research gap in the understanding of multiple flame structures of monocomponent fuels under fuel-rich conditions. Additionally, the fundamental combustion characteristics of multicomponent fuel droplet sprays, such as hydrous ethanol and TTIP/*p*-xylene precursor solutions in the context of FSP, are seldom studied. This necessitates a thorough investigation to improve both theoretical and practical knowledge for accurate numerical predictions.

The next section details the mathematical model for a monocomponent droplet spray flame in a counterflow configuration, including both gas and liquid phase equations connected through a coupling source term. It then extends this model to multicomponent systems, illustrating chemical kinetics and thermophysical properties of various droplet systems, and detailing the numerical procedures for solving the governing equations.

2.2 Governing Equations and Numerical Solution

The gas-phase equations in the Eulerian framework incorporate source terms for a dilute spray, and the Lagrangian framework details droplet heating, evaporation, and motion [46, 47]. The interrelation between gas and liquid phase equations is explored in Subsections 2.2.1 and 2.2.2, respectively, with the introduction of a coupling source term described in Subsection 2.2.3. These equations are presented in both dimensional and non-dimensional forms. The model is extended from a monocomponent to a multicomponent spray combustion system in Subsection 2.2.4, incorporating equations for multicomponent heating and evaporation, as well as a modified source term for each droplet group transitioning to the gas phase. Subsection 2.2.5 thoroughly details the variable thermophysical properties and chemical kinetics of various droplet systems. Lastly, the numerical solution algorithm employed in this study is outlined in Subsection 2.2.6.

2.2.1 Gas Phase Equations

The schematic diagram of a counterflow spray flame is shown in Fig. 1.3. In this configuration, fuel droplet spray carried by air is injected from the left, opposing an air stream from the right. The resulting gas stagnation plane is clearly visible. The gas strain rate at the spray boundary of the counterflow configuration characterizes the spray flames [27]:

$$a_{-\infty} = -\frac{1}{\alpha+1}\frac{\mathrm{d}v}{\mathrm{d}y}\bigg|_{-\infty}, \tag{2.1}$$

where α equals unity for the presently used axisymmetric counterflow configuration. The subscript $-\infty$ represents the boundary on the spray side of the configuration, while v denotes the gas flow axial velocity in the axial (y) direction.

The general dimensional conservation equations for mass, momentum, chemical species mass fractions, and energy, considering the interaction between gas and droplet spray through spray source terms, are formulated as follows [47]:

$$\frac{\partial \rho}{\partial t} + \frac{\partial\left(\rho u_i\right)}{\partial x_i} = S_{\mathrm{v}} \tag{2.2}$$

$$\rho\frac{\partial u_j}{\partial t} + \rho u_i\frac{\partial u_j}{\partial x_i} = -\frac{\partial p}{\partial x_j} - \frac{\partial \tau_{ij}}{\partial x_i} - u_j S_{\mathrm{v}} + S_{\mathrm{m,j}} \tag{2.3}$$

$$\rho\frac{\partial Y_k}{\partial t} + \rho u_i\frac{\partial Y_k}{\partial x_i} + \frac{\partial V_{k,i}}{\partial x_i} = \dot{\omega}_k + \left(\delta_{\mathrm{F}k} - Y_k\right) S_{\mathrm{v}}, \;\; k = 1, ..., N \tag{2.4}$$

$$\begin{aligned}\rho c_p\frac{\partial T}{\partial t} + \rho u_i c_p\frac{\partial T}{\partial x_i} \;&=\; -\sum_{k=1}^{N} h_k\dot{\omega}_k + \frac{\partial p}{\partial t} + u_i\frac{\partial p}{\partial x_i} + \frac{\partial}{\partial x_i}\left(\lambda\frac{\partial T}{\partial x_i}\right) \\ &-\; \frac{\partial T}{\partial x_i}\sum_{k=1}^{N} c_{p,k}V_{k,i} - \tau_{ij}\frac{\partial u_i}{\partial x_j} - S_{\mathrm{v}}\int_{T_0}^{T} c_{p,\mathrm{F}}\mathrm{d}T + S_{\mathrm{e}},\end{aligned} \tag{2.5}$$

where u_i and u_j are the gas velocity in i direction and j direction, respectively. The variable ρ is the gas density, Y_k denotes the mass fraction of species k, and T presents the gas temperature. c_p and $c_{p,k}$ are the specific heat capacities at constant pressure for the mixture and the species k, respectively. p represents the static pressure, h_k denotes the enthalpy of species k, λ signifies the heat conductivity, and τ_{ij} represents the viscous stress tensor. S_{v}, S_{m}, and S_{e} are the mass, momentum, and energy source terms accounting for the interaction between the gas and liquid phases. $V_{k,i}$ is the diffusion velocity of species k in i direction within the mixture. δ denotes the Kronecker symbol, the subscript F represents the fuel, and $\dot{\omega}_k$ describes the specific chemical reaction rate for the species k, $k = 1, ..., N$. N is the total number of chemical species in the system.

The viscous tensor τ_{ij} in Eqs. 2.3 and 2.5 is defined by neglecting the bulk viscosity and given by the Newton law as:

$$\tau_{ij} = -\mu \left(\frac{\partial u_i}{\partial x_j} + \frac{\partial u_j}{\partial x_i} \right) + \frac{2}{3}\mu \left(\frac{\partial u_k}{\partial x_k} \right) \delta_{ij}. \tag{2.6}$$

The mixture's viscosity (μ), thermal conductivity (λ), and constant pressure specific heat capacity (c_p) are determined as follows:

$$\mu = \frac{1}{2} \left[\sum_{k=1}^{N} X_k \mu_k + \left(\sum_{k=1}^{N} \frac{X_k}{\mu_k} \right)^{-1} \right] \tag{2.7}$$

$$\lambda = \frac{1}{2} \left[\sum_{k=1}^{N} X_k \lambda_k + \left(\sum_{k=1}^{N} \frac{X_k}{\lambda_k} \right)^{-1} \right] \tag{2.8}$$

$$c_p = \sum_{k=1}^{N} c_{p,k} Y_k, \tag{2.9}$$

where X_k denotes the mole fraction of species k. The viscosity, μ_k and heat conductivity, λ_k for each species k are calculated using temperature-dependent polynomial expressions [153]:

$$\ln(\mu_k) = \sum_{n=1}^{4} a_{\mu,k,n} (\ln(T))^{n-1} \tag{2.10}$$

$$\ln(\lambda_k) = \sum_{n=1}^{4} a_{\lambda,k,n} (\ln(T))^{n-1}, \tag{2.11}$$

where the coefficients $a_{\mu,k,n}$ and $a_{\lambda,k,n}$ for viscosity and thermal conductivity are provided in tabulated form, as referenced by Kee et al. [153].

The heat capacity at constant pressure for species k, $C_{p,k}$ and the enthalpy of species k, h_k are calculated using the NASA polynomial tabulations [154]. These polynomials are well-regarded for their accuracy and reliability in predicting temperature-dependent properties. Typically, the NASA polynomials take the following form [154]:

$$C_{p,k} = \mathrm{R} \sum_{n=1}^{5} a_{C_p,k,n} T^{n-1} \tag{2.12}$$

$$\frac{h_k}{\mathrm{R}T} = \sum_{n=1}^{5} a_{h_k,n} T^{n-1} + \frac{a_{h_k,6}}{T}, \tag{2.13}$$

where the coefficients $a_{C_p,k,n}$ and $a_{h_k,n}$ are derived from the detailed chemical reaction mechanism files for the droplet systems. These coefficients vary depending on the temper-

ature ranges of 300 to 1000 K and 1000 to 4000 K. R represents the universal gas constant. The specific heat capacity, $c_{p,k}$ in Eq. 2.9 is then calculated by dividing the heat capacity, $C_{p,k}$ by the mass of species k.

The diffusion velocity $V_{k,i}$ of species k in direction i in Eq. 2.5 is approximated using the Hirschfelder-Curtiss diffusion law [155]:

$$V_{k,i} = -\rho D_k \frac{Y_k}{X_k}\frac{\partial X_k}{\partial x_i} - \frac{D_\mathrm{T}}{T}\frac{\partial T}{\partial x_i}, \tag{2.14}$$

where D_T represents the thermal diffusion coefficient, applicable to light species such as H and H_2. The diffusion coefficient D_k for a species k within a mixture is defined as follows:

$$D_k = \frac{1 - Y_k}{\sum_{j\neq k}^{N} \frac{X_k}{D_{kj}}}, \tag{2.15}$$

where D_{kj} is the binary diffusion coefficient between species k and j. Using detailed chemical reaction mechanisms for droplet systems, the value of D_{kj} can be derived from the polynomial provided by Kee et al. [153] as:

$$\ln(D_{kj}) = \sum_{n=1}^{4} a_{D,k,n}(\ln(T))^{n-1}. \tag{2.16}$$

Eq. 2.14 can be rewritten by using the product law as:

$$V_{k,i} = -\frac{\partial}{\partial x_i}\left(\rho D_k \frac{\partial Y_k}{\partial x_i}\right) - \frac{\partial}{\partial x_i}\left(\rho \frac{D_k Y_k}{\bar{M}}\frac{\partial \bar{M}}{\partial x_i}\right) - \frac{D_\mathrm{T}}{T}\frac{\partial T}{\partial x_i}, \tag{2.17}$$

where $\bar{M}$ represents the mean molar mass of the mixture. If the contributions of the last two terms on the right-hand side are neglected, Eq. 2.17 can be simplified to Fick's diffusion law [156]:

$$V_{k,i} = -\frac{\partial}{\partial x_i}\left(\rho D_k \frac{\partial Y_k}{\partial x_i}\right). \tag{2.18}$$

For a detailed chemical reaction mechanism, consider N species and M reactions. The summarized form of every chemical reaction is as follows:

$$\sum_{k=1}^{N} \nu'_{k,j} A_k = \sum_{k=1}^{N} \nu''_{k,j} A_k, \tag{2.19}$$

where $j = 1, \ldots, M$. A_k represents species k, while $\nu'_{k,j}$ and $\nu''_{k,j}$ denote the molar stoichiometric coefficients of species k in reaction j.

The specific chemical reaction rate of species k, denoted as $\dot{\omega}_k$ in Eq. 2.4, is determined

as follows:

$$\dot{\omega}_k = \sum_{j=1}^{M} \dot{\omega}_{k,j}, \tag{2.20}$$

where $\dot{\omega}_{k,j}$ represents the contribution of reaction j to the overall reaction rate of species k. This contribution can be obtained by:

$$\dot{\omega}_{k,j} = M_k \nu_{k,j} K_j \prod_{n=1}^{N} C_k^{\nu'_{k,j}}, \tag{2.21}$$

where M_k and C_k represent the molecular weight and concentration of species k, respectively. $\nu_{k,j} = \nu''_{k,j} - \nu'_{k,j}$. The rate of reaction j, denoted as K_j, is calculated by:

$$K_j = A_j T^{\beta_j} \exp\left(-\frac{E_j}{RT}\right), \tag{2.22}$$

where A_j, β_j, and E_j are the pre-exponential factor, a constant, and the activation energy, respectively. In this study, different detailed chemical reaction mechanisms were utilized to analyze various droplet spray flames, which are given in detail in Subsection 2.2.5.

The steady two-dimensional conservation equations for mass, momentum, energy, and chemical species mass fractions in the gas phase are simplified using the boundary layer assumption and a low Mach number [27]. These equations are then transformed into one-dimensional form through the introduction of a similarity variable, η and a stream function, f [46, 47]:

$$\eta = \int_0^y \rho \, \mathrm{d}y \quad \text{and} \quad f = \int_0^\eta \frac{u}{x} \, \mathrm{d}\eta, \tag{2.23}$$

where x denotes the radial direction. The transformed equations yield [46, 47]:

$$v = -1/\rho \left([\alpha + 1]f + f_\mathrm{v}\right) \quad \text{with} \quad f_\mathrm{v} = -\int_0^\eta 1/\rho \; S_\mathrm{v} \, \mathrm{d}\eta \tag{2.24}$$

$$\frac{\mathrm{d}}{\mathrm{d}\eta}\left(\rho\mu\frac{\mathrm{d}f''}{\mathrm{d}\eta}\right) + \left([\alpha+1]f + f_\mathrm{v}\right) f'' = (f')^2 - \frac{1}{\rho} - \frac{S_\mathrm{m}}{\rho x} \tag{2.25}$$

$$\begin{aligned} &\frac{\mathrm{d}}{\mathrm{d}\eta}\left(\lambda\rho\frac{\mathrm{d}\theta}{\mathrm{d}\eta}\right) + c_p([\alpha+1]f + f_\mathrm{v})\frac{\mathrm{d}\theta}{\mathrm{d}\eta} = \\ &\rho\sum_{k=1}^{N} V_{k,y} c_{p,k} \frac{\mathrm{d}\theta}{\mathrm{d}\eta} + \frac{1}{\rho}\sum_{k=1}^{N} h_k \dot{w}_k - \frac{1}{\rho} S_\mathrm{e} \end{aligned} \tag{2.26}$$

$$-\frac{\mathrm{d}}{\mathrm{d}\eta}(\rho V_{k,y}) + ([\alpha+1]f + f_\mathrm{v})\frac{\mathrm{d}Y_k}{\mathrm{d}\eta} = -\frac{1}{\rho}\dot{w}_k - (\delta_{\mathrm{F}k} - Y_k)\frac{1}{\rho} S_\mathrm{v}, \tag{2.27}$$

where $\delta_{\mathrm{F}k}$ equals unity if and only if the conservation equation for fuel is considered. Fur-

thermore, the ideal gas law $\rho = \bar{W}/\theta$ is used where $\bar{W} = (\sum_k Y_k/W_k)^{-1}$ is the mean molecular weight of the mixture. θ is the non-dimensional gas temperature.

The transformed governing equations (Eqs. 2.23- 2.27) are subject to the following boundary conditions [27]:

$$\begin{aligned} \eta = -\infty: \quad & f = f_{-\infty}; \quad f' = 1; \quad Y_k = Y_{k-\infty}; \quad \theta = 1; \\ \eta = \infty: \quad & f = f_{+\infty}; f' = \sqrt{\rho_{-\infty}/\rho_{\infty}}; \quad Y_k = Y_{k\infty}; \quad \theta = 1, \end{aligned} \tag{2.28}$$

where ∞ denotes the gas boundary of the counterflow configuration. In the study, the species mass fractions Y_k in both streams are set to values representative of pure air. Furthermore, for all cases studied, the injection temperatures on both sides of the configuration are non-dimensionalized by a ratio relative to 300 K, resulting in a value of unity.

The next subsection presents the dimensional and non-dimensional governing equations for the liquid phase.

2.2.2 Liquid Phase Equations

The spray is assumed to be dilute, composed of spherically symmetric droplets, and analyzed using a Lagrangian approach to describe droplet evaporation, heating, and motion. Although the study focuses on the injection of mono-disperse sprays, droplet reversal, and oscillation may result in local poly-dispersity [26, 47, 136].

The droplet motion, evaporation, heating, and number density in the dimensional form are represented by [46, 47]:

$$m_k \frac{\mathrm{d}\mathbf{v}_k}{\mathrm{d}t} = \frac{1}{2}\pi {R_k}^2 \rho_\mathrm{l} C_{D,k} (\mathbf{u} - \mathbf{v}_k)|\mathbf{u} - \mathbf{v}_k| + m_k \mathbf{g} \tag{2.29}$$

$$\dot{m}_k = 2\pi R_k \, \rho_{\mathrm{f},k} \, D_{\mathrm{f},k} \, \widetilde{\mathrm{Sh}_k} \ln(1 + B_{\mathrm{M},k}) \tag{2.30}$$

$$\frac{\partial T_{\mathrm{l},k}}{\partial t} = \frac{1}{r^2}\frac{\partial}{\partial r}\left(\alpha_\mathrm{l} \frac{r^2 \partial T_{\mathrm{l},k}}{\partial r}\right) \tag{2.31}$$

$$\frac{\partial n_k}{\partial t} + \frac{\partial \left(n_k \, v_{i,k}\right)}{\partial x_i} = S_{n,k}, \tag{2.32}$$

where the subscript k = 1, 2, ..., is the total number of different droplet size groups. t means time. ρ_l denotes liquid density, $C_{D,k}$ is the drag coefficient, $\mathbf{u}$ and $\mathbf{v}_k$ are the gas and droplet velocities, respectively, and $\mathbf{g}$ presents gravity acceleration. m_k is the mass of a droplet with radius R_k, while $\dot{m}_k$ presents the droplet mass vaporization rate of a droplet in size group k. The subscript f refers to properties in the film around the droplets and film properties are computed using the $1/3$ rule [157]. The modified Sherwood number $\widetilde{\mathrm{Sh}_k}$ accounts for convective droplet evaporation [157]. $T_{\mathrm{l},k}$ is the temperature of the liquid, r is the radial

coordinate inside the spherical droplet, and n_k is the droplet number density of droplet size group k. $S_{n,k}$ denotes the source term accounting for changes in the droplet number density due to droplet reversal or oscillation [47].

The Spalding mass transfer number, $B_{\mathrm{M},k}$ in Eq. 2.30 for each droplet size group k is defined as:

$$B_{\mathrm{M},k} = \frac{(Y_{\mathrm{F,s},k} - Y_{\mathrm{F}})}{(1 - Y_{\mathrm{F,s},k})}, \tag{2.33}$$

where Y_{F} represents the mass fraction of fuel vapor in the bulk of gas surrounding the droplet, and $Y_{\mathrm{F,s},k}$ indicates the fuel mass fraction at the droplet surface, defined as:

$$Y_{\mathrm{F,s},k} = \frac{M_{\mathrm{F}} X_{\mathrm{F,s},k}}{M_{\mathrm{F}} X_{\mathrm{F,s},k} + (1 - X_{\mathrm{F,s},k})\bar{M}_{\mathrm{s}}}, \tag{2.34}$$

where $\bar{M}_{\mathrm{s}}$ represents the mean molecular weight of the gas surrounding the droplet surface, and the fuel mole fraction at the droplet surface $X_{\mathrm{F,s},k}$ is defined as:

$$X_{\mathrm{F,s},k} = \frac{p_{\mathrm{vap}}}{p_{\mathrm{atm}}}, \tag{2.35}$$

where p_{vap} is the vapor pressure at the droplet surface, which is determined using various equations specific to the droplet spray system. p_{atm} is the atmospheric pressure. These equations are detailed in Subsection 2.2.5.

The liquid phase equations are then transformed to non-dimensional equations after introducing three specific variables [46, 47]:

$$\xi = r/R(t); \quad \xi_{\mathrm{s}} = R(t)/R_0; \quad \tau = \frac{1}{t_{\mathrm{l}}^{\star}} \int_0^t \frac{\mathrm{d}z}{\xi_{\mathrm{s}}}, \tag{2.36}$$

where z is a fictive variable and $\star$ denotes reference values. $R(t)$ and R_0 are the temporal droplet radius and its initial value, respectively.

The transformed equations for droplet heating, evaporation, and motion for each droplet size group are presented without indices to enhance the clarity and transparency of the equations, which yield [46, 47]:

$$\frac{\mathrm{d}\xi_{\mathrm{s}}}{\mathrm{d}\tau} = -\frac{1}{9}\, c_1 \rho_{\mathrm{f}} D_{\mathrm{f}} \widetilde{\mathrm{Sh}} (1 + B_Y) \tag{2.37}$$

$$\frac{\partial \theta_{\mathrm{l}}}{\partial \tau} - \frac{\xi}{\xi_{\mathrm{s}}} \frac{\mathrm{d}\xi_{\mathrm{s}}}{\mathrm{d}\tau} \frac{\partial \theta_{\mathrm{l}}}{\partial \xi} = \frac{1}{\xi_{\mathrm{s}} \xi^2} \frac{\partial}{\partial \xi} \left(\xi^2 \frac{\partial \theta_{\mathrm{l}}}{\partial \xi} \right) \tag{2.38}$$

$$\frac{\partial^2 x_{\mathrm{l}}}{\partial \tau^2} - \frac{1}{\xi_{\mathrm{s}}} \left(\frac{\mathrm{d}\xi_{\mathrm{s}}}{\mathrm{d}\tau} - c_1 \mu \right) \frac{\mathrm{d}x_{\mathrm{l}}}{\mathrm{d}\tau} = c_1 c_2 \mu \frac{\mathrm{d}f}{\mathrm{d}\eta} x_{\mathrm{l}} + c_2^2 \xi_{\mathrm{s}}^2 g_x \tag{2.39}$$

$$\frac{\partial^2 \eta_\mathrm{l}}{\partial \tau^2} + \rho \frac{\mathrm{d}\rho^{-1}}{\mathrm{d}\tau}\frac{\mathrm{d}\eta_\mathrm{l}}{\mathrm{d}\tau} - \frac{1}{\xi_\mathrm{s}}\left(\frac{\mathrm{d}\xi_\mathrm{s}}{\mathrm{d}\tau} - c_1\mu\right)\frac{\mathrm{d}\eta_\mathrm{l}}{\mathrm{d}\tau} = c_1 c_2 \mu(-([\alpha+1]f + f_\mathrm{v})) + \rho c_2^2 \xi_\mathrm{s}^2 g_\eta, \tag{2.40}$$

with $c_1 = 6\pi(M^\star/M_\mathrm{l}^\star)(L_\mathrm{l}^\star/L^\star)(t_\mathrm{l}^\star/t^\star)$ and $c_2 = t_\mathrm{l}^\star/t^\star$.

The initial and boundary conditions are:

$$\begin{aligned} &\xi_\mathrm{s}(0) = 1; \quad \frac{\partial \theta_\mathrm{l}}{\partial \xi}\,|_{\xi=0} = 0; \quad \frac{\partial \theta_\mathrm{l}}{\partial \xi}\,|_{\xi=1} = \frac{\dot{q}}{3\xi_\mathrm{s}}; \quad \theta_\mathrm{l}(\xi,0) = 1; \\ &s_\mathrm{l}(0) = s_{\mathrm{l},0}; \quad s_\mathrm{l}'(0) = s_{\mathrm{l},0}'; \quad \eta_\mathrm{l}(0) = \eta_{\mathrm{l},0}; \quad \eta_\mathrm{l}'(0) = \eta_{\mathrm{l},0}', \end{aligned} \tag{2.41}$$

where $\dot{q}$ is calculated as:

$$\dot{q} = \dot{m}\left[\frac{C_{p,\mathrm{f}}}{C_{p,\mathrm{l}}}\left(\frac{T^\star}{T_\mathrm{l}^\star}\theta - \theta_\mathrm{ls}\right)/B_\mathrm{T} - L_\mathrm{V}\right], \tag{2.42}$$

where $\dot{m}$ and L_V denote the mass evaporation rate of a droplet and the latent heat of evaporation, respectively.

The Spalding heat transfer number B_T in Eq. 2.42 can be calculated as [157]:

$$B_\mathrm{T} = (1 + B_\mathrm{M})^\phi - 1, \tag{2.43}$$

with

$$\phi = \frac{C_{p,\mathrm{l}}\widetilde{\mathrm{Sh}}}{C_{p,\mathrm{f}}\widetilde{\mathrm{NuLe}}}, \tag{2.44}$$

where Le is Lewis number which is defined as the ratio of thermal diffusivity to mass diffusivity.

$\widetilde{\mathrm{Nu}}$ and $\widetilde{\mathrm{Sh}}$ in Eq. 2.44 are modified Nusselt number and Sherwood number, respectively, and can be determined by [157]:

$$\begin{Bmatrix} \widetilde{\mathrm{Sh}} \\ \widetilde{\mathrm{Nu}} \end{Bmatrix} = 2 + [(1 + \mathrm{Re}\begin{Bmatrix} \mathrm{Sc} \\ \mathrm{Pr} \end{Bmatrix})^{1/3}[\max(1, \mathrm{Re})]^{0.077} - 1] \cdot \begin{Bmatrix} F(B_\mathrm{M}) \\ F(B_\mathrm{T}) \end{Bmatrix}, \tag{2.45}$$

where Re, Sc, and Pr are the Reynolds, Schmidt, and Prandtl numbers, respectively.

The expressions for $F(B_\mathrm{M})$ and $F(B_\mathrm{T})$ in Eq. 2.45 account for corrections of the diffusion and thermal boundary layer thickness in the convective two-film model, respectively [157]. They are defined as:

$$F(B) = \frac{(1+B)^{0.7}\ln(1+B)}{B}, \tag{2.46}$$

with $B = \{B_\mathrm{M}$ or $B_\mathrm{T}\}$.

2.2.3 Spray Source Terms

Droplet transfer between size groups at the same position results in local polydispersity within the spray, as detailed in [46]. This transfer is strategically managed to prevent new data from overwriting previously calculated information. Consequently, the spray source terms for mass, momentum, and energy at each grid point, as specified in Eqs. 2.2-2.5, are obtained as [47]:

$$S_{\mathrm{v}} = \sum_{k=1}^{K} n_k \dot{m}_k \tag{2.47}$$

$$\mathbf{S}_{\mathrm{m}} = \sum_{k=1}^{K} \left[- n_k m_k \frac{\mathrm{d}\mathbf{v}_k}{\mathrm{d}t} + n_k \dot{m}_k \mathbf{v}_k \right] \tag{2.48}$$

$$S_{\mathrm{e}} = \sum_{k=1}^{K} \left[- n_k [\dot{q}_k + \dot{m}_k L_{\mathrm{V}}(T_{\mathrm{l},k})] + n_k \dot{m}_k \int_{T_0}^{T_{s,k}} C_{p,\mathrm{F}} dT \right]. \tag{2.49}$$

In Eq. 2.49, $\dot{q}_k$ represents the energy transferred to the droplet and is defined as:

$$\dot{q}_k = \dot{m}_k \left[\frac{C_{p,\mathrm{F}}(T - T_{\mathrm{s},k})}{B_{\mathrm{T},k}} - L_{\mathrm{V}}(T_{\mathrm{l},k}) \right], \tag{2.50}$$

where $B_{\mathrm{T},k}$ represents the Spalding heat transfer number, and $L_{\mathrm{V}}(T_{\mathrm{l},k})$ denotes the temperature-dependent latent heat of vaporization for droplet size group k, which varies across the different droplet systems.

Then the source terms are non-dimensionalized with specific reference values introduced in Eq. 2.36:

$$\frac{S_{\mathrm{v}}}{\rho} = -\,3\,\frac{M_{\mathrm{l}}^{\star}}{M^{\star}}\,\frac{t^{\star}}{t_{\mathrm{l}}^{\star}}\,\frac{n}{\rho}\xi_{\mathrm{s}}\,\frac{\mathrm{d}\xi_{\mathrm{s}}}{\mathrm{d}\tau} \tag{2.51}$$

$$-\frac{S_{\mathrm{m}}}{\rho x} = \frac{M_{\mathrm{l}}^{\star}}{M^{\star}} \left(\frac{t^{\star}}{t_{\mathrm{l}}^{\star}}\right)^{2} \frac{n}{\rho s} \left[\xi_{\mathrm{s}} \frac{\mathrm{d}^2 s}{\mathrm{d}\tau^2} + 2\frac{\mathrm{d}\xi_{\mathrm{s}}}{\mathrm{d}\tau}\frac{\mathrm{d}s}{\mathrm{d}\tau} - 3\frac{t_{\mathrm{l}}^{\star}}{t^{\star}} f' s \xi_{\mathrm{s}} \frac{\mathrm{d}\xi_{\mathrm{s}}}{\mathrm{d}\tau} \right] \tag{2.52}$$

$$-\frac{S_{\mathrm{e}}}{\rho} = \frac{c_{p,\mathrm{f}}}{\bar{c_p}}\,\frac{M_{\mathrm{l}}^{\star}}{M^{\star}}\,\frac{t^{\star}}{t_{\mathrm{l}}^{\star}}\,\frac{n}{\rho}\,\dot{m}\left(\theta - \frac{T_{\mathrm{l}}^{\star}}{T^{\star}}\theta_{\mathrm{l,s}}\right)\frac{1 + B_{\mathrm{T}}}{B_{\mathrm{T}}}\,. \tag{2.53}$$

The conservation of the droplet number [46, 47] is:

$$n = \frac{n_0\ s_0\ \eta'_{\mathrm{l},0}\ \rho}{s\ \eta'_{\mathrm{l}}\ \rho_0}, \tag{2.54}$$

with

$$s = \frac{x_{\mathrm{l}}}{u_{\mathrm{l},0}}, \tag{2.55}$$

assuming that the droplet number is conserved since neither droplet coalescence nor breakup is considered. However, the spray may become polydisperse in regions where droplet re-

versal or oscillation occurs [47, 136].

The equivalence ratio $E_{-\infty}$ of the initially monodisperse spray with the initial radius R_0 refers to the injected liquid mass at the spray side of the configuration. It is defined as follows [158]:

$$E_{-\infty} = \left(\frac{v_{O_2}}{v_F}\right)_{st} \left(\frac{M_{O_2}}{M_F}\right) \frac{m_{sp,\,F}}{\rho_{-\infty} Y_{O_2,-\infty}}, \tag{2.56}$$

where v and $m_{sp,\,F}$ are the stoichiometric coefficient and the initial volumetric mass of the fuel spray, respectively.

2.2.4 Extension to Multicomponent Droplet Sprays

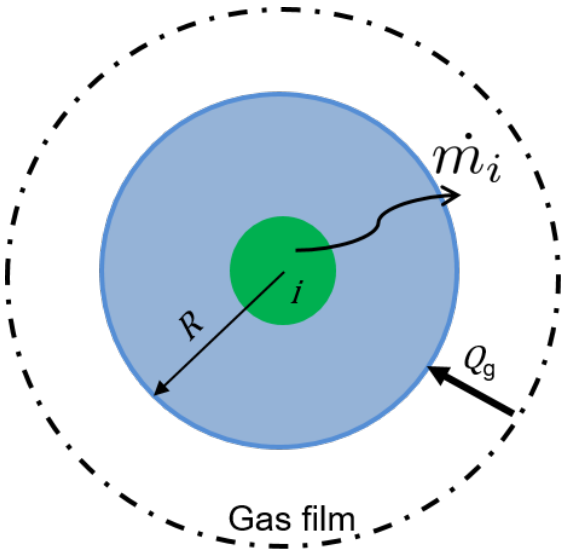

Figure 2.1: Schematic diagram of the heating and evaporation of a bicomponent droplet.

In 1989, Abramzon and Sirignano [157] developed a model for the evaporation and heating of monocomponent droplets in a convective environment, widely used in spray combustion modeling [10]. This model was extended by Brenn et al. [116] to accommodate multicomponent droplets for enhanced analysis of droplet behavior under varied conditions. Introduced in the study for multicomponent spray combustion modeling, the focus is on bicomponent droplets as illustrated in Fig. 2.1. The methodologies discussed are applicable to droplet spray systems with multiple components. This adaptability enhances the applicability of the research to more complex multicomponent sprays, which are common in various industrial processes.

Modified from Eq. 2.30, the mass evaporation rate of component i, $\dot{m}_i$ in a multicomponent droplet system is [116]:

$$\dot{m}_i = 2\pi R_i \rho_{f,i} D_{f,i} \widetilde{Sh}_i \ln(1 + B_{M,i}). \tag{2.57}$$

The total mass evaporation rate, $\dot{m}$ can be calculated as: $\dot{m} = \sum_{i=1}^{2} \dot{m}_i$. In Eq. 2.57, R_i is the volume equivalent partial radius of component i of the droplet and $\rho_{\mathrm{l},i}$ denotes the liquid density of component i. $D_{\mathrm{f},i}$ is the diffusion coefficient of component i into the ambient gas mixture. The Spalding mass transfer number $B_{\mathrm{M},i}$ of the component i in Eq. 2.57 is:

$$B_{\mathrm{M},i} = \frac{Y_{i,\mathrm{s}} - Y_{i,\infty}}{1 - Y_{i,\mathrm{s}}}, \tag{2.58}$$

where the subscript s and ∞ stand for the droplet surface and the ambience, respectively.

The source term of mass of every droplet group transferred to the gas phase due to evaporation is modified from Eq. 2.47 by:

$$S_{\mathrm{v}} = \sum_{i=1}^{2} n_i \dot{m}_i, \tag{2.59}$$

where n_i is the droplet number density of component i.

The heating model for multicomponent droplets retains the same form as that used for monocomponent droplets, as detailed in Eq. 2.31. For ease of reference, it is repeated here:

$$\frac{\partial T}{\partial t} = \frac{1}{r^2}\frac{\partial}{\partial r}\left(\alpha_{\mathrm{l}} \frac{r^2 \partial T}{\partial r}\right), \tag{2.60}$$

with the boundary conditions:

$$T_{\mathrm{l}}(r,0) = T_{\mathrm{l},0}, \left.\frac{\partial T_{\mathrm{l}}}{\partial r}\right|_{r=0} = 0, \left.\frac{\partial T_{\mathrm{l}}}{\partial r}\right|_{r=R(t)} = \frac{\dot{Q}_{\mathrm{l}}}{4\pi R^2 \rho_{\mathrm{l}} c_{p,\mathrm{l}}}, \tag{2.61}$$

where α_{l}, ρ_{l} and $c_{p,\mathrm{l}}$ are the mass average values [153] of thermal diffusivity, density and specific heat capacity of the droplet, respectively, which varies as the composition of component i inside the mixture droplet changes with time when the droplet moves along the physical space. The rate of heat transfer into the multicomponent liquid droplet, $\dot{Q}_{\mathrm{l}}$ is modeled by:

$$\dot{Q}_{\mathrm{l}} = \sum_{i=1}^{2} \dot{Q}_{\mathrm{l},i} \equiv \sum_{i=1}^{2} \dot{m}_i \left[\frac{C_{p,\mathrm{l},i}(T_\infty - T_{\mathrm{s}})}{B_{\mathrm{T},i}} - L_{\mathrm{V}}(T_{\mathrm{l},i})\right], \tag{2.62}$$

where $L_{\mathrm{V}}(T_{\mathrm{l},i}), i = 1, 2$ is the latent heat of vaporization of component i. The Spalding heat transfer number $B_{\mathrm{T},i}$ is:

$$B_{\mathrm{T},i} = (1 + B_{\mathrm{M},i})^{\phi_i} - 1, \tag{2.63}$$

with

$$\phi_i = \frac{C_{p,\mathrm{l}}\widetilde{\mathrm{Sh}}_i}{C_{p,\mathrm{f}}\widetilde{\mathrm{Nu}}_i \mathrm{Le}_i}, \tag{2.64}$$

where $\widetilde{\mathrm{Nu}}_i$ and $\widetilde{\mathrm{Sh}}_i$ are modified Nusselt number and Sherwood number of the component i, respectively, and can be calculated as:

$$\begin{Bmatrix} \widetilde{\mathrm{Sh}}_i \\ \widetilde{\mathrm{Nu}}_i \end{Bmatrix} = 2 + [(1 + \mathrm{Re} \begin{Bmatrix} \mathrm{Sc}_i \\ \mathrm{Pr}_i \end{Bmatrix})^{1/3} [\max(1, \mathrm{Re})]^{0.077} - 1] \cdot \begin{Bmatrix} F(B_{\mathrm{M},i}) \\ F(B_{\mathrm{T},i}) \end{Bmatrix}, \tag{2.65}$$

where Sc_i, and Pr_i represent the Schmidt and Prandtl numbers of the component i, respectively.

The expressions for $F(B_{\mathrm{M},i})$ and $F(B_{\mathrm{T},i})$ in Eq. 2.65 account for corrections of the diffusion and thermal boundary layer thickness in the convective two-film model, respectively [157]. They can be calculated as:

$$F(B) = \frac{(1 + B)^{0.7} \ln(1 + B)}{B}, \tag{2.66}$$

for $B = \{B_{\mathrm{M},i} \text{ or } B_{\mathrm{T},i}\}$.

The ideal Raoult's law is utilized to address vapor-liquid equilibrium:

$$X_{\mathrm{s},i} = X_i \frac{p_{\mathrm{vap},i}}{p_{\mathrm{atm}}}, \tag{2.67}$$

where $X_{\mathrm{s},i}$ represents the mole fraction of the vapor of component i at the surface of the droplet. $p_{\mathrm{vap},i}$ is the vapor pressure of the component i. For the hydrous ethanol system containing ethanol solvent and water solute, minimal discrepancies are observed between Raoult's law and the UNIFAC (universal quasichemical functional group activity coefficients) method, as documented in [144, 159]. Similarly, no significant differences are noted for the TTIP/p-xylene precursor solution either [111].

2.2.5 Chemical Kinetics and Physical Properties

In the counterflow configuration, air functions both as the carrier gas on the spray side and as the oxidizer on the gas side. The monocomponent droplet spray system uses ethanol as fuel, chosen for its environmental and economic advantages [13, 14, 15, 16] as well as its well-established chemical reaction mechanisms [24]. For multicomponent droplet spray systems, the research examines hydrous ethanol and TTIP/p-xylene precursor solution droplets. These investigations aim to understand the complex behaviors and interactions within monocomponent and multicomponent droplet spray flames in the studied configuration.

The reaction scheme for ethanol in air, adopted from Chevalier [24], specifically addresses the ethanol–air system under the atmospheric pressure condition. This mechanism includes 38 species and 337 elementary reactions. It provides a comprehensive framework

for understanding and modeling the combustion characteristics of ethanol-air mixtures, enabling detailed analysis of combustion dynamics and reaction pathways. This mechanism has proven effective in predicting ignition delay time and laminar flame speeds in gas flames and has been successfully applied in studies examining ignition delay for monodisperse ethanol–air sprays, as noted in Chevalier [24]. Furthermore, it has been successfully utilized in various studies of ethanol/air spray combustions, as referenced in [25, 26, 27, 28, 29]. These applications underscore the mechanism's robustness and versatility in addressing complex combustion phenomena. The properties of the gas phase and gas mixtures are sourced from Kee et al. [153]. The liquid properties of ethanol are evaluated according to the methodologies described by Poling et al. [160]. Specifically, the Clausius-Clapeyron relation is utilized to determine the phase transition between the liquid and gas states of ethanol. Additionally, the gas phase is assumed to behave as an ideal gas in these analyses.

For the hydrous ethanol system, the detailed chemical kinetics follow the same scheme as the pure ethanol/air system, given that the species H_2O is already included in the model. The variable thermophysical properties of ethanol in both the liquid and gas phases are derived from studies cited in [28, 29], while the properties for water are sourced from [161]. The overall liquid and gas mixture properties utilized in the model are taken from Poling et al. [160]. For calculating the thermal conductivity of the liquid mixture, the Jamieson correlation is employed, whereas the thermal conductivity of the gas mixture is evaluated using the Wassiljewa equation, which provides a reliable method for calculating this property in complex gas mixtures. The viscosity of the gas mixture in the film is computed following Wilke's rule. This rule offers an empirical approach for estimating mixture viscosities based on individual component viscosities. Diffusivity measurements for ethanol vapor in air and water vapor in air are determined using the Fuller equation and the Chapman and Enskog equation, respectively, ensuring a comprehensive approach to modeling the physical properties essential for accurate simulation of multicomponent droplet dynamics and interactions.

For the TTIP and p-xylene precursor solution system, the detailed chemical reaction mechanism for TTIP and p-xylene in air includes a complex network of 213 chemical reactions involving 52 species [162]. This detailed mechanism helps accurately model the combustion and interaction behaviors of this specific chemical system under various conditions, providing a robust framework for understanding the kinetics and dynamics of TTIP and p-xylene reactions in air. The chemical reaction mechanism for p-xylene, originally proposed by Ranzi et al. [163], was subsequently reduced by Nanjaiah and Wlokas [162]. This reduction aimed to streamline the model while maintaining accuracy in predicting key combustion characteristics. Nanjaiah and Wlokas [162] then validated this reduced reaction scheme by comparing its predictions of laminar flame speed and ignition delay time against

both the numerical results from Ranzi et al. [163] and experimental data from Ji et al. [164]. For TTIP, thermal decomposition is a key process considered in FSP. The primary decomposition product from TTIP under thermal conditions is titanium hydroxide, $Ti(OH)_4$, which forms through the abstraction pathways involving CH_3- and C_3H_6-groups. This decomposition mechanism has been detailed in studies by Buerger et al. [165] and Lindberg [114, 115], providing a solid foundation for understanding the chemical transformations of TTIP in thermal environments.

The characteristic thermophysical properties of the TTIP and p-xylene are provided in Table 2.1. The variable liquid properties of a mixture of TTIP and p-xylene at atmospheric pressure were systematically measured by Keller et al. [110]. Their research provides valuable data that enhance the understanding of the physical characteristics of this mixture under standard atmospheric conditions. This information is critical for accurately simulating and modeling processes that involve the handling or use of TTIP and p-xylene in industrial applications, particularly those related to chemical synthesis and materials processing. The mixture properties of TTIP and p-xylene in the gas phase are sourced from the comprehensive work by Poling et al. [160]. Specifically, the thermal conductivity of the gas mixture is evaluated using the Wassiljewa equation. The viscosity of the gas mixture, particularly in the film, is calculated using Wilke's rule. Diffusivity of TTIP vapor and p-xylene vapor in air is determined using the Fuller equation [166], which is widely recognized for its accuracy in predicting binary diffusion coefficients. Vapor pressures of p-xylene and TTIP are calculated using the Antoine equation [110], a well-established method for determining the pressure at which a liquid turns into vapor.

Table 2.1: The thermophysical properties of p-xylene and TTIP at standard conditions of 1 bar and 300 K, adopted from the dataset provided by Keller et al. [110] if not specified otherwise.

Properties	Unit	p-xylene	TTIP
Density ρ	kg/m^3	852.2	952.8
Molecular mass, M	kg/mol	0.106	0.284
Specific heat capacity c_p	kJ/kg·K	1.745	1.620
Thermal diffusivity α	m^2/s	8.423×10^{-8}	8.405×10^{-8}
Boiling temperature T_{boil}	K	411.52	505.00
Critical temperature T_{crit}	K	616.2 [167]	641.0 [168]
Latent heat of vaporization L	kJ/kg	3.962×10^2 [169]	2.192×10^2 [169]

2.2.6 Numerical Solution

This simulation study addresses the solution of a closed system of strongly coupled equations numerically, drawing on methodologies outlined in [46, 47] to obtain the structures of laminar spray flames of monocomponent and multicomponent droplets within the counterflow configuration. The strongly coupled equations are resolved using a hybrid computational scheme that integrates the gas and liquid phases, where a cental finite difference scheme is employed, which can be derived by considering an expansion in the Taylor series. After the discretization of the governing differential equations, a system of algebraic equations is derived. These equations can be solved using the Thomas algorithm, also known as the Tri-Diagonal Matrix Algorithm (TDMA) [170]. Notably, the computational code was developed and extended by incorporating the transformed gas phase equations and non-dimensional liquid phase equations as well as spray source terms. Initially, the liquid phase equations (Eqs. 2.37–2.40) are computed with specific accompanying calculations, including the Spalding transfer numbers and vapor-liquid equilibrium analysis. Subsequently, the gas phase source terms are evaluated following Eqs. 2.51 to 2.53. The gas phase equations (Eqs. 2.24- 2.27) are then computed, incorporating comprehensive solutions of chemical reactions based on the detailed chemical kinetics of the systems under consideration, which typically require about 100 iterations before revisiting the liquid phase equations. A typical computation undergoes approximately 100–1000 cycles until convergence is determined by achieving a relative error of 10^{-4}, with the exact number depending on the variations in initial conditions from previous computations. Ultimately, the non-dimensional data results are converted to dimensional form using reference values for enhanced comprehension and visualization.

The numerical model used for monocomponent droplet spray had been validated previously for an n-heptane/oxygen flame as detailed in Gutheil and Sirignano [47], and subsequently extended to study ethanol/air spray flames as discussed in further studies [26, 47, 55, 158]. This dissertation presents further extensions concerning the multiple structures of laminar non-premixed ethanol/air spray flames in the counterflow configuration, particularly under fuel-rich conditions. Additionally, it incorporates a multicomponent heating and evaporation model to enhance applicability to more complex systems with multiple chemical components. This extended model is validated using hydrous ethanol spray flames, as detailed in Subsection 3.2.1.

Different flame structures under identical boundary conditions are achieved through a series of simulations. Initially, simulations are conducted at low strain rates, resulting in flame structures characterized either by a single reaction zone or by dual reaction zones. Upon increasing the gas strain rate, a transition to alternative flame structures is observed

at elevated strain rates. Subsequently, a reduction in strain rate from this elevated state typically maintains the existence of these structures at low strain rates in most instances; however, occasionally, it leads to a transition to a different structure. This methodology outlines the coexistence of three distinct flame structures under the same initial and boundary conditions at low strain rates. The comprehensive findings will be discussed in Chapter 3.

3. Results and Discussions

This chapter offers an extensive examination and findings derived from numerical simulations of monocomponent anhydrous ethanol, as well as multicomponent hydrous ethanol and TTIP/p-xylene droplet spray laminar flames in a counterflow configuration. The methodologies for bicomponent droplet spray combustion modeling discussed in Subsection 2.2.4 are applicable to multicomponent droplet spray systems. Thus, the terms 'bicomponent' and 'multicomponent' are used interchangeably in this context. As the schematic diagram shown in Fig. 1.3, the monocomponent or multicomponent droplet spray with carrier gas air is injected from the left side of the configuration and directed against an opposed air flow. The gas flow field considered here is steady, the Lagragnian description of the droplets is unsteady.

In all cases considered in this chapter, all air streams and liquid fuel are at ambient temperature of 300 K and an atmospheric pressure. The initial droplet velocity consistently matches the gas velocity on the left side of the configuration. Different cases exhibit variations in equivalence ratio, strain rate at the spray side of the configuration, and initial droplet radius. Specific boundary and initial conditions for each case are detailed as necessary in the corresponding subsections.

The investigation initially explores the observed double structures within ethanol spray flames under various gas strain rates and equivalence ratios, focusing on initial droplet radii of $R_0 = 30\,\mu\text{m}$ and $R_0 = 50\,\mu\text{m}$, as reported by Ying et al. [28]. This is followed by an examination of triple structures at different gas strain rates and equivalence ratios with droplet radii ranging from $R_0 = 10\,\mu\text{m}$ to $R_0 = 30\,\mu\text{m}$, including detailed discussions on their transition mechanisms. This part of discussion is adapted from the work by Ying and Gutheil [29, 58]. Furthermore, the discussion extends to laminar spray flames of hydrous ethanol droplets, showcasing a comprehensive Eulerian-Lagrangian methodology for analyzing multicomponent droplet spray flames. The chapter concludes with an analysis of the results for TTIP/p-xylene spray flames, enhancing the understanding of precursor solution modeling and subsequent combustion in nanoparticle formation within the framework of FSP, as discussed by Ying and Gutheil [141].

3.1 Ethanol Spray Flames

In this section, flame structures of laminar non-premixed ethanol/air spray in a counterflow configuration are analyzed under fuel-rich conditions. The study focuses on the phenomena of double and triple flame structures, which occur under specific operational conditions determined by the gas strain rates and droplet sizes.

Double flame structures will be discussed in Subsection 3.1.1. These structures are observed under different gas strain rates and equivalence ratios, with initial droplet radii of $R_0 = 30\,\mu m$ and $R_0 = 50\,\mu m$. The results are incorporated into a regime diagram that categorizes the conditions for the formation of double and single flame structures and defines the limits at which flame extinction occurs. This discussion is based on the findings reported by Ying et al. [28]. Triple flame structures will be discussed in Subsection 3.1.2. These structures are identified at various gas strain rates and equivalence ratios, with droplet radii smaller than $30\,\mu m$. This part of the discussion is adapted from the work of Ying and Gutheil [29, 58]. The triple flame structures exhibit a more complex interaction between the evaporating fuel and oxidizing air, resulting in three distinct zones of chemical reactions. The transition mechanism between these structures is a critical aspect of the study. It involves understanding how variations in physical parameters like strain rate and droplet size influence the flame dynamics and structures. The transition is influenced by the balance between the chemical kinetics of the fuel-air reactions and the physical dynamics of spray dispersion and heat transfer.

3.1.1 Double Flame Structures

This study analyzes the double flame structures of laminar non-premixed ethanol/air spray flames in a counterflow configuration. Utilizing a monodisperse liquid fuel spray with carrier gas air directed against an opposing airstream, the study outlines distinct flame structures under consistent boundary and initial conditions. Two principal spray flame structures are outlined: the first exhibits two distinct chemical reaction zones positioned on either side of the gas stagnation plane, facilitating complex interactions between evaporating fuel and oxidizing air, thereby influencing combustion dynamics. The second structure is characterized by the absence of a spray-sided flame, with combustion confined entirely to the gas side, resulting in distinctly separate evaporation and combustion zones, which alters the dynamics of heat and mass transfer. Parametric studies varying the equivalence ratio from 1.1 to 1.8, gas strain rates on the spray side up to 55/s, and initial droplet sizes ranging from 10 µm to 50 µm were conducted to deepen understanding of these phenomena. The findings are integrated into a regime diagram categorizing the conditions under which the development of

double and single flame structures is, as well as defining the limit at which flame extinction occurs. This subsection concludes with an analysis of the physical mechanisms underlying the formation and breakup of these double flame structures.

Characteristics and Parametric Study of Double Spray Flame Structures

In the forthcoming analysis, the influence of strain rate, equivalence ratio, and initial droplet size on the configuration of spray flame structures will be investigated.

Figures 3.1 and 3.2 present two distinct structures of a monodisperse ethanol spray flame, driven by carrier air and directed against an opposing airstream under specific conditions: a spray-sided gas strain rate of $a_{-\infty} = 55$/s, gas velocity of 0.44 m/s, initial gas and liquid temperatures of 300 K, an initial droplet radius of 50 µm, and an equivalence ratio $E_{-\infty} = 1.5$, all maintained at atmospheric pressure. In the depicted figures, the configuration introduces the spray mixed with carrier gas air from the left, while pure air counterflows from the right. The axial position $y = 0$ mm is designated as the gas stagnation plane. Part (a) of each figure illustrates the profiles for normalized droplet size R/R_0, gas temperature T_g, and the mass fractions Y_k of select chemical species. Conversely, part (b) of the figures displays the normalized droplet size and gas temperature alongside the velocities of the gas v_g and droplets v_d, as well as the mass evaporation rate S_v of the spray. Notably, the droplets either reverse or oscillate, resulting in locally polydisperse spray conditions characterized by varied droplet velocities.

Figure 3.1b illustrates the evaporation zone on the spray side of the configuration, discernible from the profile of the mass evaporation rate, denoted as S_v. The axial position marked by $y = 0$ mm indicates the location of the gas stagnation plane, as also highlighted

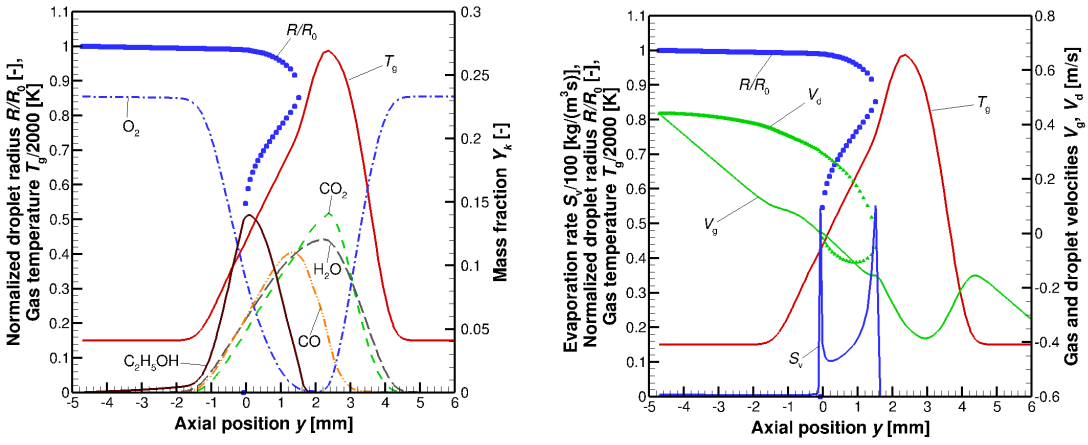

(a) Outer flame structure

(b) Spray characteristics

Figure 3.1: Spray flame structure with one reaction zone for $R_0 = 50$ µm, $E_{-\infty} = 1.5$, $v_0 = 0.44$ m/s, $T_{\mathrm{l},0} = T_{\mathrm{g},0} = 300$ K, $a_{-\infty} = 55$/s [28].

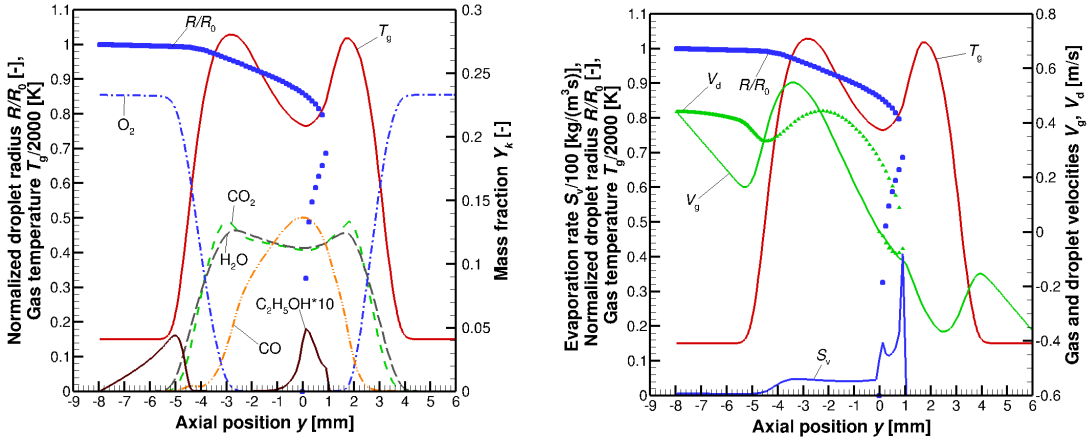

(a) Outer flame structure

(b) Spray characteristics

Figure 3.2: Spray flame structure with two reaction zones for $R_0 = 50\,\mu\text{m}$, $E_{-\infty} = 1.5$, $v_0 = 0.44$ m/s, $T_{\text{l},0} = T_{\text{g},0} = 300$ K, $a_{-\infty} = 55$/s [28].

on the right part of the figure. This evaporation zone extends into the gas side of the configuration, resulting in a peak in the mass evaporation rate profile at the droplet reversal position, approximately at $y = 1.6$ mm.

The chemical reaction zone is predominantly situated on the gas side of the counterflow configuration, while the evaporation and combustion zones are largely detached within the setup. Significant evaporation occurs near the droplet reversal point and close to the stagnation plane, as indicated by the profile of the spray evaporation rate, S_{v}. This pattern is attributed to the accumulation of droplets at these locations, resulting from their reduced velocities and correspondingly extended residence times. The concentration of fuel vapor peaks near the gas stagnation plane. The distinct profiles of gas and droplet velocities reveal that while the droplets experience two stagnation points, the gas phase encounters only one, a characteristic typical of counter-flowing gas combustion systems. The byproducts of the chemical reactions, such as H_2O and CO_2, are predominantly found in the regions of high gas temperatures, as shown in Fig. 3.1a.

Figure 3.2 presents a spray flame structure markedly different from that described in Fig. 3.1, despite identical initial and boundary conditions. While the chemical reaction zone on the gas side has a high resemblance to that observed in Fig. 3.1, the overall configuration diverges significantly. Notably, an additional chemical reaction zone on the spray side contributes to a substantial broadening of the spray flame width, expanding from approximately 6 mm to about 9 mm. The predominant evaporation zone of the spray is wider, and the profiles of chemical reaction products generally mirror those of the gas temperature, displaying two local maxima. An exception is observed in the profile of CO, which peaks in the cooler gas temperature region situated between the two chemical reaction zones, where

the temperature is insufficient to fully convert CO into CO_2. Additionally, the fuel vapor mass fraction exhibits a local maximum in the area of the gas temperature's local minimum near the stagnation plane, resulting in a locally fuel-rich flame. In contrast, configurations with a single chemical reaction zone, as seen in Fig. 3.1, demonstrate that gaseous fuel near the gas stagnation plane remains unburnt due to low gas temperatures, thereby inhibiting flame sustainability. This condition conversely discourages vaporization within that region of the spray flame, leading to fuel vapor mass fractions as high as approximately 0.14 in the main evaporation zone, as evidenced by the profile of S_v in Fig. 3.1b.

As the gas strain rate on the spray side of the configuration is increased, the two distinct spray flame structures previously discussed remain stable up to a gas strain rate of 230/s. Beyond this rate, the structure initially characterized by a single chemical reaction zone transitions into a double flame structure, which is identical to the one initially having two chemical reaction zones. Therefore, the presence of these double flame structures, considering an initial droplet radius of 50 µm and an equivalence ratio of 1.5, is maintained within a range of gas strain rates from 55/s to 230/s on the spray side of the configuration.

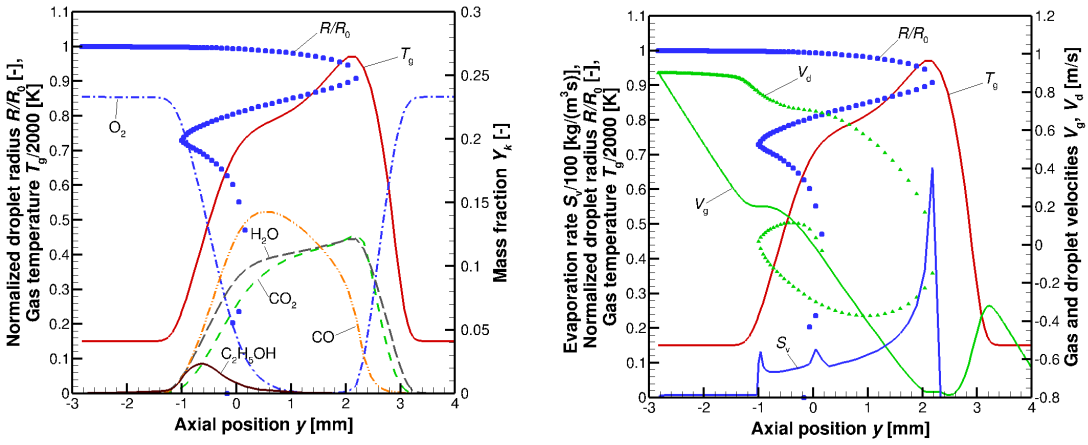

(a) Outer flame structure

(b) Spray characteristics

Figure 3.3: Spray flame structure with one reaction zone for $R_0 = 50\,\mu m$, $E_{-\infty} = 1.5$, $T_{l,0} = T_{g,0} = 300$ K, $a_{-\infty} = 230$/s [28].

Figures 3.3 and 3.4 illustrate the flame structures at a gas strain rate of 230/s for configurations with one and two chemical reaction zones, respectively. The most notable difference in the two-zone structures is the significant reduction in flame thickness, decreasing from approximately 9 mm in Fig. 3.2 to just over 5 mm in Fig. 3.4, whereas the structures with a single chemical reaction zone exhibit minimal changes, as shown in Figs. 3.1 and 3.3. In the single flame configuration, the vaporization zone becomes considerably broader with the increased strain rate, and the droplets experience a dual reversal, penetrating deeper into the incoming spray stream. The chemical reaction zone and the evaporation zone overlap

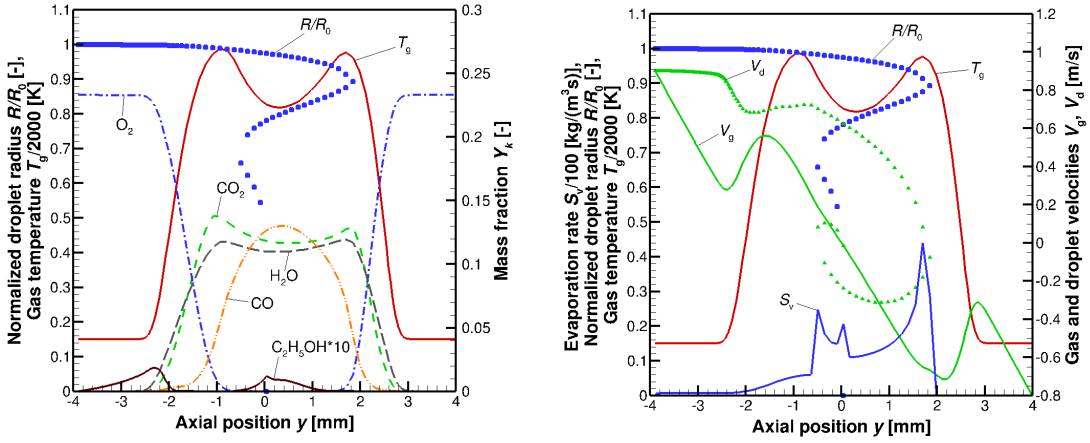

(a) Outer flame structure

(b) Spray characteristics

Figure 3.4: Spray flame structure with two reaction zones for $R_0 = 50\,\mu\text{m}$, $E_{-\infty} = 1.5$, $T_{l,0} = T_{g,0} = 300$ K, $a_{-\infty} = 230$/s [28].

significantly, with droplets residing within the hottest zone of the flame at approximately 2 mm, thereby enhancing chemical reactions. In Fig. 3.3, on the spray side of the single reaction zone, droplets exiting the chemical reaction zone contribute to a shoulder in the gas temperature profile, enhancing both chemical reactions and vaporization. This results in a lower peak in the C_2H_5OH vapor mass fraction compared to the lower strain scenario. Figure 3.4 demonstrates that droplets also penetrate into the hottest temperature region on the gas side of the configuration in the two-zone structure, enhancing vaporization as evidenced by the mass evaporation rate profile S_v in Fig. 3.4b. The mass evaporation rate displays three peaks, two at the positions of droplet reversal and a third at the stagnation plane, where all droplets eventually evaporate completely. In contrast, the spray flame structures with a single chemical reaction zone are characterized by an evaporation regime that, following droplet reversal, remains physically distinct from the high-temperature region of the gas flame.

At gas strain rates exceeding 230/s, the distinct spray flame structures characterized by single and double chemical reaction zones cease to exist, converging into a unified double flame structure. This convergence results in a unique numerical solution of the governing equations, signifying a critical transition in the behavior of the flame under elevated strain conditions.

Figures 3.5 and 3.6 illustrate the evolution of the spray flame structure at gas strain rates of $a_{-\infty} = 300$/s and $a_{-\infty} = 550$/s, respectively. As the strain rate increases, the spray flame narrows and penetrates deeper into the configuration. Notably, at the highest examined strain rate of 550/s, which is proximate to the extinction point at 555/s, the spray evaporation zone on the gas side of the configuration is positioned outside of the chemical reaction

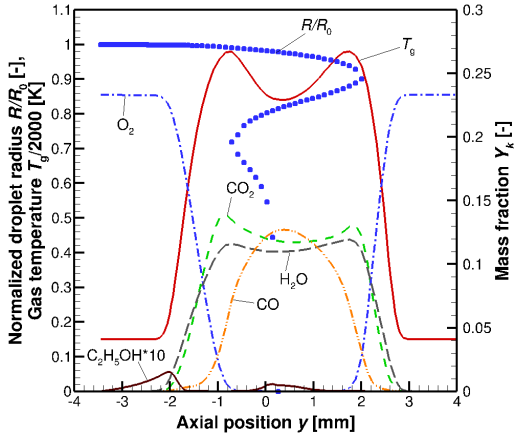

(a) Outer flame structure

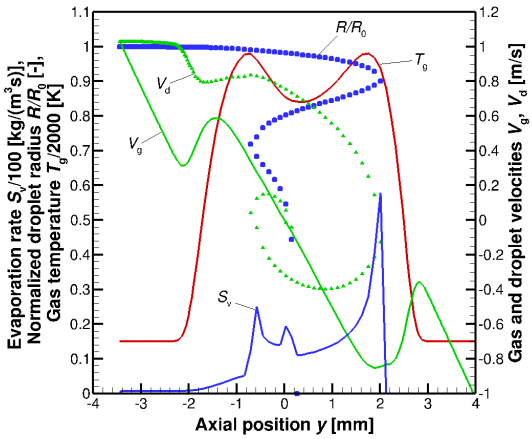

(b) Spray characteristics

Figure 3.5: Spray flame structure for $R_0 = 50$ µm, $E_{-\infty} = 1.5$, $T_{l,0} = T_{g,0} = 300$ K, $a_{-\infty} = 300$/s [28].

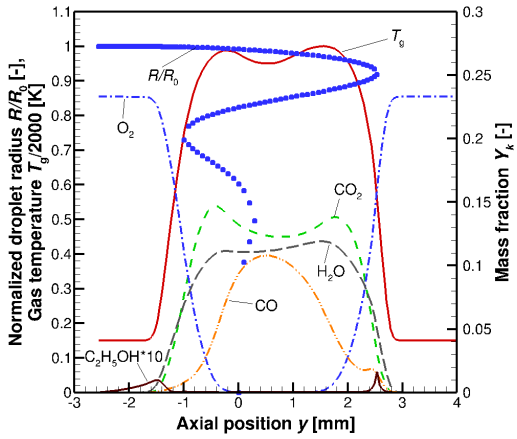

(a) Outer flame structure

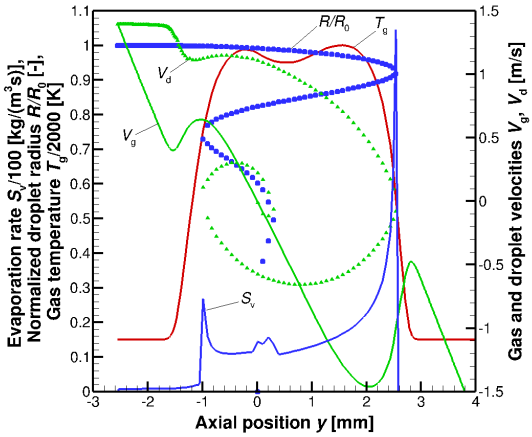

(b) Spray characteristics

Figure 3.6: Spray flame structure for $R_0 = 50$ µm, $E_{-\infty} = 1.5$, $T_{l,0} = T_{g,0} = 300$ K, $a_{-\infty} = 550$/s [28].

zone. This displacement is evident in Fig. 3.6b, where the peak of the mass evaporation rate is located outside the chemical reaction zone. This positioning implies that the spray flame cannot be sustained at this high strain rate, as the evaporated droplets with significant momentum exit the reaction zone. The strain rate of the initial spray exceeding 555/s leads to flame extinction, which is not primarily due to reduced chemical reaction time—common in typical gas combustion extinction—but rather due to a breakdown in spray evaporation. This breakdown results from insufficient energy being available from the combustion process to sustain the flame, indicating a unique extinction mechanism in spray combustion.

Although spray flames in the counterflow configuration manifest in multiple structures

under both stoichiometric [136] and fuel-rich conditions, their structural characteristics and extinction mechanisms significantly differ. In stoichiometric spray flames, structures with a single chemical reaction zone exhibit physically overlapping vaporization and chemical reaction zones. In contrast, these zones are distinctly separated in fuel-rich flames. Notably, while multiple structures converge at elevated strains in both flame types, stoichiometric spray flames typically combine into a single chemical reaction zone, whereas fuel-rich flames are characterized by dual reaction zones. The extinction of stoichiometric spray flames is primarily attributed to the breakdown of chemical reactions. Conversely, in fuel-rich flames, extinction occurs as the vaporization of droplets ceases when the spray exits the chemical reaction zone, thereby disrupting vaporization due to insufficient energy from gas combustion.

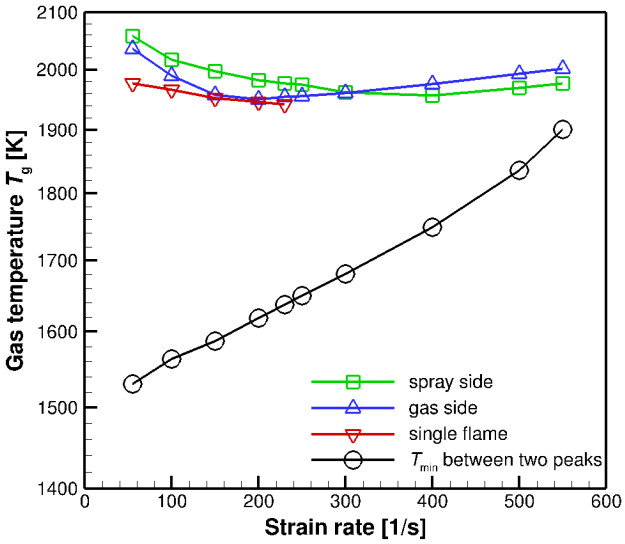

Figure 3.7: Maximum gas temperature and local minimum gas temperatures versus strain rate for the multiple spray flames for $E_{-\infty} = 1.5$ and $R_0 = 50\,\mu$m [28].

Figure 3.7 summarizes the local minimum and maximum flame temperatures versus the gas strain rate for the cases under investigation. It displays both local maxima and the local minimum between them for flames with two reaction zones, while only a single maximum is shown for flames with one reaction zone. The peak temperature of the single flame structure (denoted by downward triangles) consistently remains lower than that of the two-reaction-zone flames (upward triangles for gas-sided peaks and squares for spray-sided peaks). This lower temperature in single-zone flames results from the substantial energy required to sustain evaporation within the zone. As the strain rate increases, the greater momentum of the droplets allows deeper penetration into the gas-sided chemical reaction zone, thus feeding more fuel vapor into this region and enhancing combustion. This is reflected by a shift in the peak flame temperature from the spray to the gas side at a

strain rate of approximately $a_{-\infty} = 300/\text{s}$. The circles in Fig. 3.7 denote the local minimum temperatures between the maximum gas temperatures in two-peak structures, which increase and output the dip in the gas temperature profile less pronounced as the strain rate rises. This change is due to the narrowing of the spray flame and the more uniform profile of the mass evaporation rates observed in Figs. 3.5b and 3.6b.

In flame structures with a single chemical reaction zone, the distinct chemical reaction and evaporation zones are interdependent: evaporation feeds the chemical reactions through spray vaporization, while heat release from these reactions provides the energy necessary for further spray evaporation. This interdependence may explain phenomena such as flame pulsation [171] or micro-explosions of droplets observed in experiments [108, 172]. It is crucial that the model accounts for both droplet reversal and oscillation to accurately capture the temperature effects in chemical reaction zones.

The subsequent analysis explores the impact of varying the equivalence ratio and initial droplet size of the mono-disperse spray on the structure of spray flames.

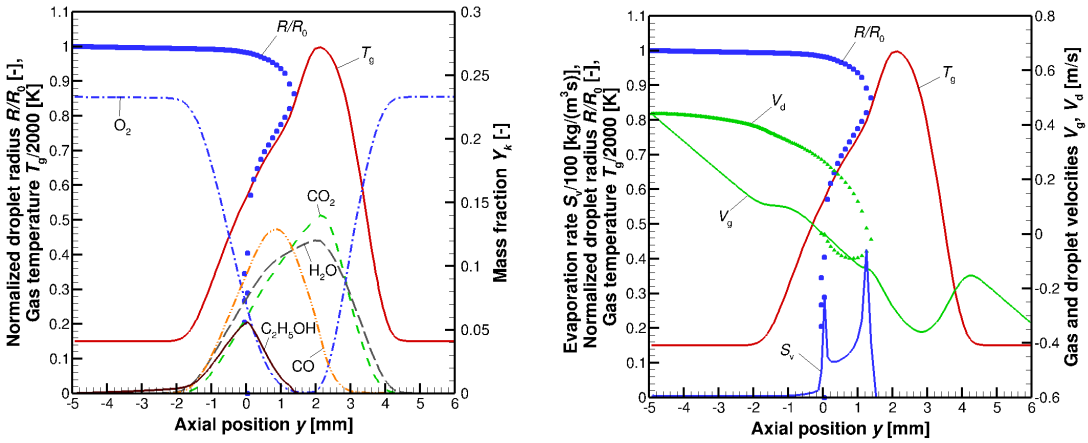

(a) Outer flame structure

(b) Spray characteristics

Figure 3.8: Spray flame structure with one reaction zone for $R_0 = 50\,\mu\text{m}$, $E_{-\infty} = 1.2$, $v_0 = 0.44$ m/s, $T_{l,0} = T_{g,0} = 300$ K, $a_{-\infty} = 55/\text{s}$ [28].

Figures 3.8 through 3.9 and 3.10 through 3.11 represent the flame structures at equivalence ratios of 1.2 and 1.8, respectively. These ratios represent values both below and above the baseline discussed in the former subsection. These figures offer insights into how variations in equivalence ratios influence the behavior of the spray flames under similar operational conditions. These figures should be interpreted alongside Figs. 3.1 and 3.2, which represent the flame structures at an equivalence ratio of 1.5, situated between the conditions depicted in the earlier figures.

In spray flame structures with a single chemical reaction zone, the most notable variation across different equivalence ratios is observed in the peak mass fraction of the fuel vapor,

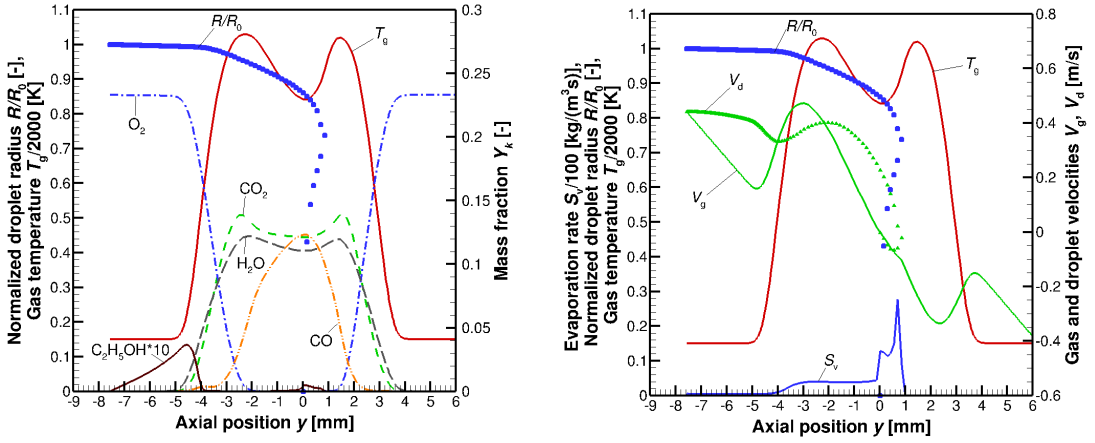

(a) Outer flame structure (b) Spray characteristics

Figure 3.9: Spray flame structure with two reaction zones for $R_0 = 50\,\mu\text{m}$, $E_{-\infty} = 1.2$, $v_0 = 0.44$ m/s, $T_{l,0} = T_{g,0} = 300$ K, $a_{-\infty} = 55$/s [28].

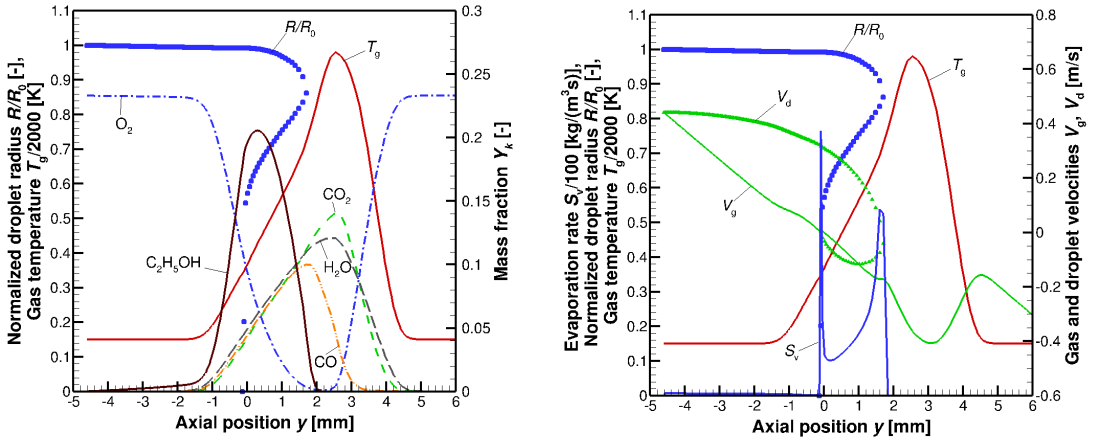

(a) Outer flame structure (b) Spray characteristics

Figure 3.10: Spray flame structure with one reaction zone for $R_0 = 50\,\mu\text{m}$, $E_{-\infty} = 1.8$, $v_0 = 0.44$ m/s, $T_{l,0} = T_{g,0} = 300$ K, $a_{-\infty} = 55$/s [28].

which increases approximately fourfold with higher equivalence ratios. Simultaneously, the peak of the CO mass fraction shifts toward the center of the chemical reaction zone and exhibits a slight decrease. This movement is due to the peak occurring in a higher temperature region, which facilitates the temperature-dependent chemical reaction CO + OH $\rightleftharpoons$ CO_2 + H. Despite these changes in chemical composition, the overall width of the spray flame remains largely unaffected by the increase in equivalence ratio. However, the necessity for greater evaporation of the increased spray mass is reflected by a slight reduction in flame temperature and a significant rise in unburnt fuel vapor within the major evaporation zone, along with a less pronounced temperature shoulder on the left side of the

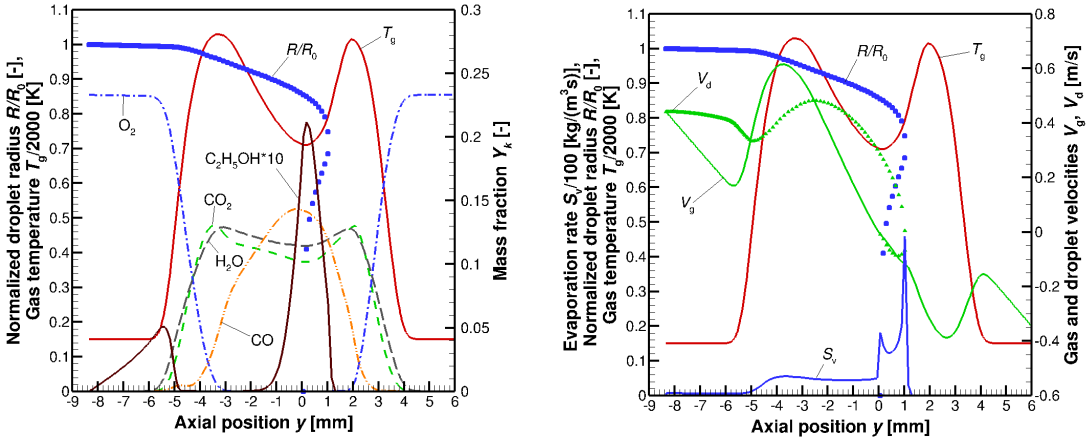

(a) Outer flame structure

(b) Spray characteristics

Figure 3.11: Spray flame structure with two reaction zones for $R_0 = 50\,\mu\text{m}$, $E_{-\infty} = 1.8$, $v_0 = 0.44$ m/s, $T_{l,0} = T_{g,0} = 300$ K, $a_{-\infty} = 55$/s [28].

gas temperature profile.

In configurations with two reaction zones, a higher equivalence ratio and correspondingly greater droplet number density cause the droplets to penetrate more deeply into the gas-sided reaction zone. This deeper penetration leads to a lower minimum temperature between the temperature peaks. As a result, more fuel vapor accumulates in this region, and the mass evaporation rate is elevated, as evidenced in Figs. 3.9b and 3.11b. This change results in a considerable broadening of the overall spray flame structure. These dynamics illustrate how variations in the equivalence ratio not only affect the chemical behavior within the zones but also significantly influence the physical characteristics of the flame.

Figure 3.12 depicts the peak flame temperatures (triangles up for the gas side, and squares for the spray side) alongside the local minimum gas temperature between these peaks (circles), and the peak temperature of the single flame structure (triangles down). These data are plotted against the equivalence ratio, $E_{-\infty}$, for both one and two reaction zone flame structures, maintaining a constant initial droplet size of 50 µm and a gas strain rate of 55/s. Notably, the minimum gas temperature between the peaks decreases with an increase in equivalence ratio, while the peak temperatures remain relatively constant.

This consistency in peak temperatures, despite higher equivalence ratios, is attributed to the excess fuel that cannot be burned due to an insufficient supply of oxygen, resulting in nearly constant flame temperatures. The increased need for energy to vaporize more liquid fuel is reflected in the decline of the local minimum gas temperature, which decreases from about 1750 K at $E_{-\infty} = 1.1$ to approximately 1420 K at $E_{-\infty} = 1.8$. As previously discussed in the context of rising strain rates in Fig. 3.7, the maximum temperature of the single flame structure consistently registers lower compared to that of the two-peak structure.

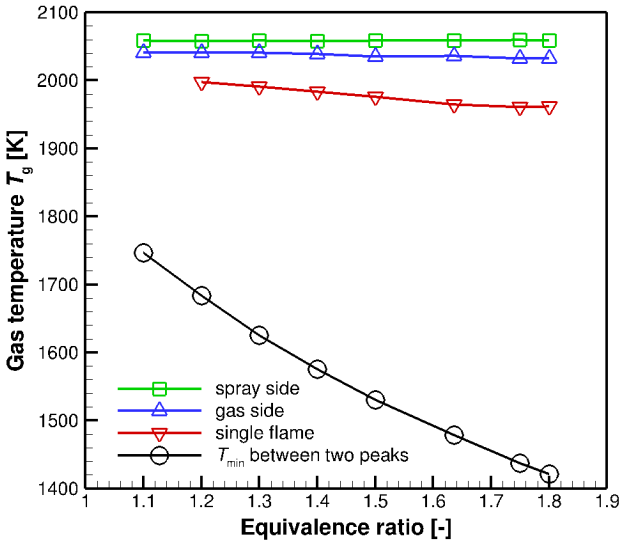

Figure 3.12: Maximum and local minimum gas temperatures versus equivalence ratio for the multiple spray flames for $a_{-\infty} = 55$/s and $R_0 = 50$ µm [28].

The analysis of these flame structures shows that while the gas-sided chemical reaction zone remains relatively unchanged with higher equivalence ratios, the increased liquid mass, evident in the droplet number density, results in a higher fuel vapor mass fraction near the stagnation plane. This contributes to the observed decrease in the minimum gas temperature as the equivalence ratio increases. The consistency in the structure of the gas-sided chemical reaction zone aligns with findings from an earlier study by Gutheil et al. [26], which demonstrated that the chemical reaction zone on the gas side of the counterflow configuration could effectively be replaced by a gas flamelet in models of turbulent spray combustion. This replacement facilitates the use of simplified flamelet structures in complex combustion modeling, providing a robust framework for predicting the behavior of spray flames under varied operational conditions.

The variation in the initial droplet radius from 5 µm to 50 µm significantly impacts the interaction between the spray and the flame structures within the counterflow configuration. As the droplet radius increases, both the momentum and the drag on the droplets increase. This results in a more pronounced influence of the spray on the flame structures, primarily because larger droplets can penetrate deeper into the counterflow configuration. For the smallest droplets at 5 µm, the droplets remain near the nozzle exit, and under these conditions, it is not possible to obtain a reasonable numerical solution due to limitations in capturing the dynamics of such small droplets effectively within the simulated environment. Consequently, the smallest initial droplet radius for which results are presented in this study is 10 µm. This ensures a more stable and interpretable outcome while maintaining all other parameters constant. This careful adjustment of droplet size parameters facilitates a

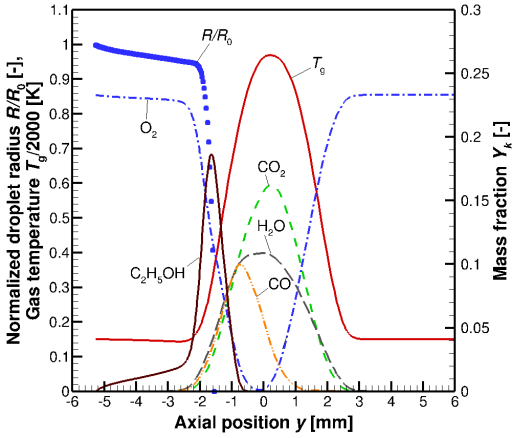

(a) Outer flame structure

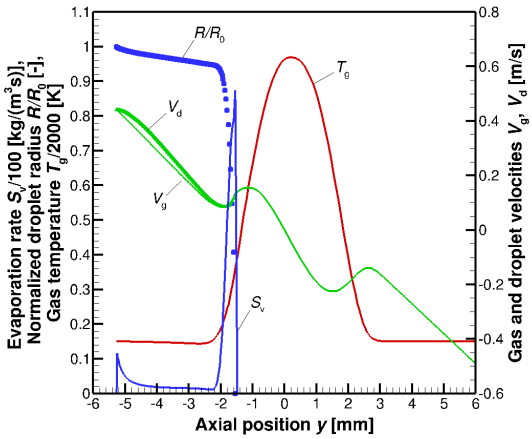

(b) Spray characteristics

Figure 3.13: Spray flame structure with one reaction zone for $R_0 = 10\,\mu\text{m}$, $E_{-\infty} = 1.5$, $v_0 = 0.44$ m/s, $T_{\text{l},0} = T_{\text{g},0} = 300$ K, $a_{-\infty} = 55$/s [28].

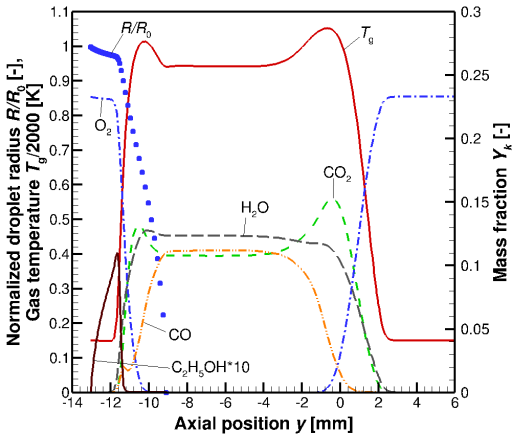

(a) Outer flame structure

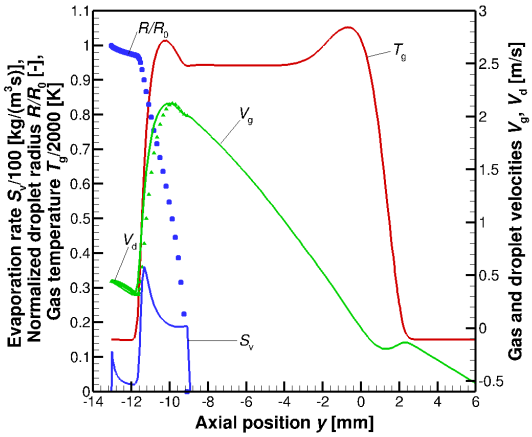

(b) Spray characteristics

Figure 3.14: Spray flame structure with two reaction zones for $R_0 = 10\,\mu\text{m}$, $E_{-\infty} = 1.5$, $v_0 = 0.44$ m/s, $T_{\text{l},0} = T_{\text{g},0} = 300$ K, $a_{-\infty} = 55$/s [28].

deeper understanding of the influence of droplet dynamics on the overall flame structure and behavior.

Figures 3.13 and 3.14 illustrate the flame structures for an initial droplet radius of 10 µm, showcasing single and double chemical reaction zones respectively. Notably, the scale of the physical coordinates in these figures varies, highlighting that the spray flame with two chemical reaction zones is more than twice as broad as its counterpart. Both configurations exhibit a relatively narrow evaporation zone; however, the chemical reaction zone in the double-zone configuration is significantly broader, a phenomenon attributed to the effects of diffusion and convection within this zone. This aspect and its implications will

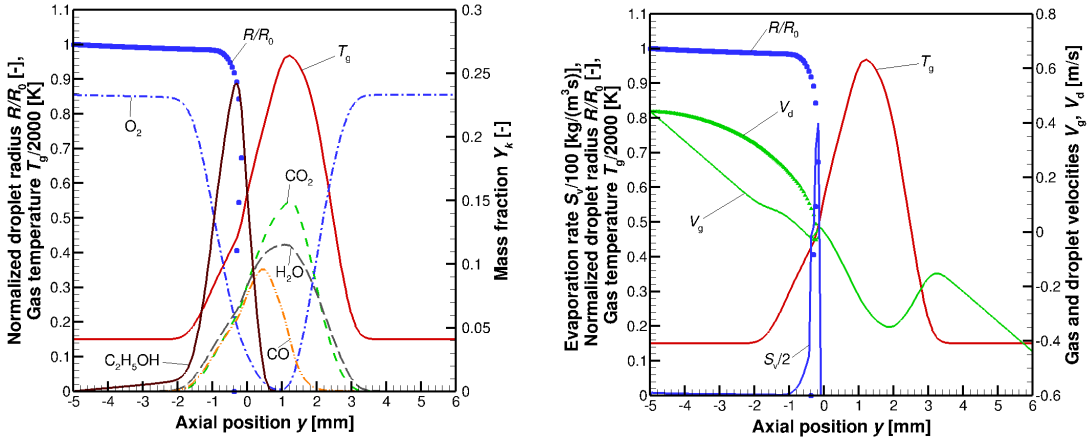

(a) Outer flame structure (b) Spray characteristics

Figure 3.15: Spray flame structure with one reaction zone for $R_0 = 30\,\mu\text{m}$, $E_{-\infty} = 1.5$, $v_0 = 0.44$ m/s, $T_{l,0} = T_{g,0} = 300$ K, $a_{-\infty} = 55$/s [28].

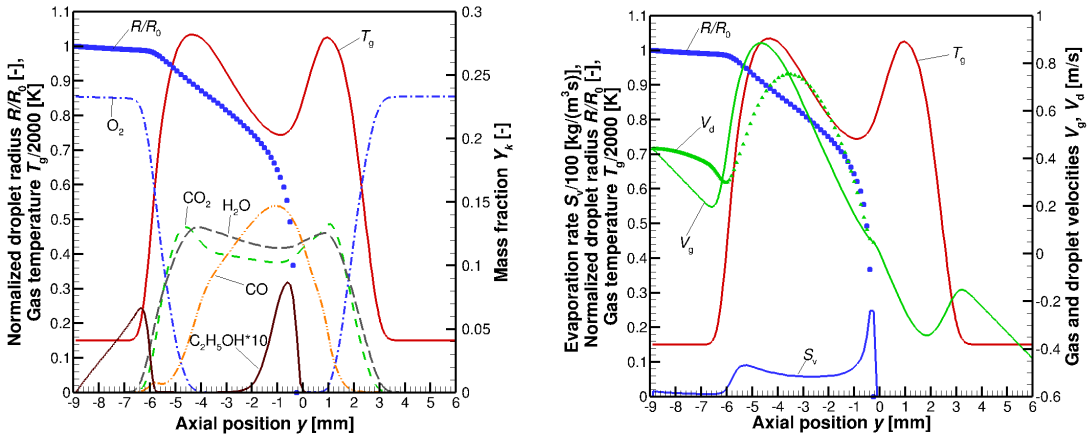

(a) Outer flame structure (b) Spray characteristics

Figure 3.16: Spray flame structure with two reaction zones for $R_0 = 30\,\mu\text{m}$, $E_{-\infty} = 1.5$, $v_0 = 0.44$ m/s, $T_{l,0} = T_{g,0} = 300$ K, $a_{-\infty} = 55$/s [28].

be discussed further in subsequent discussions. Interestingly, even though the vaporization regime in the double reaction zone scenario is positioned very close to the spray injection point, there remains a distinctly separated reaction zone near the stagnation plane. This separation is characteristic of gas combustion in a counterflow configuration and underscores the influence of the structural dynamics on flame behavior.

Upon increasing the initial droplet radius to 30 µm, as illustrated in Figs. 3.15 and 3.16, the resulting flame structures align closely with those observed with a 50 µm droplet radius discussed earlier. This similarity suggests that larger droplet sizes tend to stabilize the flame structure, making it less sensitive to variations in droplet size beyond a certain threshold.

The following subsection will summarize the conditions under which double spray flame structures can exist, consolidating the findings across different scenarios and parameter variations to provide a comprehensive overview of the factors influencing flame structure in spray combustion systems.

Regime Diagrams and Transition Mechanisms in Double Spray Flame Structures

The comprehensive parameter study encompassing over 200 simulations aims to delineate the conditions under which double flame structures can exist within a counterflow configuration. This analysis considers variables such as the initial droplet radius, the gas strain rate on the spray side, and the equivalence ratio. The findings from these simulations are contained in the regime diagrams presented in Figs. 3.17a and 3.17b, which respectively highlight results for initial droplet radii of 50 µm and 30 µm.

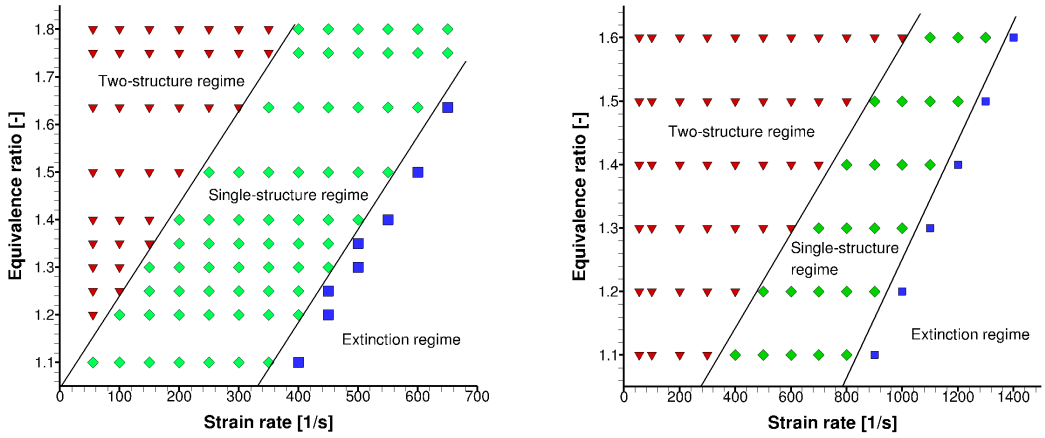

(a) $R_0 = 50\,\mu m$ (b) $R_0 = 30\,\mu m$

Figure 3.17: Regime diagrams of different flame structures [28].

In these regime diagrams, two black lines specify the boundaries between conditions leading to different structural outcomes: the existence of two distinct spray flame structures, a unique flame solution, and flame extinction. Notably, for the larger initial droplet size (50 µm), double structures are primarily observed at lower strain rates compared to those with a smaller initial droplet size (30 µm). Additionally, with an increase in strain rate, these structures persist across a broader range of equivalence ratios. Conversely, flames originating from the smaller initial droplet size generally exhibit greater stability, though it is posited that this stability might be specific to the droplet sizes currently under study.

This observation suggests that droplet size significantly influences flame behavior, with larger droplets fostering more distinct separation between flame structures at varied strain rates and equivalence ratios. The reasons for these differences have been discussed previ-

ously and involve aspects such as the width of the chemical reaction and vaporization zones. A more detailed investigation into these zones will provide deeper insights into the dynamics governing these flame structures and their stability under different operational conditions.

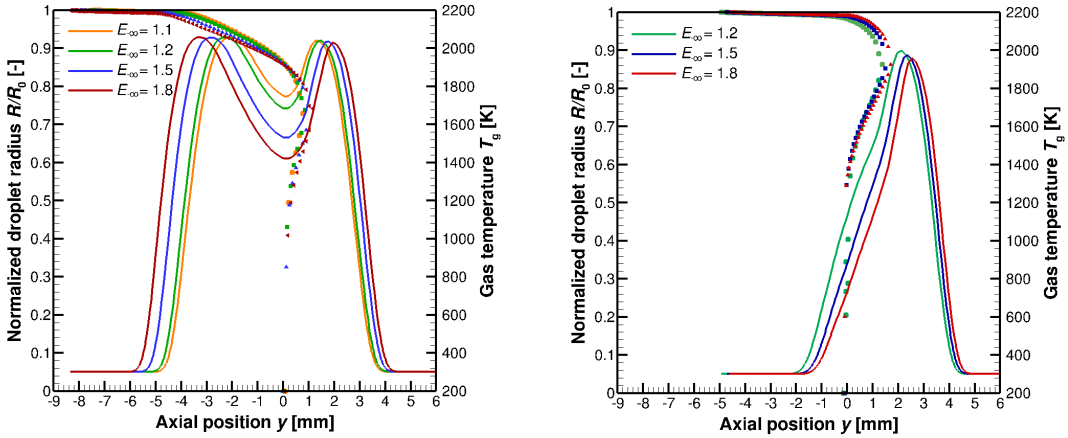

(a) Two chemical reaction zones (b) Single chemical reaction zone

Figure 3.18: Gas temperature and normalized droplet radius for a fixed strain rate of 55/s and $R_0 = 50$ µm for different equivalence ratios $E_{-\infty}$ [28].

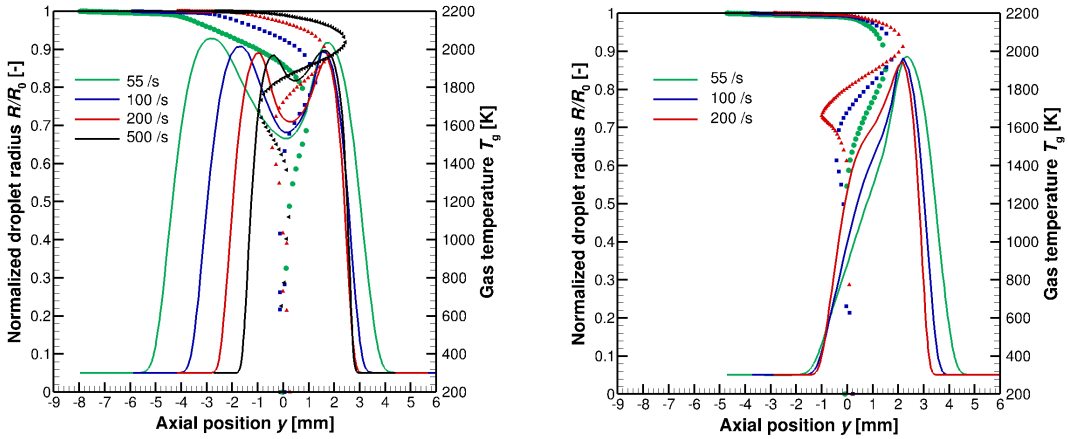

(a) Two chemical reaction zones (b) Single chemical reaction zone

Figure 3.19: Gas temperature and normalized droplet radius for initial strain rates from 55/s to 500/s and $R_0 = 50$ µm and $E_{-\infty} = 1.5$ [28].

Figure 3.18 presents the temperature profiles and normalized droplet radii in physical space for an initial droplet size of 50 µm and a gas strain rate of 55/s across various equivalence ratios. Interestingly, the equivalence ratio appears to have minimal impact on the width of the flame, the maximum flame temperatures, and the depth to which droplets penetrate the flame. The most significant effect of varying the equivalence ratio is observed in

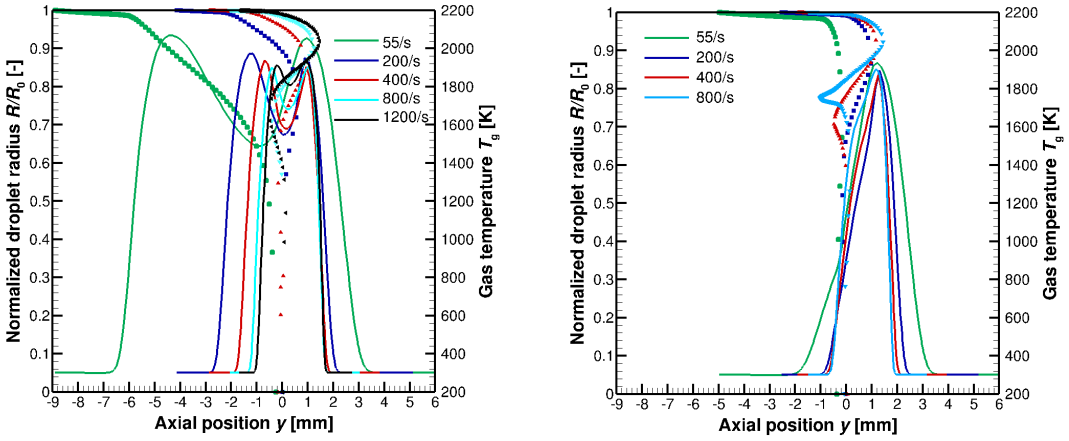

(a) Two chemical reaction zones

(b) Single chemical reaction zone

Figure 3.20: Gas temperature and normalized droplet radius for initial strain rates from 55/s to 1200/s and $R_0 = 30$ µm and $E_{-\infty} = 1.5$ [28].

the minimum gas temperature situated between the two peaks in the double chemical reaction zone. It can be concluded that an increase in equivalence ratio predominantly affects this minimum temperature and the associated vaporization dynamics in the double flame structure, as well as the disappearance of the shoulder on the left side of the gas temperature profile in the single flame structure.

Figs. 3.19 and 3.20 display the temperature profiles for droplet sizes of 50 µm and 30 µm, respectively, at an equivalence ratio of 1.5 and a strain rate of 55/s. These figures illustrate that the effects of strain and initial droplet size are more pronounced compared to those of the equivalence ratio. Within these profiles, a progressive increase in the initial strain rate leads to a narrowing of the reaction zone for both the single and double reaction zone structures. At lower strain rates, the spray is able to penetrate deeper into the flame front, with droplets occasionally crossing the flame front and oscillating around the stagnation plane as the strain rate increases. This re-entry of droplets into the flame zone significantly enhances both evaporation and combustion, particularly before flame extinction events, thus critically influencing both flame temperature and stability. These observations underscore the complex interaction between droplet dynamics, chemical reactions, and flame structure in spray combustion. The understanding of these dynamics is crucial for optimizing combustion processes in practical applications, especially in designing systems that must operate over a range of conditions involving variations in fuel characteristics and operational parameters.

Exploring the transition from double to a unique structure of laminar spray flames involves analyzing the geometric characteristics of the reaction and evaporation zones across different initial strain rates, as detailed in Fig. 3.21. Figure 3.21a depicts these characteristics for a droplet size of $r_0 = 50$ µm, and Fig. 3.21b presents them for $r_0 = 30$ µm, both at

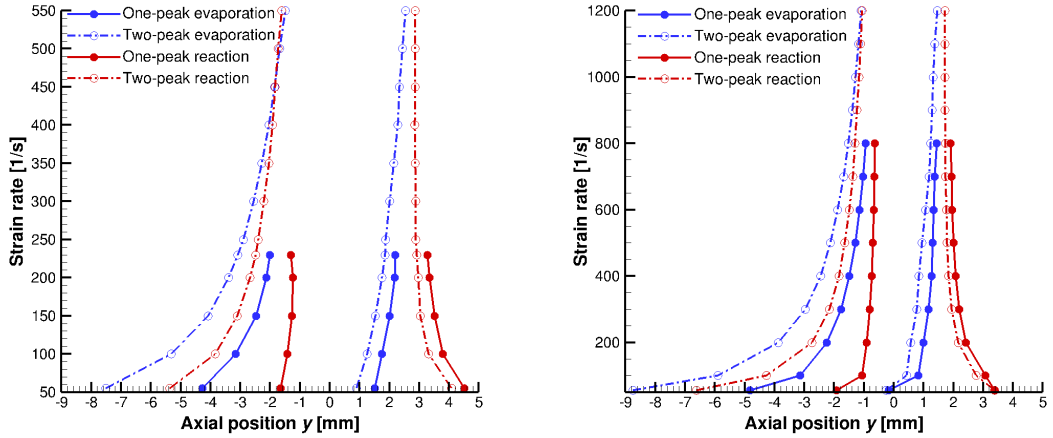

(a) $R_0 = 50\,\mu\text{m}$ (b) $R_0 = 30\,\mu\text{m}$

Figure 3.21: Left and right boundaries of evaporation and chemical reaction zones for the structures with one (solid lines) and two (dashed lines) reaction zones for $E_{-\infty} = 1.5$, $T_{l,0} = T_{g,0} = 300$ K [28].

a fixed equivalence ratio of 1.5 and variable gas strain rates.

The boundary of the vaporization regimes is identified by a normalized droplet radius of 0.999, while the boundary for the chemical reaction zone is marked by a gas temperature above 310 K. It's noted that the chemical reaction zone in the one-peak structure tends to be shifted toward the air side compared to the two-reaction zone structure, and these zones converge as the strain rates increase. On the spray side, the difference in the positioning of the zones is significant. The evaporation zone is substantially broader than the chemical reaction zone. On the air side, the vaporization zone generally lies within the chemical reaction zone, whereas on the spray side, the opposite holds true.

In the two-peak structure, flame extinction tends to occur when the widths of the evaporation and chemical reaction zones become similar. At this point, the droplets are positioned outside the chemical reaction zone, preventing sustained evaporation. The initial choice of 310 K to identify the chemical reaction zone may be inadequate. A higher threshold, such as around 700 K, might more accurately reflect the conditions under which droplets exit the combustion zone, as evaporation ceases to occur effectively, exemplified in Fig. 3.6 for the two-reaction zone structure and Fig. 3.3 for the single flame structure. Notably, in the two-reaction zone structure, droplets exit the chemical reaction zone towards the air side, whereas in the single flame structure, they exit towards the spray side.

This qualitative difference in behavior between the different spray flame structures suggests underlying variations in the dynamics of chemical reactions and physical transport processes. To further understand the mechanism behind the transition in flame structures, it would be beneficial to examine the chemical timescales of the system. These can be evalu-

ated by considering the molar reaction rate $\dot{\omega}_k$ and the concentration of species k.

$$t_k = \frac{c_k}{|\dot{\omega}_k|}, \; i = 1, \ldots, K. \tag{3.1}$$

To further investigate the dynamics of spray flame structures, the variation in chemical reaction times across the counterflow configuration is crucial. As illustrated in Fig. 3.22, these timescales differ for each chemical species, illustrating the complex interplay of reactions within the flame. Additionally, the evaporation timescale, denoted as t_{evap}, plays a significant role in influencing flame behavior and is calculated using the following formula:

$$t_{\text{evap}} = \frac{m_i}{\dot{m}_i}, \tag{3.2}$$

where m_i is the mass of a droplet and $\dot{m}_i$ denotes its mass evaporation rate. The index i depends on the number of droplet reversals and stands for the droplet size group in case polydispersity occurs due to droplet oscillations. The vaporization timescales are always larger than those of chemical timescales inside the vaporization zone as can be seen in Fig. 3.22 for a strain rate of 230/s, $R_0 = 50$ µm, and $E_{-\infty} = 1.5$ which is just prior to the breakdown of the structure with a single chemical reaction zone, cf. Figs. 3.3 and 3.4.

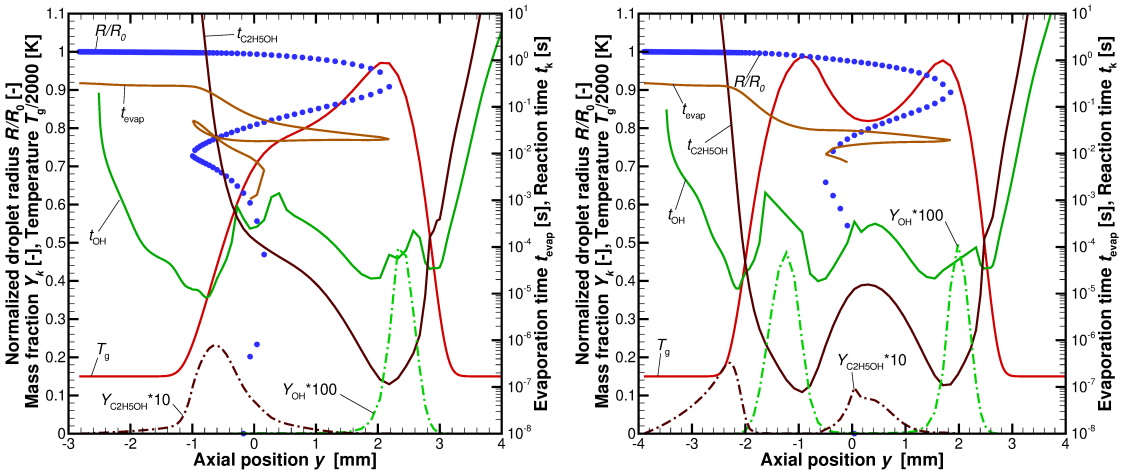

(a) Single reaction zone

(b) Two reaction zones

Figure 3.22: Timescales of evaporation, t_{evap} and of chemical reactions, t_k, for $R_0 = 50$ µm, $E_{-\infty} = 1.5$, and $a_{-\infty}$ = 230/s, $T_{\text{l},0} = T_{\text{g},0}$ = 300 K [28].

A critical examination of the chemical timescales, particularly comparing those of the fuel vapor C_2H_5OH with OH, reveals that initially, after liquid fuel evaporation, the chemical timescale of C_2H_5OH is considerably longer than that of OH. However, following substantial spray evaporation, the chemical timescale of OH lengthens, and at $y = -0.3$ mm, the timescales of both species converge. At this juncture, the gas temperature approximates the crossover temperature T_{cross} of 1104 K, where the rates of the propagating reaction H + O_2

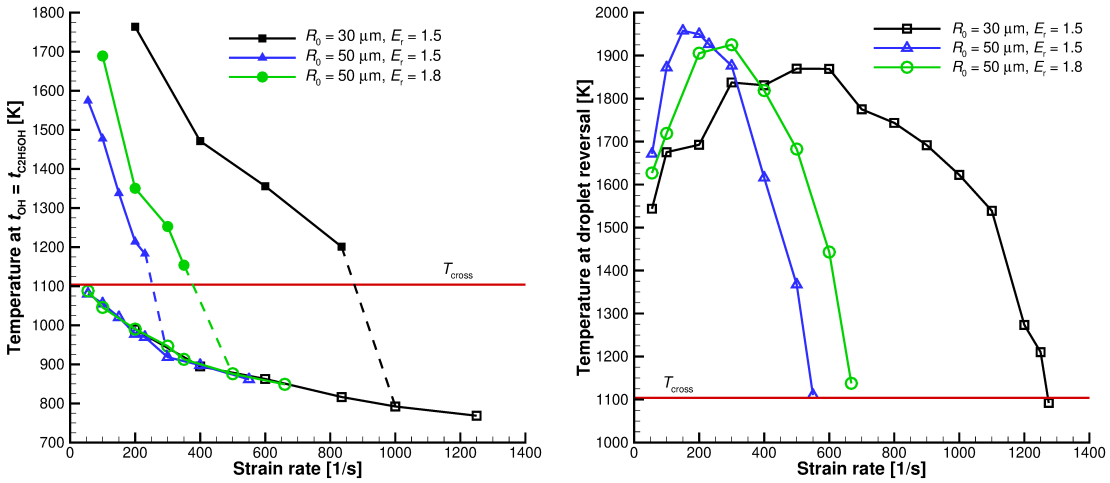

(a) Temperature at which $t_{OH} = t_{C_2H_5OH}$ (b) Temperature at the first droplet reversal point

Figure 3.23: Gas temperature versus gas strain rate for various conditions in the single flame structure (filled symbols) and the double flame structure (open symbols) (a) evaluated at equal reaction times of C_2H_5OH and OH on the spray side of the configuration. (b) evaluated at the first reversal point of the droplets on the gas side of the configuration in the double-peak flame structure [28].

$\rightleftharpoons$ OH + O and the termination reaction H + O_2 + M $\rightarrow$ HO_2 + M are balanced. Figure 3.23a illustrates the gas temperature at which these chemical timescales equilibrate for both the single reaction zone (filled symbols) and the dual reaction zone structures (open symbols). It is observed that if the point at which OH's timescale exceeds that of the fuel vapor is below the crossover temperature, the single flame structure transitions to a double flame structure as the strain rate increases. This transition is marked by dashed lines in Fig. 3.23a.

Additionally, Figure 3.23b analyzes the relationship between gas temperature and gas strain rate at the location of the first droplet reversal on the gas side of the counterflow configuration for the dual reaction zone structure; at these higher strain rates, the single reaction zone structure is not sustainable. Under all evaluated conditions, gas temperature initially increases with strain rate but subsequently decreases, leading to a breakdown of the spray flame structure when the crossover temperature is reached, thereby disrupting the chain branching reaction. Consequently, both chemical processes and vaporization dynamics play pivotal roles in the limits of spray flame sustainability beyond certain strain rate thresholds, as evidenced by the significant peak in mass evaporation rate at this position at the highest gas strain rate of 550/s, shown in Fig. 3.6b.

The next subsection will emphasize the complex interaction between chemical kinetics and physical evaporation processes in determining the stability and transition of flame structures in ethanol spray combustion within a counterflow configuration.

3.1.2 Triple Flame Structures

Building on previous research discussed in the last subsection, this study further examines the structures of laminar non-premixed ethanol/air spray flames in a counterflow configuration under fuel-rich conditions, employing numerical simulations. The setup utilizes a monodisperse ethanol spray propelled by air, which encounters a counter air stream in an axisymmetric arrangement. Both streams are introduced at 300 K under atmospheric pressure. This analysis identifies up to three distinct flame structures for identical boundary and initial conditions at low gas strain rates and small droplet sizes. Regime diagrams are generated to describe the conditions under which these structures display, focusing on the gas strain rate on the spray side of the configuration, $a_{-\infty}$, starting from 55/s with an initial spray velocity of 0.44 m/s. The equivalence ratio on the spray side, $E_{-\infty}$ is varied from 1.1 to 1.6, and initial droplet radii R_0 range from 10 µm to 50 µm. The analysis reveals that the most stable spray flame structure is characterized by two chemical reaction zones, one located on the spray side and the other on the gas side of the configuration. In certain conditions, single chemical reaction zones on either side of the configuration are also observed. This study outlines the conditions under which these diverse flame structures can exist, expanding on previous findings that identified only two coexisting structures under slightly different boundary conditions, by presenting three distinct structures for the first time. Additionally, mechanisms of transition between these structures are analyzed. The interaction between energy-intensive spray evaporation and the heat released by exothermic chemical reactions, coupled with the positioning of the spray, critically influences the existence or absence of the different flame structures. This dynamic may also explain specific characteristics of spray flames, such as flame pulsation, by providing insight into the fluid dynamics and chemical kinetics underlying these phenomena. The following discussion examines the first identification of the third spray flame structure different from those discussed in Subsection 3.1.1, followed by a detailed examination of these diverse triple flame structures. The discussion will explore how the initial droplet size, equivalence ratio, and gas strain rate influence the existence and stability of each flame configuration.

Identification of the Third Spray Flame Structure

The identification of a third spray flame structure was achieved under specific conditions, revealing the coexistence of three distinct spray flame structures. Following a detailed analysis of various coexisting spray flame structures under the condition of $R_0 = 15\,\mu\text{m}$, an equivalence ratio of 1.5, and a gas strain rate increasing from 55/s, the identification of a third spray flame structure was accomplished. This discovery, in conjunction with the previously identified double flame structures discussed in Subection 3.1.1, confirms the co-

existence of three distinct spray flame structures.

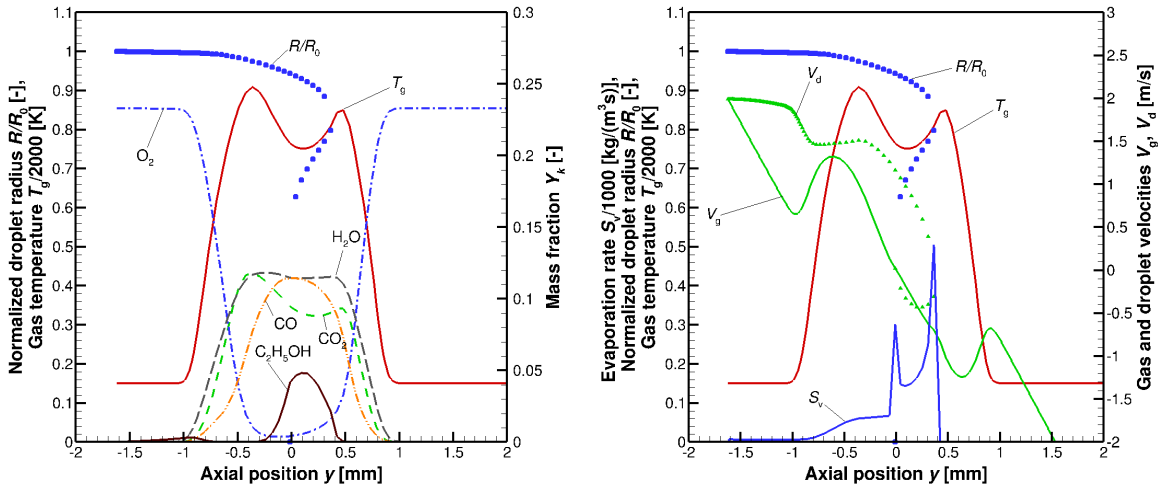

Figure 3.24: Spray flame structure with two reaction zones for $R_0 = 15\,\mu\text{m}$, $E_{-\infty} = 1.5$, $T_{l,0} = T_{g,0} = 300$ K, $a_{-\infty} = 1120$/s. Left: Outer flame structure; Right: Spray characteristics [58].

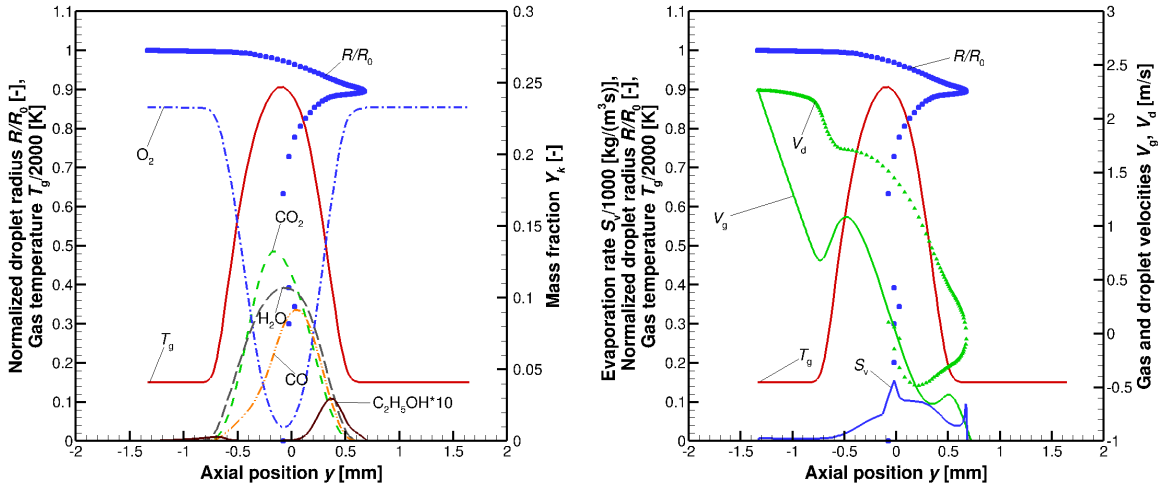

Figure 3.25: Spray flame structure with one reaction zone on the spray side for $R_0 = 15\,\mu\text{m}$, $E_{-\infty} = 1.5$, $T_{l,0} = T_{g,0} = 300$ K, $a_{-\infty} = 1450$/s. Left: Outer flame structure; Right: Spray characteristics [58].

Figures 3.24 show the flame structures with two chemical reaction zones of the configuration at 1120/s. Beyond a gas strain rate of 1120/s, only the spray flame structure with a single chemical reaction zone on the spray side of the counterflow configuration exists, see Fig. 3.25 for $a_{-\infty} = 1450$/s. Even though the qualitative results for the gas strain rates of 1120/s and 1450/s are similar, the right peak in the profile of the spray vaporization rate decreases and leaves the chemical reaction zone [28], leading to the non-existence beyond a gas strain rate of 1450/s. It is notable that the breakdown of this spray flame structure is not

due to chemical extinction which prevails in gas combustion [32] but due to a breakdown of vaporization [28, 137].

After applying the rules from Subsection 2.2.6, triple flame structures were observed at low gas strain rates and small droplet sizes of $R_0 = 15$ µm. Figure 3.26 shows the range of existence of single, two, or three different flame structures for the same initial and boundary conditions where both the initial droplet radius and the gas strain rates on the spray side of the configuration are modified for a fixed equivalence ratio of 1.5. The blue triangles display structures with a single reaction zone on the spray side of the configuration, the red triangles display spray flames with a single reaction zone on the gas side of the configuration, and the circle shows conditions for which structures with two reaction zones exist where one resides on the spray side and the other one on the gas side of the counterflow configuration. These findings were then extended to other droplet radii and they will be detailly discussed in following discussion.

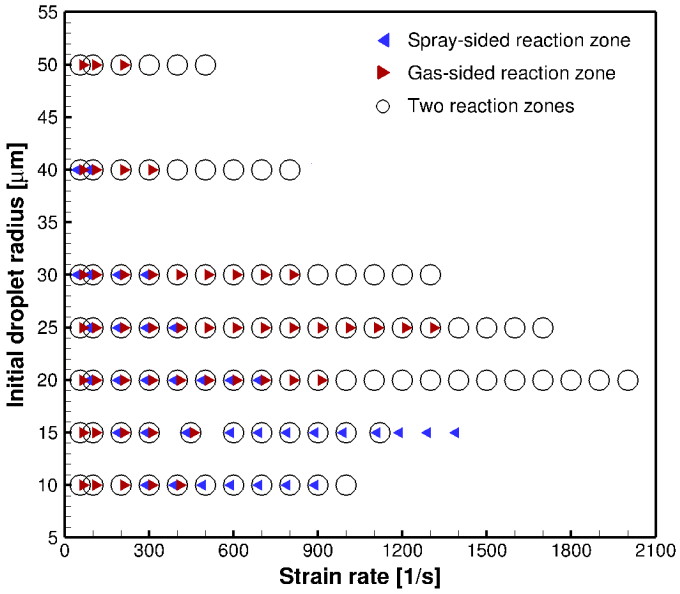

Figure 3.26: Regime diagrams of spray flame structures with single spray- or gas-sided reaction zones or two reaction zones for $E_{-\infty} = 1.5$, depending on the gas strain rate and initial droplet radius [58].

Characteristics of the Triple Spray Flame Structures

A series of numerical simulations were conducted on a monodisperse ethanol spray accompanied by carrier gas air, directed against an opposing air stream under atmospheric pressure. Initial temperatures for both gas and spray are set at 300 K, with an equivalence ratio ($E_{-\infty}$) on the spray side ranging from 1.1 to 1.6. The study focuses on the structures of fuel-rich spray flames, considering initial droplet radii from 10 µm to 50 µm, and an initial spray ve-

locity ($v_{g,-\infty} = v_{d,-\infty} = 0.44$ m/s) at a spray-sided gas strain rate of 55/s. This is followed by a comprehensive examination of the flame structures, delving into the effects of initial droplet radii, equivalence ratios, and gas strain rates. Identifying a specific operational condition where three distinct spray flame structures coexist, a detailed analysis and discussion of their characteristics is conducted. The presence of these diverse structures is confirmed for an initial droplet radius of $R_0 = 10\,\mu$m, an equivalence ratio of $E_{-\infty} = 1.2$, and a gas strain rate on the spray side of the counterflow configuration of $a_{-\infty} = 400$/s.

The specific flame structures under these conditions are visualized in Fig. 3.27. This scenario provides a unique opportunity to examine the spray flame dynamics, particularly how the small initial droplet size combines with moderate equivalence ratio and high strain rate to support the existence of distinct flame structures. The analysis will focus on the individual and collective behaviors of these structures, exploring how they contribute to overall flame stability and performance under these specified conditions. This discussion aims to deepen the understanding of flame structure dynamics in spray combustion processes, providing insights into their potential applications and implications in real-world scenarios.

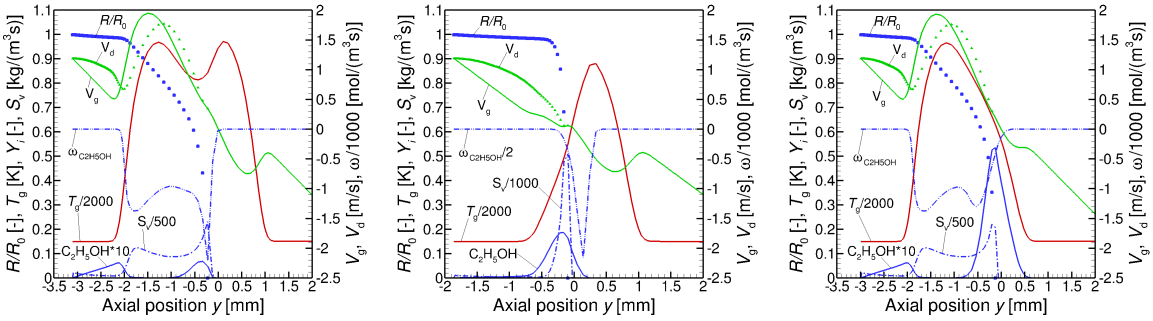

(a) Two reaction zones (b) Gas-sided reaction zone (c) Spray-sided reaction zone

Figure 3.27: Different flame structures for $R_0 = 10\,\mu$m, $E_{-\infty}$ = 1.2, $T_{l,0} = T_{g,0}$ = 300 K, $a_{-\infty}$ = 400/s: Normalized droplet radius R/R_0, gas temperature T_g, mass fraction of fuel vapor $Y_{C_2H_5OH}$, mass evaporation rate S_v, and gas and droplet velocities, v_g and v_d [29].

The monodisperse spray flame structures with a relatively small initial droplet radius of 10 µm demonstrate a vaporization zone that is entirely confined to the spray side of the configuration. The droplets do not reach the stagnation plane located at the axial position of $y = 0$ mm. This distribution is evidenced in the profile of the source term in the continuity equation, which spans from approximately -2 mm to -0.2 mm, encompassing the zone where droplet evaporation occurs.

The gas temperature profile features a notable dip just before the stagnation plane where a peak in the profile of S_v is observed. This peak corresponds to the location where all droplets eventually evaporate, inducing significant energy consumption due to spray evaporation. The profile of the fuel vapor correlates with that of S_v, reflecting the consumption of fuel in the hot regions of the flame. This is further confirmed by the molar chemical reaction

rate $\dot{\omega}_{C_2H_5OH}$, which shows negative peaks around -1.8 mm and -0.2 mm, where most of the fuel vapor is generated through vaporization.

Both gas and droplet velocities, v_g and v_d, which are equal at the spray boundary, illustrate the significant impact of drag force on the droplets. As droplets evaporate and dwindle in size, their velocities tend to converge with that of the gas.

Additional spray flame structures with single chemical reaction zones are also identified. In Fig. 3.27b, the reaction zone is located on the spray side of the configuration, whereas in Fig. 3.27c, it is situated on the gas side. The primary spray flame structure presented in Fig. 3.27b was previously identified in Subsection 3.1.1 for a gas strain rate of $a_{-\infty} = 55/s$, where the third structure shown in Fig. 3.27c does not manifest at this lower strain rate and with an initial droplet radius of 50 µm at an equivalence ratio of $E_{-\infty} = 1.5$.

A comparative analysis of the spray flame structures displayed in Figs. 3.27a and 3.27c reveals that the spray-sided structure in Fig. 3.27a closely resembles that in Fig. 3.27c. Conversely, the structure presented in Fig. 3.27b is qualitatively different. Gutheil [136] previously identified two distinct spray flame structures for methanol/air sprays, exhibiting either two chemical reaction zones or a single zone on the spray side of the configuration. It was argued that the spray-sided chemical reaction zones are similar or even identical to scenarios where the gas-sided reaction zone is extinguished in configurations with a single chemical reaction zone on the spray side, an observation that holds true in the current analysis as well. However, the structure exhibited in Fig. 3.27b introduces a qualitatively different configuration with distinctly separated vaporization and chemical reaction zones. This structure, as discussed in Subsection 3.1.1, emphasizes the unique behavior of such configurations under specific operational conditions. Importantly, this study is the first to demonstrate the existence of three distinct spray flame structures under identical initial and boundary conditions for fuel-rich spray flames in a counterflow configuration, thus expanding the understanding of the dynamic behavior of spray flames and their stability under varied conditions.

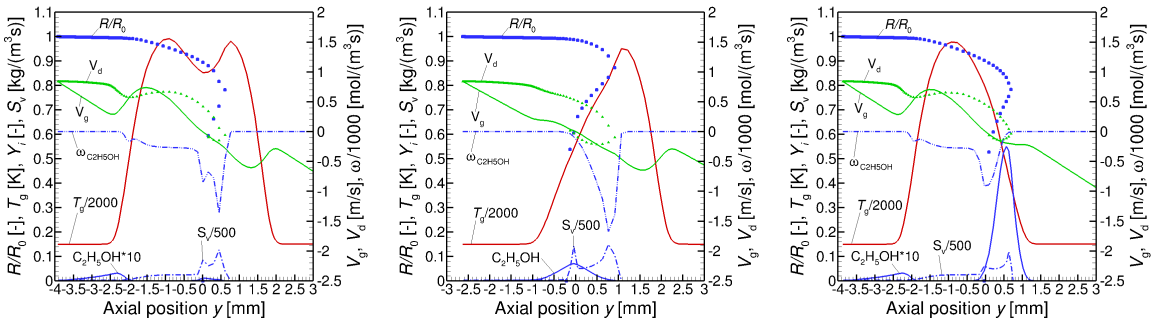

(a) Two reaction zones (b) Gas-sided reaction zone (c) Spray-sided reaction zone

Figure 3.28: Different flame structures for $R_0 = 30$ µm, $E_{-\infty} = 1.2$, $T_{l,0} = T_{g,0} = 300$ K, $a_{-\infty} = 200/s$: Normalized droplet radius R/R_0, gas temperature T_g, mass fraction of fuel vapor $Y_{C_2H_5OH}$, mass evaporation rate S_v, and gas and droplet velocities, v_g and v_d [29].

The existence of diverse spray flame structures has important implications for phenomena such as spray flame pulsation, as identified in the literature [173]. Particularly, the spray flame structure illustrated in Fig. 3.27b presents a noteworthy scenario in the context of micro-explosions of droplets. Such micro-explosions may occur in multicomponent droplets that exist in a relatively hot environment outside the main combustion zone, providing optimal conditions for puffing and micro-explosions [108].

In Fig. 3.27, small droplets are shown to evaporate entirely on the spray side of the counterflow configuration. However, as the initial droplet radius increases to 30 µm, notable changes in flame structure occur, with droplets crossing the stagnation plane and reversing, as shown in Fig. 3.28. The conditions in Figs. 3.27 and 3.28 are differentiated only by the initial droplet size and the gas strain rate at the spray boundary, set at 400/s and 200/s respectively.

Figure 3.28 showcases the three corresponding structures to those in Fig. 3.27 but for the larger initial droplet radius and reduced gas strain rate. A significant difference is the deep penetration of the larger droplets into the configuration, where they cross the stagnation plane and reverse due to the opposing airflow, leading to a locally polydisperse spray. This alteration is reflected in the profiles of droplet velocities. Enhanced evaporation at the droplet reversal positions, due to prolonged residence times, is evident in the profile of S_{v}.

Despite the changes, the principal characteristics of the three different spray flame structures are preserved for larger initial droplet radii. The spray flames broaden, and the evaporation zone expands. In the configuration with two chemical reaction zones, as seen in Fig. 3.28a, the location of droplet reversal resides inside the chemical reaction zone. Conversely, in scenarios with a single chemical reaction zone, as illustrated in Figs. 3.28b and 3.28c, the droplet reversal does not occur inside but closer to the respective sides of the configuration. Additionally, it is observed that in the structure with a single chemical reaction zone on the spray side, droplets exit the chemical reaction zone due to their larger momentum. At higher initial droplet radii, not only does droplet reversal occur, but also oscillation, and under such conditions, triple flame structures are not observed.

The subsequent subsection will analyze the conditions facilitating the existence of multiple spray flame structures. This integration of findings across diverse scenarios and parameter variations aims to explain the factors that influence flame structure within spray combustion systems, providing a comprehensive analysis integral to this study.

Regime Diagrams and Transition Mechanisms in Triple Spray Flame Structures

Serial numerical simulations were performed to explore the behavior of laminar non-premixed ethanol/air spray flames under varied conditions within a counterflow configuration. These simulations systematically varied key parameters including the equivalence ratio ($E_{-\infty}$) on

the spray side, which ranged from 1.1 to 1.6, indicating fuel-rich conditions. Initial droplet radii were also varied, spanning from 10 µm to 50 µm, to assess the impact of droplet size on flame characteristics. Additionally, gas strain rates were incrementally increased up to a critical point beyond which no stable numerical solutions could be obtained. The analysis begins with the presentation of regime diagrams that categorize the conditions under which single or multiple spray flame structures can exist, followed by the discussions on mechanisms behind the transition and eventual breakdown of these spray flame structures, providing a deeper understanding of the dynamic interactions between physical spray characteristics and combustion chemistry within this configuration.

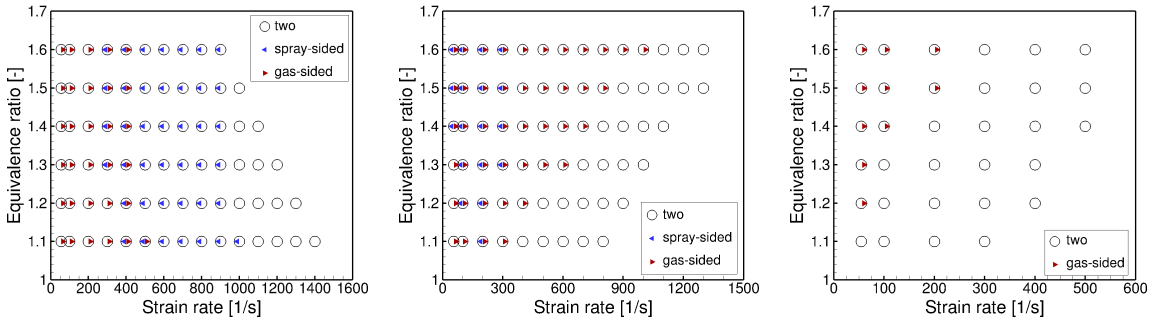

(a) $R_0 = 10$ µm (b) $R_0 = 30$ µm (c) $R_0 = 50$ µm

Figure 3.29: Regime diagrams of spray flame structures with single spray- or gas-sided reaction zones or two reaction zones for different initial droplet radii R_0, depending on the gas strain rate and the equivalence ratio on the spray side of the configuration [29].

Diagrams illustrating the existence of multiple spray flame structures under consistent initial and boundary conditions for initial droplet radii of 10 µm, 30 µm, and 50 µm are depicted in Figs. 3.29a through 3.29c. Note that Fig. 3.29b is an updated regime diagram of Fig. 3.17b, incorporating the newly identified third flame structure.

Figure 3.29 employs symbols to represent the presence of spray flames as a function of equivalence ratios ($E_{-\infty}$) ranging from 1.1 to 1.6, indicative of fuel-rich conditions, and gas strain rates ($a_{-\infty}$) on the spray side of the configuration, for varying initial droplet sizes of the monodisperse sprays. In this figure, blue and red triangles denote structures with a single chemical reaction zone situated on the spray and gas sides of the configuration, respectively. Black circles represent conditions under which structures with two chemical reaction zones are observed, with one zone on each side of the counterflow configuration. Specifically, triangles pointing left (blue) and right (red) signify the existence of a spray flame structure with a single chemical reaction zone on the spray or gas side, respectively. Black circles denote a structure with two chemical reaction zones positioned on either side of the configuration. These regime diagrams serve as a visual summary of the range and type of flame structures possible under varying operational conditions. Areas without symbols indicate the absence of spray flame structures under those specific conditions.

Regime diagrams in Figs. 3.29a and 3.29b for initial droplet radii of 10 μm and 30 μm, respectively, show that the three distinct spray flame structures persist at lower strain rates but cease to exist at very high strain rates. With increased gas strain rates, larger initial droplet sizes tend to favor a single chemical reaction zone on the gas side of the configuration, while smaller initial droplet sizes prefer a spray-sided single chemical reaction zone due to differences in droplet behavior and evaporation characteristics. The implications of these observations and their relevance to spray combustion dynamics are further discussed in subsequent sections of the text. This analysis helps to clarify the conditions under which different flame structures can be sustained or fail to form, providing essential insights into the complex interplay between droplet size, chemical kinetics, and flow dynamics in spray flames.

The analysis of the flame structures represented in Fig. 3.29 indicates that configurations with two chemical reaction zones demonstrate greater stability, persisting at higher strain rates compared to those with single chemical reaction zones. Furthermore, the range of strain rates that allow for viable numerical solutions decreases with an increase in the initial droplet radius. For configurations where multiple structures are feasible, the presence of a single chemical reaction zone on the gas side is more commonly associated with larger initial droplet sizes. Conversely, spray flames with a single chemical reaction zone on the spray side predominantly occur with the smallest initial droplet radius of 10 μm. Structures featuring three chemical reaction zones are observed only for smaller initial droplet sizes and at moderate strain rates.

The following discussion explores scenarios leading to the breakdown of various spray flame structures. Triple flame structures are not observed with initial droplet radii of 50 μm or at extreme equivalence ratios for smaller initial droplet sizes, as illustrated in Fig. 3.29. Adjusting the gas strain rate from the 200/s condition detailed in Fig. 3.28 results in the loss of one of the triple flame structures, leaving only two distinct spray flame structures. At an initial droplet radius of 30 μm, the flame structure with the gas-sided reaction zone remains consistent across variations. For an initial droplet radius of 10 μm, reducing $a_{-\infty}$ preserves the flame structure with the gas-sided reaction zone, whereas at higher strain rates, the structure with the spray-sided reaction zone predominates. In each scenario, structures featuring two chemical reaction zones are maintained. The underlying reasons for these phenomena will be explored in the following discussion.

Increasing the gas strain rate from 200/s to 400/s at an initial droplet radius (R_0) of 30 μm leads to the breakdown of the flame structure with a single reaction zone on the spray side of the configuration. This breakdown occurs as the peak gas temperature falls below approximately 1700 K, a threshold below which flame extinction is observed, as reported in 3.1.1. At these conditions, Figs. 3.30a and 3.30b illustrate the remaining spray flame

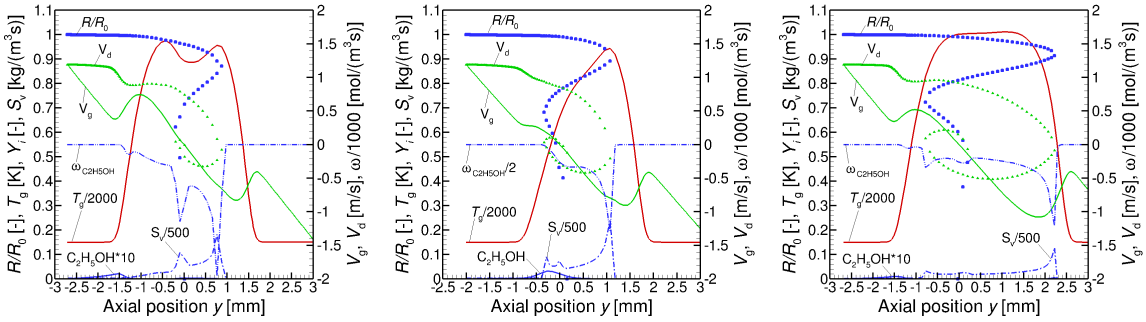

(a) Two reaction zones (b) Gas-sided reaction zone (c) Two reaction zones

Figure 3.30: Flame structures at $E_{-\infty}$ = 1.2, $T_{l,0} = T_{g,0}$ = 300 K, $a_{-\infty}$ = 400/s. (a-b) for $R_0 = 30$ µm (c) for $R_0 = 50$ µm [29].

structures at $R_0 = 30$ µm, equivalence ratio ($E_{-\infty}$) of 1.2, and a gas strain rate ($a_{-\infty}$) of 400/s. The spray flame structure previously shown in Fig. 3.28c transitions into a structure with two chemical reaction zones due to the strong vaporization on the spray side occurring in a significantly hot environment, allowing the development of a second chemical reaction zone as indicated in Fig. 3.30a.

At a larger initial droplet radius of 50 µm, only two distinct spray flame structures are observed, as seen in Fig. 3.29c. An increase in gas strain rate from 55/s to 100/s at $E_{-\infty} = 1.2$ results in a uniform spray flame structure featuring two chemical reaction zones, as demonstrated in Fig. 3.30c. The disappearance of the single spray flame structure correlates with the development of a temperature shoulder on the spray side of the configuration, which evolves into a separate chemical reaction zone 3.1.1, leading to the dominance of structures with two chemical reaction zones in the regional diagram for $R_0 = 50$ µm as displayed in Fig. 3.29c.

The transition to fewer and ultimately to a singular spray flame structure is induced by the increased momentum of larger droplets, which causes droplet reversal and potential oscillation around the stagnation plane. This dynamic facilitates deeper penetration of the droplets into the chemical reaction zone and towards the gas side of the configuration, thereby enhancing the combustion process by feeding the flame with additional fuel vapor. This interaction illustrates the critical relationship between vaporization and combustion within spray flames: vaporization not only demands energy from the combustion zone but also supplies fuel vapor to it, while the chemical reactions consume this vapor and generate the necessary energy for further vaporization. Moreover, the motion and positioning of droplets within the counterflow configuration are pivotal in determining the spatial distribution of vaporization and combustion zones. The behavior of droplets, and hence the structure and stability of the spray flames, vary significantly depending on the initial droplet radius in monodisperse sprays. This variation underscores the complex interaction between physical

spray properties and combustion dynamics, which governs the transition among different spray flame structures.

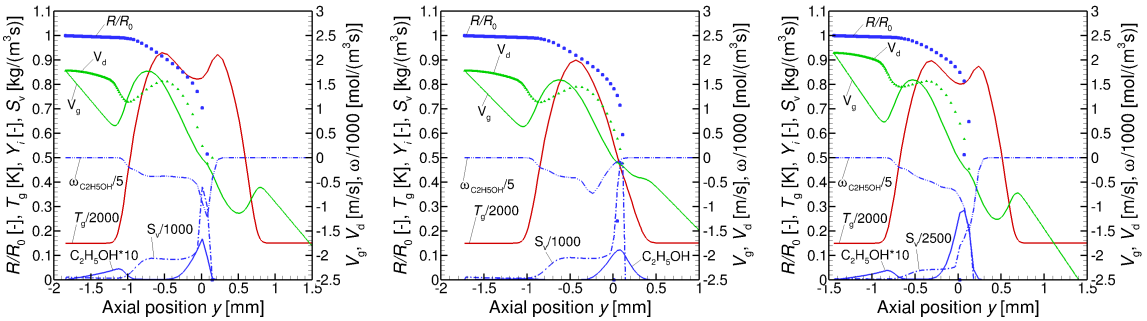

(a) Two reaction zones (b) Spray-sided reaction zone (c) Two reaction zones

Figure 3.31: Flame structures at $E_{-\infty}$ = 1.2, $T_{l,0} = T_{g,0}$ = 300 K, $R_0 = 10$ µm. (a-b) $a_{-\infty}$ = 900/s (c) $a_{-\infty}$ = 1300/s [29].

The transition mechanism from three to two different spray flame structures at an initial droplet radius (R_0) of 10 µm is analyzed within the context of Fig. 3.31. Figures 3.31a and 3.31b illustrate the two remaining structures at a strain rate of 900/s, with the structure featuring the gas-sided chemical reaction zone no longer present. As the strain rate increases, chemical reaction times decline, leading to chemical extinction. A comparison of the maximum gas temperatures across different spray flame structures at 400/s, under fixed conditions shown in Fig. 3.27, indicates the lowest temperature occurs in the gas-sided chemical reaction zone, highlighting its instability. Further increasing the gas strain rate to 1300/s results in the collapse of the second spray flame structure, leaving only the structure with two chemical reaction zones, as represented in Fig. 3.31c. This breakdown mirrors the dynamics discussed previously for higher strain rates. An additional increase in strain rate further narrows the spray flame and significantly reduces the peak gas temperature, preventing sustainable chemical reactions, and thereby excluding the existence of spray flames beyond 1300/s.

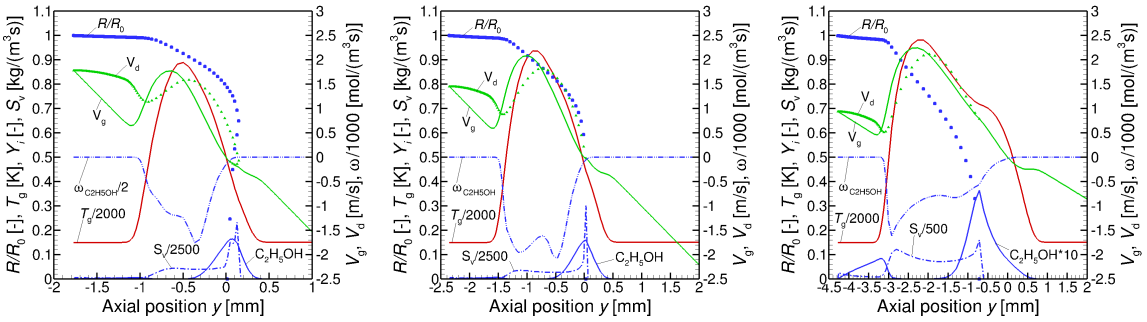

(a) $a_{-\infty}$ = 900/s (b) $a_{-\infty}$ = 600/s (c) $a_{-\infty}$ = 250/s

Figure 3.32: Spray-sided flame structures at $T_{l,0} = T_{g,0}$ = 300 K, $E_{-\infty}$ = 1.5, $R_0 = 10$ µm for different gas strain rates [29].

Figure 3.32 illustrates the loss of the spray-sided flame structure at an equivalence ratio $E_{-\infty} = 1.5$ and initial droplet radius $R_0 = 10$ μm, as gas strain rates are reduced from 900/s to 600/s and further to 250/s. To enhance the visibility of physical processes, the equivalence ratio is adjusted from 1.2 to 1.5. With the decrease in strain rate, the chemical reaction zone broadens while the vaporization zone narrows, eventually merging completely into the chemical reaction zone at the lowest strain rate, as illustrated in the sequence of subfigures. Additionally, the axial position range is varied in Fig. 3.32 to improve the resolution of results. At the lowest strain rate, a temperature shoulder develops on the gas side, contributing to the formation of a second chemical reaction zone, transitioning the structure into one with two chemical reaction zones. For strain rates lower than 250/s, the displayed spray flame structure ceases to exist, transitioning into a configuration with two chemical reaction zones. This transition occurs as the energy-intensive vaporization zone shifts towards the spray side, allowing sufficient energy to establish the second chemical reaction zone on the gas side.

In summary, spray flame structures with two reaction zones are observed in all cases and demonstrate greater stability compared to those with a single chemical reaction zone. Triple flame structures are only present at low initial droplet radii and moderate gas strain rates. Structures with the largest initial droplet radius of 50 μm do not exhibit a spray-sided reaction zone, as the high momentum of the droplets facilitates their penetration and potential reversal within the chemical reaction zone, with predominant evaporation occurring on the gas side. The transition mechanisms for the loss or emergence of spray flame structures are influenced by the intricate interaction between energy-consuming vaporization, droplet positioning within the counterflow configuration, and exothermic chemical reactions. As reported in the study [56], further exploration is needed on the impact of multiple spray flame structures on spray flamelet modeling. While the spray-sided chemical reaction zones in the twopeak structure are nearly identical to those in the single spray-sided flame structure, the gas-sided chemical reaction zone exhibits distinct behavior compared to the other two flame structures. Moreover, the identification of a single flame with a gas-sided chemical reaction zone introduces a new element requiring special consideration. This study's novelty lies in its identification of triple spray flame structures under certain conditions within fuel-rich spray flames.

In the next section, the discussion expands to address the laminar spray flames of multicomponent systems, focusing on hydrous ethanol droplets. This analysis will be facilitated through the development of a comprehensive Eulerian-Lagrangian methodology designed to investigate multicomponent droplet spray flames.

3.2 Hydrous Ethanol Spray Flames

Hydrous ethanol, renowned for its extensive applications as a sustainable fuel, particularly in internal combustion engines, has received significant interest [73, 74]. Numerous experimental studies have assessed the performance and operational characteristics of engines utilizing hydrous ethanol [77, 78, 79, 80, 81, 82, 83, 84, 85]. Additionally, while numerical simulations on this topic are scarce, they provide valuable insights [86, 87, 88]. Despite these efforts, fundamental research into hydrous ethanol combustion is relatively undeveloped, often limited to specific areas such as laminar burning velocity [89, 90, 91, 92], ignition delay times [93], spray characteristics [87], and flame instability [94]. This specialization underscores an ongoing need for broader research into hydrous ethanol combustion, particularly concerning spray combustion processes, to enhance our understanding and optimize engine performance effectively.

This study numerically investigates laminar spray flames of hydrous ethanol, modeled as bicomponent ethanol/water droplets in a counterflow configuration. The investigation employs an extended Eulerian-Lagrangian methodology, as detailed in Subsection 2.2.4. The model accounts for variable physical properties of both the liquid and gas phases, along with detailed chemical reactions, as illustrated in Subsection 2.2.5. This section first presents the validation of an extended model, followed by an analysis of the typical structure of a hydrous ethanol spray flame. A comparative study of an anhydrous ethanol spray flame is conducted under identical conditions, with and without water addition to the initial droplet sprays, to investigate the impact of water content on flame structure. The term 'anhydrous ethanol' used for comparison here is the same as the 'ethanol' discussed in Section 3.1. Extinction strain rates for the hydrous ethanol spray flame are subsequently identified. Under specific conditions, multiple spray flame structures are observed in hydrous ethanol sprays. This study concludes with an analysis of the influence of water content on these multiple flame structures.

3.2.1 Validation of Extended Model

Numerical investigations of hydrous ethanol spray flames in a counterflow configuration were conducted using an extended version of the source code originally designed for monocomponent anhydrous ethanol spray flames within the same configuration, as documented in previous studies [26, 28, 29, 133, 158]. This extension, discussed in Subsection 2.2.4, adapts the model to accommodate bicomponent hydrous ethanol. Due to the absence of specific theoretical or experimental data for validating hydrous ethanol spray flames in this configuration, the bicomponent droplet vaporization model for convective heat transfer was validated

using numerical results [159] and experimental data [174] from single droplet studies. This validates the extended model's ability to accurately simulate hydrous ethanol sprays under specified conditions. The validation examines a single 600 µm bicomponent ethanol/water droplet as it undergoes heating and evaporation in convective dry air at atmospheric pressure. Initial ethanol mass fractions ranging from 0% to 100%, in increments of 25%, are tested, with the droplet initially at room temperature. The ambient air velocities considered vary from 2 m/s to 4 m/s, while gas temperatures are maintained at 400 K and 475 K. As

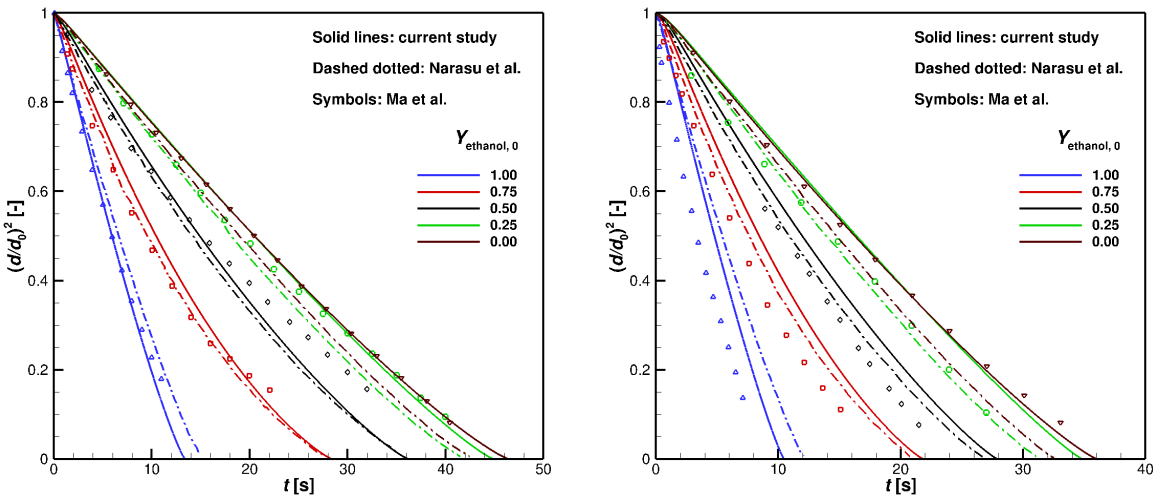

Figure 3.33: Normalized droplet surface area versus evaporation time for different initial conditions: $R_0 = 600\,\mu m$, $T_{l,0} = T_{g,0} = 293.15$ K, $p = 1$ bar, and (a) $u_0 = 4$ m/s, $T_{g,0} = 400$ K; (b) $u_0 = 2$ m/s, $T_{g,0} = 475$ K. Various initial mass fractions of ethanol range from 0% to 100%. The simulation results are validated against numerical data from Narasu et al. [159] and experimental data from Ma et al. [174].

demonstrated in Fig. 3.33, the numerical results for the bicomponent ethanol/water droplet's heating and evaporation in a convective environment closely match both previous numerical predictions [159] and experimental data [174]. This alignment builds on the success of the original code developed within an Eulerian-Lagrangian framework, which was rigorously validated for an n-heptane/oxygen flame [47] and subsequently adapted for ethanol/air spray flames [26, 28, 47, 133]. This extended code incorporates direct interactions between the gas and liquid phases via the source term in Eq. (2.59) and utilizes detailed thermophysical properties and chemical kinetics discussed in Subsection 2.2.5. These enhancements enable a comprehensive numerical study of hydrous ethanol spray flames in a counterflow configuration.

3.2.2 Typical Spray Flame Structures

The flame structures of monodisperse hydrous ethanol spray flames within a counterflow configuration were numerically investigated by using the validated model. To enhance un-

derstanding and provide context, the flame structures of pure ethanol (anhydrous ethanol)/air sprays are also examined, referencing previous research discussed in Section 3.1. These conditions relate to the cases studied in Subsection 3.1.2. The system is maintained at atmospheric pressure, with both the initial gas and spray temperatures set to 300 K. This study primarily focuses on the characteristics of spray flames initiated with a droplet radius of 30 μm and an equivalence ratio ($E_{-\infty}$) of 1.2. The gas strain rate ($a_{-\infty}$) on the spray side is progressively increased from an initial spray velocity of 0.44 m/s, starting at 55/s, to determine the maximum strain rate at which the spray flame remains sustainable, thereby identifying the extinction conditions of the spray flame. For hydrous ethanol cases, the equivalence ratio defined in Eq. 2.56 accounts only for the mass of ethanol.

Figure 3.34 depicts the gas characteristics of flame structures for both anhydrous and hydrous ethanol in a counterflow configuration. The left side of the figure presents anhydrous ethanol spray flames as a reference for comparing the combustion characteristics of hydrous ethanol sprays. In the hydrous ethanol spray, the initial water and ethanol volume fractions are 20% and 80%, respectively. This configuration is termed the ”hydrous ethanol spray flame” throughout this study unless otherwise specified for different water volume concentrations. The left subfigures of Fig. 3.34 highlight the features of anhydrous ethanol spray flame structures under a specific conditionof a gas strain rate ($a_{-\infty}$) of 200/s. This condition supports a stable flame structure featuring two chemical reaction zones, one on each side of the configuration, which has been demonstrated to be the most stable among triple flame structures, as discussed in Subsection 3.1.2. This setup serves as a benchmark for comparative analyses with hydrous ethanol spray flames under identical conditions and configurations as the anhydrous ethanol spray flame. The purpose is to investigate the effects of water addition on flame structure. The right subfigures of Fig. 3.34 depict the structure of a hydrous ethanol spray flame. As demonstrated in Fig. 3.34(a-b), the non-dimensional droplet radius (R/R_0) profiles are presented, along with the mass fraction profiles of typical species such as CO, CO_2, and H_2O. Additionally, their chemical reaction rates are illustrated in Fig. 3.34(c-d). The gas temperature (T_g) profiles are consistently shown across all subfigures in Fig. 3.34 to facilitate comparison.

In flame structures between droplets with and without water addition, there is a variation in gas temperature. In the anhydrous ethanol spray flame, the gas temperature profile values at the left peak, dip, and right peak positions are 1984.7 K, 1691.7 K, and 1961.8 K, respectively. Conversely, the hydrous ethanol flame shows lower temperatures at these positions: 1964.1 K, 1679.1 K, and 1941.2 K. This reduction is attributed to the ”thermal effect” of water vapor, which has a higher heat capacity [175]. The H_2O profile exhibits the most significant changes among all species in the hydrous ethanol spray flame. This is primarily due to the introduction of water into the spray, which significantly increases vapor

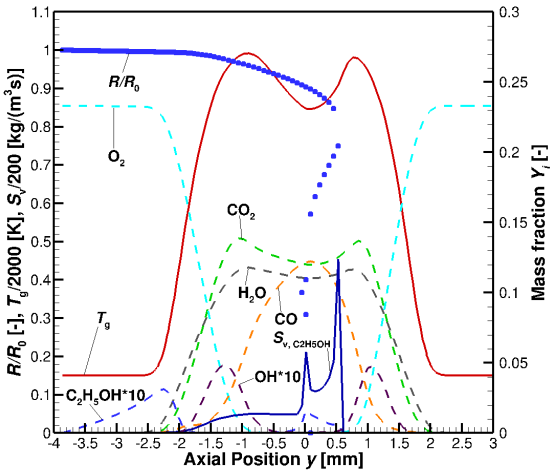

(a) Gas characteristics of anhydrous ethanol

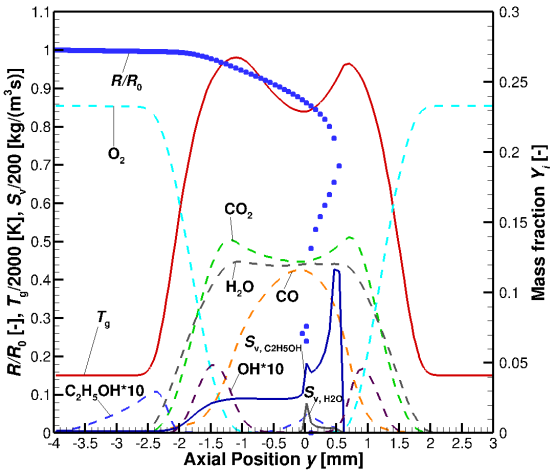

(b) Gas characteristics of hydrous ethanol

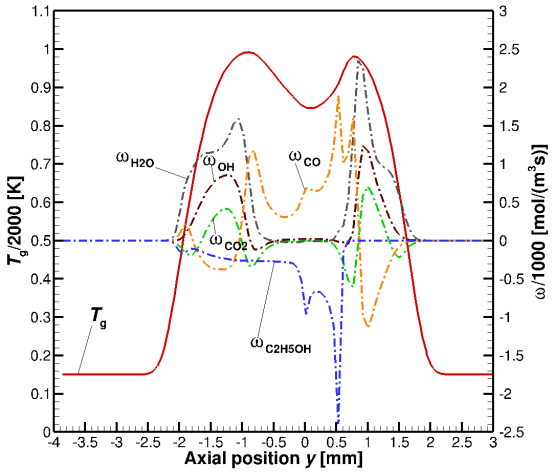

(c) Chemical reaction rates

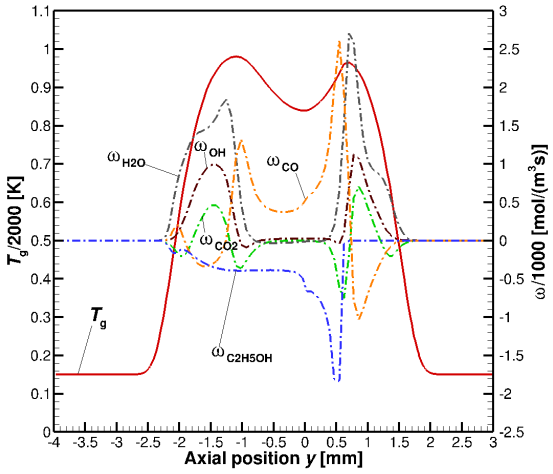

(d) Chemical reaction rates

Figure 3.34: Gas characteristics and chemical reaction rates of typical species of spray flame structures are presented under the condition: $R_0 = 30$ μm, $T_{l,0} = T_{g,0} = 300$ K, $E_{-\infty} = 1.2$, and $a_{-\infty} = 200$/s, for different sprays. Left: anhydrous ethanol; Right: hydrous ethanol.

production, as shown by the S_{v,H_2O} profile in Fig. 3.34(b), followed by diffusion influenced by the counterflowing effect. Notably, the mass fraction of gaseous H_2O between the two gas temperature peaks is higher in hydrous ethanol spray flames than in anhydrous ethanol flames. This difference is further reflected in the chemical reaction rate profiles of ω_{H_2O} in Figs. 3.34(c-d). In both flame types, the profiles of chemical reaction products generally mirror the gas temperature, displaying two local maxima. An exception is CO, which peaks in the cooler gas temperature region between the two chemical reaction zones. In a hydrous ethanol spray flame, the conversion of CO to CO_2 is enhanced, likely due to the chemical reaction $CO + OH \rightleftharpoons CO_2 + H$ [175]. Adding water to the droplet reduces the peak CO concentration by 4.98% and increases the CO_2 concentration by 1.72% at the same location. The chemical reaction rate profiles of ω_{CO}, as shown in Figs. 3.34(c-d), underscore the dis-

tinctions between anhydrous and hydrous ethanol spray flames. Specifically, the profiles of $\omega_{C_2H_5OH}$ in hydrous ethanol spray flames exhibit generally higher values compared to the anhydrous counterparts, with the exception at the 0 mm and 0.5 mm points where droplet reversal and oscillation occur, respectively.

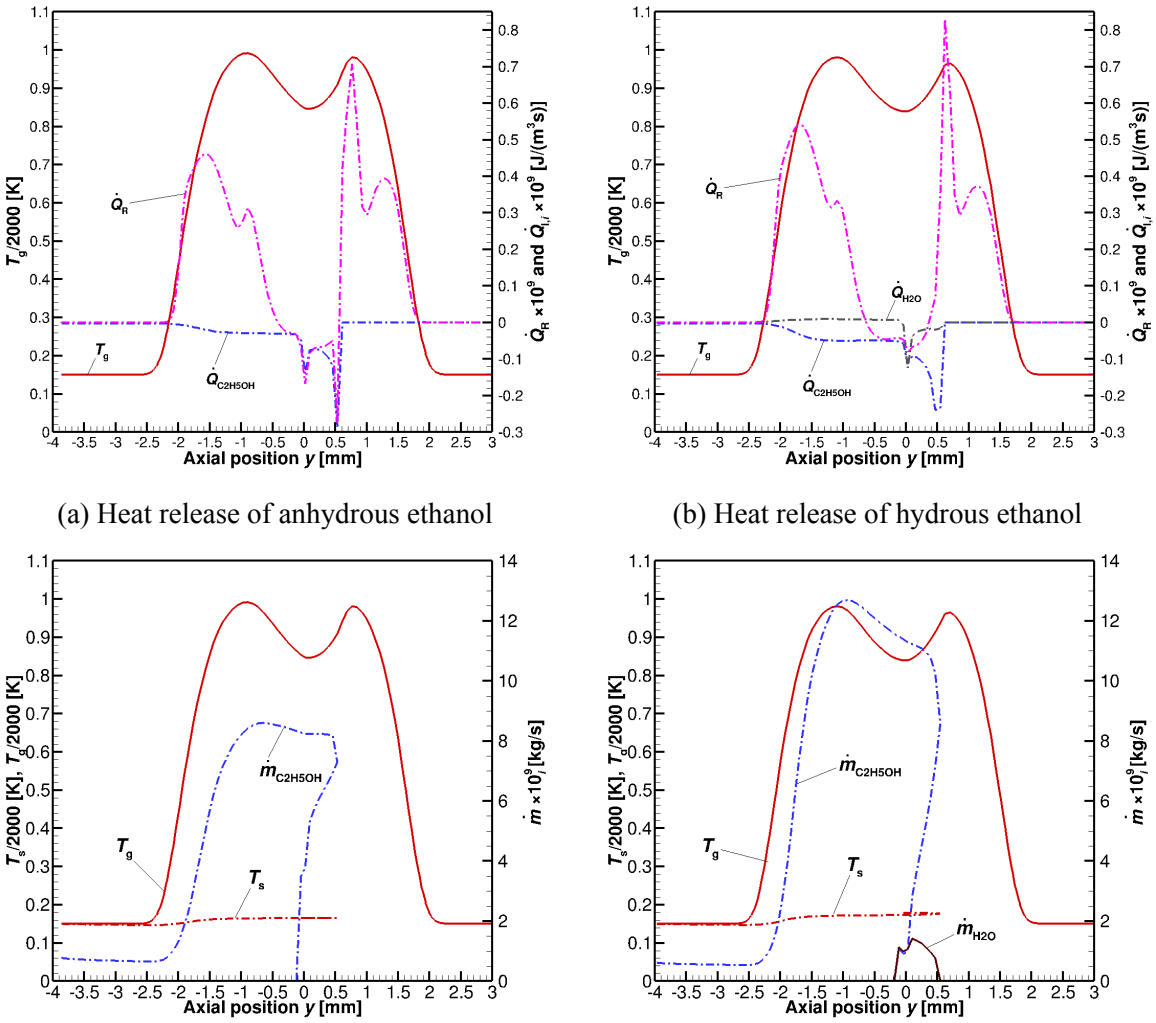

(a) Heat release of anhydrous ethanol

(b) Heat release of hydrous ethanol

(c) Mass evaporation rate of anhydrous ethanol

(d) Mass evaporation rate of hydrous ethanol

Figure 3.35: Heat release and mass evaporation rate of spray flame structures are presented under the condition: $R_0 = 30\,\mu$m, $T_{l,0} = T_{g,0} = 300$ K, $E_{-\infty} = 1.2$, and $a_{-\infty} = 200$/s, for different sprays. Left: anhydrous ethanol; Right: hydrous ethanol.

Figures 3.35(a-d) illustrate critical parameters such as heat release and mass evaporation rates for both anhydrous and hydrous ethanol spray flames under identical conditions as presented in Fig. 3.34, providing a comprehensive view of the combustion dynamics. In Figs. 3.35(a-b), the heat release rate profiles ($\dot{Q}_R$) largely reflect the gas temperature profiles but shift to negative values in regions of intense evaporation, as shown by the S_{v,C_2H_5OH} profiles in Fig. 3.35(a) and the S_{v,C_2H_5OH} and S_{v,H_2O} profiles in Fig. 3.35(b). In the hydrous ethanol spray flame, the endothermic profile due to ethanol evaporation ($\dot{Q}_{C_2H_5OH}$) extends

across the chemical reaction zone, whereas this profile of water ($\dot{Q}_{H_2O}$) is confined to a narrow region of 0.7 mm, as illustrated in Fig. 3.35(b). These variations are directly attributable to the different evaporation characteristics of ethanol and water. The mass evaporation rates ($\dot{m}$) of monocomponent and bicomponent droplet sprays are represented in Figs. 3.35(c) and 3.35(d), respectively, with the droplet surface temperature (T_s) provided for context. In the hydrous ethanol spray flame, the evaporation of ethanol accelerates, as seen in the $\dot{m}_{C_2H_5OH}$ profile in Fig. 3.35(d). This acceleration results from the rapid increase in droplet surface temperature to the wet-bulb temperature of ethanol at 351.4 K, whereas the maximum T_s in the anhydrous ethanol spray flame remains at 330.8 K. This quicker evaporation in the hydrous ethanol spray enhances the chemical reaction rate by providing a greater volume of vapor fuel, as illustrated by the $\dot{Q}_R$ profile in Fig. 3.35(b).

Despite numerical studies on the stoichiometric condition of ethanol spray flames [25, 26, 55, 158], fundamental research on hydrous ethanol spray combustion remains limited. Therefore, further investigations into this system under this condition are necessary. Numerical simulations are conducted to investigate the behavior of monodisperse hydrous ethanol spray flames in a counterflow configuration, maintaining the same conditions as presented in Figs. 3.34 and 3.35, except for a stoichiometric equivalence ratio of unity. Additionally, the flame structure of anhydrous ethanol spray is examined as a reference for comparing the combustion characteristics of hydrous ethanol sprays. Figure 3.36 illustrates the gas and chemical reaction rates of key species in spray flame structures for both anhydrous and hydrous ethanol. Fig 3.37 highlights essential parameters such as heat release and mass evaporation rates under the same condition.

The most notable difference in flame structures between droplets with and without water addition is the variation in gas temperature. In the anhydrous ethanol spray flame, the gas temperature within the dip reaches 1845 K, whereas the hydrous ethanol flame records a lower temperature of 1691 K. This reduction is attributed to the substantial energy consumed during water evaporation, which has a higher latent heat compared to ethanol, combined with the ”thermal effect” of gaseous H_2O [175], as illustrated by the mass profiles of H_2O in Figs. 3.36(a-b). An interesting phenomenon observed in hydrous ethanol spray flames under the stoichiometric condition is the conversion of CO to CO2, which exhibits a higher peak value compared to anhydrous ethanol spray flames. As discussed in Section 3.1, this inefficient conversion is associated with lower temperatures, leading to a relatively higher peak of CO in the hydrous ethanol spray flame. This trend, differing from that under fuel-rich conditions, indicates a competition between temperature and chemical effects. The variations in the chemical reaction rate profiles of ω_{CO}, as shown in Figs. 3.36(c-d), underscore the differences between anhydrous and hydrous ethanol spray flames. Specifically, the gaseous C_2H_5OH profiles exhibit significant variation. In the hydrous ethanol spray

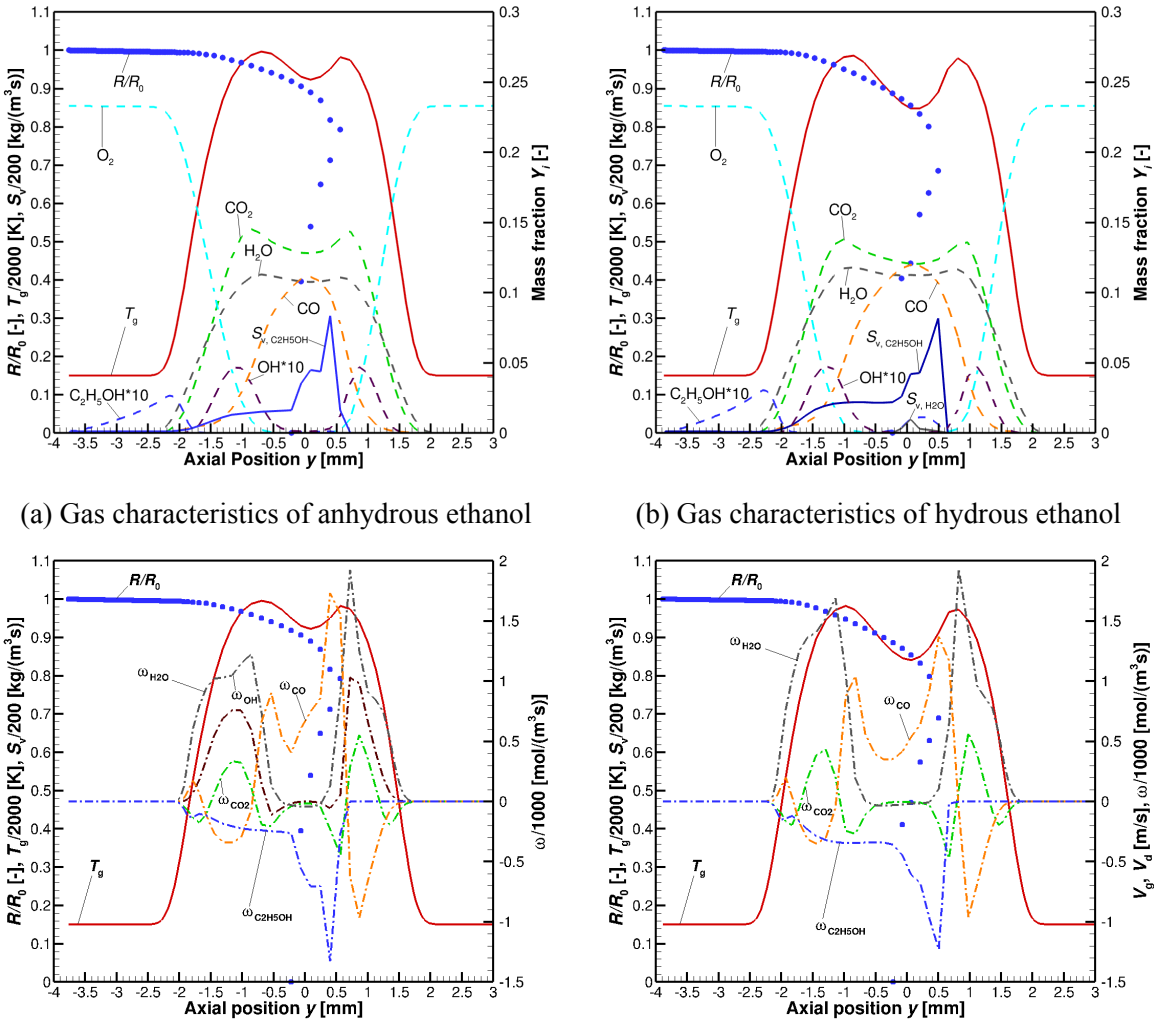

(a) Gas characteristics of anhydrous ethanol

(b) Gas characteristics of hydrous ethanol

(c) Chemical reaction rates

(d) Chemical reaction rates

Figure 3.36: Gas and chemical reaction rates of typical species of spray flame structures are presented under the condition: $R_0 = 30\,\mu\text{m}$, $T_{l,0} = T_{g,0} = 300$ K, $E_{-\infty} = 1.0$, and $a_{-\infty} = 200/\text{s}$, for different sprays. Left: anhydrous ethanol; Right: hydrous ethanol.

combustion, a higher value of 0.001 is observed at an axial position of 0.25 mm, a point where gaseous ethanol is nearly absent in the anhydrous flame. The H_2O profile undergoes the most notable change among all species in the hydrous ethanol spray flame, mainly due to the water introduced into the spray. This leads to a substantial increase in vapor production, as illustrated by the S_{v,H_2O} profile in Fig. 3.36(b), similar to results observed under fuel-rich conditions as shown in Fig. 3.35(b).

The heat release rate and endothermic profiles, seen in Fig. 3.37(a-b), demonstrate analogous characteristics under the stoichiometric condition as those observed under fuel-rich conditions for both anhydrous and hydrous ethanol spray flames. In the case of the hydrous ethanol spray flame, the evaporation pattern of the more volatile ethanol spans the chemical reaction zone on the spray side. Conversely, the rapid evaporation of water is limited to a

narrow region, approximately 0.6 mm in width, as shown in Fig. 3.37(b). The quicker evaporation in the hydrous ethanol spray is also identified under the stoichiometric condition, which enhances the chemical reaction rate of the flame by providing a greater volume of vapor fuel, as illustrated by the $\dot{Q}_R$ profile in Fig. 3.37(f).

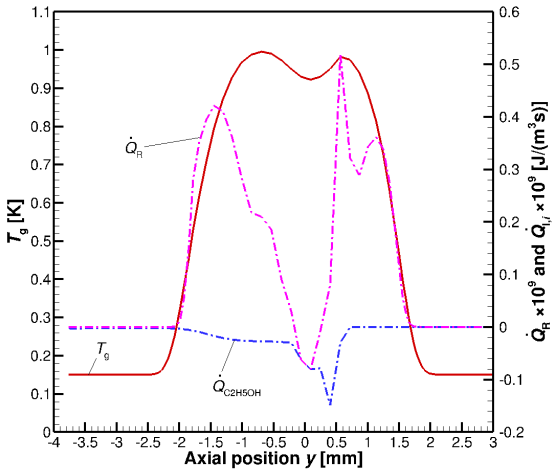

(a) Heat release of anhydrous ethanol

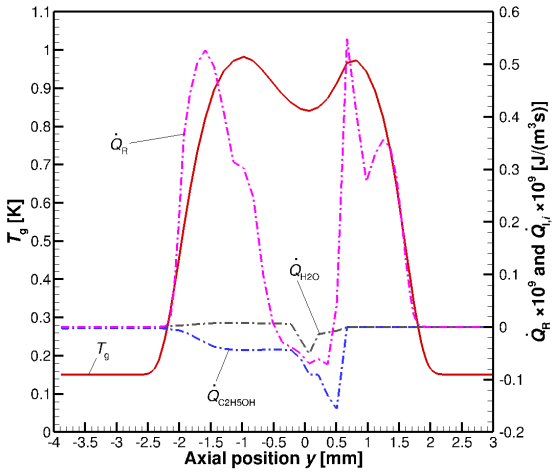

(b) Heat release of hydrous ethanol

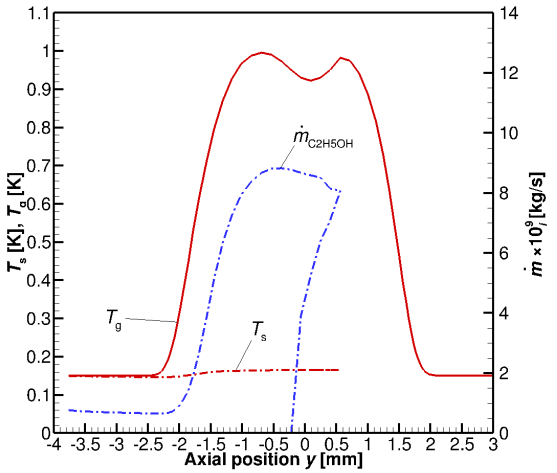

(c) Mass evaporation rate of anhydrous ethanol

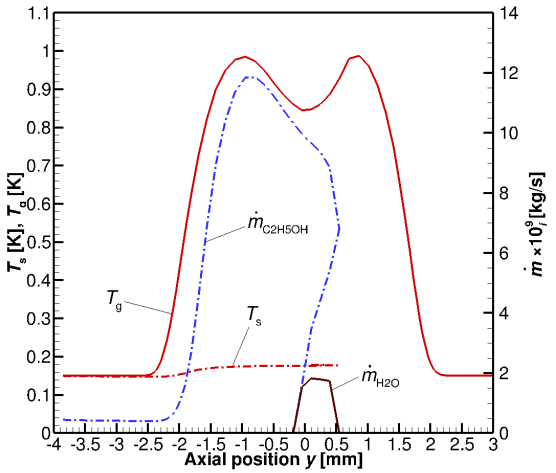

(d) Mass evaporation rate of hydrous ethanol

Figure 3.37: Heat release and mass evaporation rate of spray flame structures are presented under the condition: $R_0 = 30\,\mu$m, $T_{l,0} = T_{g,0} = 300$ K, $E_{-\infty} = 1.0$, and $a_{-\infty} = 200$/s, for different sprays. Left: anhydrous ethanol; Right: hydrous ethanol.

The influence of strain rate on hydrous ethanol spray flames is then analyzed under stoichiometric and fuel-rich conditions. For comparison, anhydrous ethanol flames are also examined. Figure 3.38 summarizes the relationship between local minimum and maximum flame temperatures and gas strain rate for the cases studied. The left subfigure presents the results under the stoichiometric condition, while the right subfigure displays the results for fuel-rich conditions with an equivalence ratio of 1.2. Solid lines and filled symbols represent anhydrous ethanol, whereas dashed lines and hollow symbols denote hydrous ethanol. Red

and green symbols indicate the peak gas temperatures on the spray and gas sides of the flame, respectively, while blue symbols denote the local minimum temperatures between these peaks.

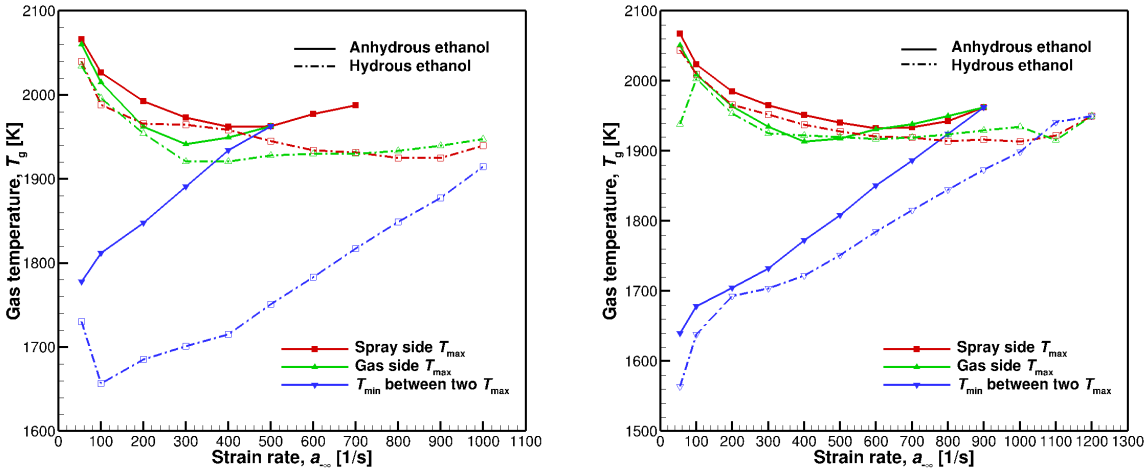

(a) $E_{-\infty}$ = 1.0 (b) $E_{-\infty}$ = 1.2

Figure 3.38: Local minimum and maximum gas temperatures versus strain rate for anhydrous and hydrous ethanol spray flames under stoichiometric and fuel-rich conditions.

Under both equivalence ratio conditions, the comparison of these two different spray flames consistently shows that hydrous ethanol flames exhibit lower peak temperatures and local minima compared to anhydrous ethanol flames, with the most significant differences observed at the local minima. This variation is primarily due to the addition of water to the spray, which absorbs a substantial amount of energy for evaporation, particularly where droplet evaporation intersects with the chemical reaction zone. The impact of water addition in the initial droplet sprays on the flame's temperature distribution also involves both the "dilution effect" and the "thermal effect" of water vapor profiles, which further decrease the gas temperature, as discussed in Qiu et al [175]. The profiles for the local minimum and two temperature peaks exhibit a consistent trend, closely aligning as the gas strain rate increases. Higher gas strain rates result in droplets with more momentum, which facilitates deeper penetration into the chemical reaction zone on the gas side. This deeper penetration and the resultant reversal oscillation of droplets near the stagnation point, as shown in Figs. 3.39 and 3.40, help introduce more fuel vapor into this zone, enhancing combustion and thus elevating the flame temperature. Under the stoichiometric condition, anhydrous ethanol exhibits converging temperature profiles at strain rates exceeding 500/s. In fuel-rich conditions, this convergence occurs at 900/s. For hydrous ethanol, no convergence is observed under the stoichiometric condition before the extinction strain rate. However, under fuel-rich conditions, convergence occurs at 1200/s prior to extinction. This discrepancy underscores the different dynamic responses of spray flames to the presence of water in

the fuel mixture, influencing both combustion efficiency and flame stability under varying operational conditions.

In the regime diagram of spray flame structures for anhydrous ethanol with an initial droplet radius $R_0 = 30$ µm, cf. Fig. 3.29b, it is observed that the gas strain rates required for spray flame extinction increase with the equivalence ratio. This behavior is also observed for hydrous ethanol. A more detailed discussion is provided below to analyze the flame extinction mechanism.

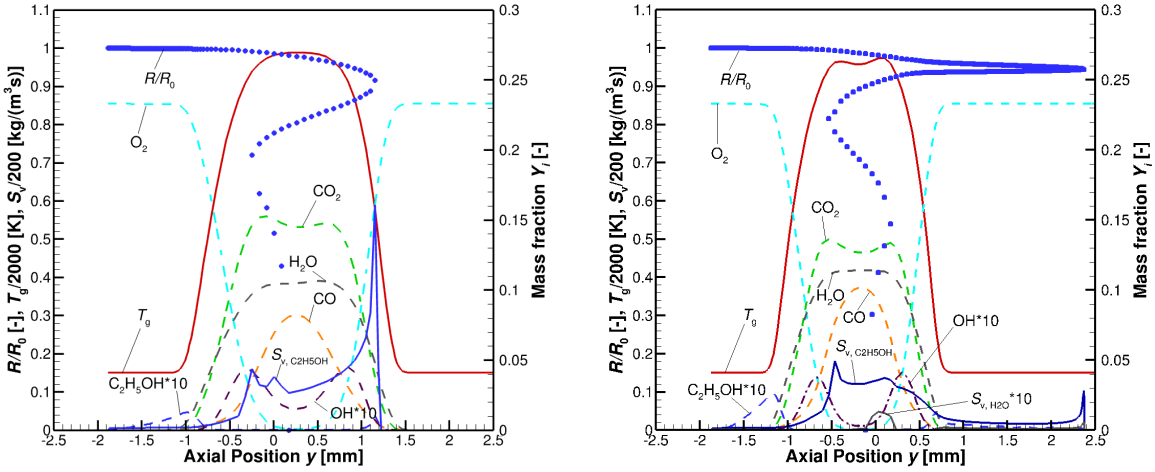

Figure 3.39: Spray flame structures under the condition: $R_0 = 30$ µm, $T_{l,0} = T_{g,0} = 300$ K, and $E_{-\infty} = 1.0$ for (a) anhydrous ethanol with $a_{-\infty} = 700$/s; (b) hydrous ethanol with $a_{-\infty} = 1000$/s.

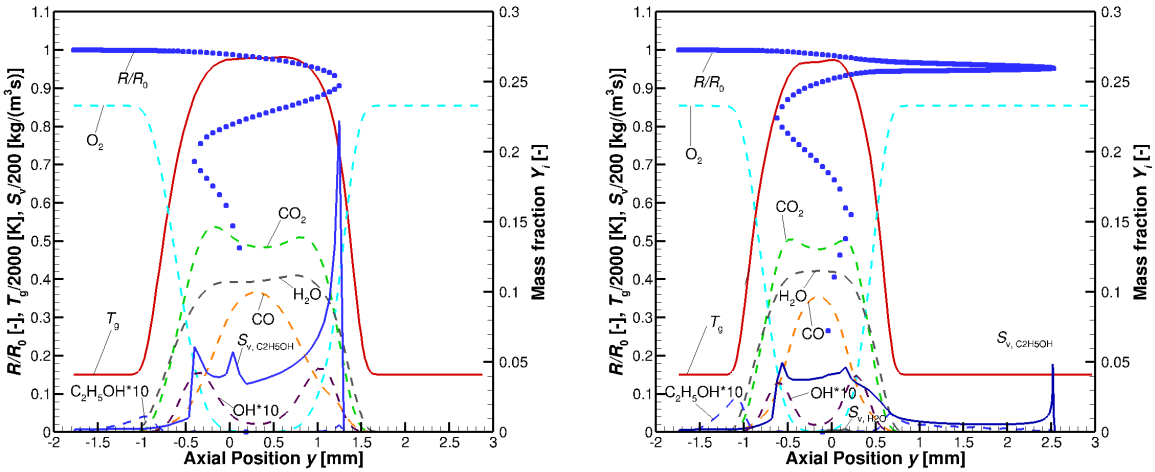

Figure 3.40: Spray flame structures under the condition: $R_0 = 30$ µm, $T_{l,0} = T_{g,0} = 300$ K, and $E_{-\infty} = 1.2$ for (a) anhydrous ethanol with $a_{-\infty} = 900$/s; (b) hydrous ethanol with $a_{-\infty} = 1200$/s.

The flame extinction strain rates for anhydrous and hydrous ethanol spray flames have been determined. Under the stoichiometric condition (cf. Fig 3.39), the anhydrous ethanol

flame extinguishes when the gas strain rate exceeds 700/s, whereas the hydrous ethanol flame persists up to 1000/s. Under fuel-rich conditions with an equivalence ratio of 1.2, seen in Fig. 3.40, the respective values are 900/s and 1200/s. Under both equivalence ratio conditions, this distinction is illustrated in Figs. 3.39 and 3.40. Comparing these figures with the cases at a lower strain rate of 200/s shown in Figs. 3.36 and 3.34 reveals that at higher strain rates, droplets in both spray flames cross the stagnation plane and reverse on the air side of the configuration. In the case of the hydrous spray, the droplets remain distant from the chemical reaction zone. The flame structure breakdown occurs when the evaporation process cannot be sustained due to the increased gas strain rate. As the gas strain rate increases, the spray flames narrow, allowing for deeper penetration of the spray into the configuration. Unlike the anhydrous ethanol spray flame, which shows a single peak in the gas temperature profile, the hydrous ethanol flame maintains a distinct dual peak. A notable characteristic of the hydrous ethanol spray flame is the penetration of droplets into the colder regions of the flame. Minor vaporization occurs throughout the gas side of the configuration, except at the turning point, where dramatic evaporation happens due to the extended residence time of droplets in this area. Consequently, the spray evaporation zone on the gas side is positioned outside the chemical reaction zone, as shown in Figs. 3.39(b) and 3.40(b). When the strain rate exceeds the critical values (1000/s under the stoichiometric condition and 1200/s at an equivalence ratio of 1.2), the droplet sprays, carrying significant momentum, exit the reaction zone. This results in unsustainable spray flame conditions. Contrary to typical gas combustion where flame extinction is often attributed to reduced chemical reaction times, the extinction of the spray flame is due to a different mechanism. For both anhydrous and hydrous ethanol spray flames, extinction is linked to the disruption of spray evaporation, which occurs when the energy provided by the combustion process is insufficient to sustain the evaporation needed for continuous combustion [28, 61].

3.2.3 Multiple Spray Flames Structures

Laminar spray flames often exhibit multiple structures under identical initial and boundary conditions, as theoretically proposed by Continillo and Sirignano [46] and subsequently validated through numerical simulations for monocomponent fuels [28, 29, 56, 57, 136, 137]. In Subsection 3.1.2, the triple flame structure of anhydrous ethanol spray flame is comprehensively analyzed under fuel-rich conditions. This study also identifies multiple structures of hydrous ethanol laminar spray flame under conditions with $R_0 = 30\,\mu\text{m}$, $E_{-\infty} = 1.2$, and $a_{-\infty} = 200/\text{s}$. Figure 3.41(a) illustrates the gas-sided flame structure, marked by a single chemical reaction on the gas side. In contrast, Figure 3.41(b) presents the spray-sided flame structure, characterized by a single chemical reaction on the spray side. Along with

the two-reaction-zone flame structure shown in Fig. 3.34(b), these observations confirm the coexistence of three distinct flame structures of hydrous ethanol spray under the same initial and boundary conditions. Moreover, in addition to fuel-rich conditions, the triple flame structure of a hydrous ethanol spray flame is also observed under the stoichiometric condition, as depicted in Figs. 3.36(b), 3.42(a) and 3.42(b), with parameters of $R_0 = 30$ μm, $E_{-\infty}$ = 1.0, and $a_{-\infty}$ = 200/s. In contrast, for anhydrous ethanol spray, only a unique two-reaction flame structure is observed under the stoichiometric condition, as illustrated in Fig. 3.36(a). This differs from the multiple flame structures seen under fuel-rich conditions [29]. This shift is attributed to the transition mechanism known as the 'shoulder shape,' as described in previous Subsection 3.1.1.

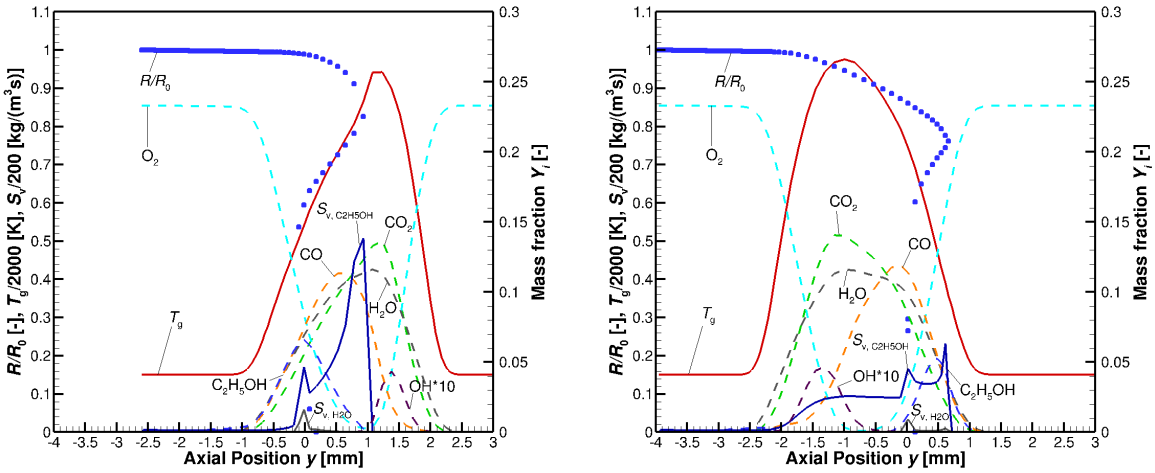

Figure 3.41: (a) Gas-sided and (b) spray-sided hydrous ethanol spray flame structures under the same condition with Fig. 3.34.

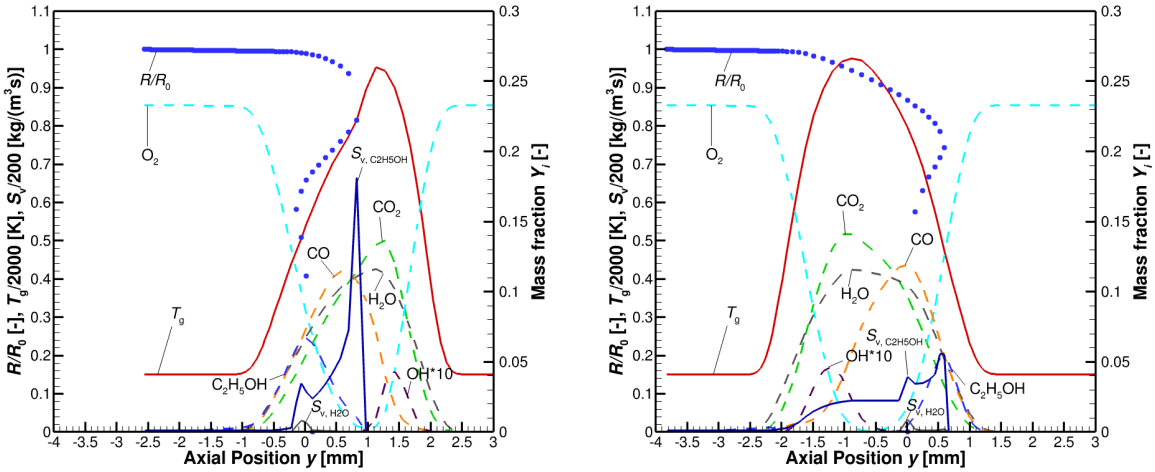

Figure 3.42: (a) Gas-sided and (b) spray-sided hydrous ethanol spray flame structures under the same condition with Fig. 3.36.

The presence of multiple spray flame structures of hydrous ethanol could offer valuable insights into understanding pulsations that may occur in spray flames, as indicated by the abrupt transitions between these structures [29, 176], potentially contributing to significant flame instabilities influenced by spray characteristics [171]. The flame instability of hydrous ethanol has been experimentally confirmed by Xu et al. [177] and Lama et al. [94], suggesting that further research is needed to systematically explore the multiple structures and transition mechanisms in hydrous ethanol laminar spray flames. The regime diagrams presented in Subsection 3.1.2 also hint at potential reasons for flame instability due to the transition between different flame structures.

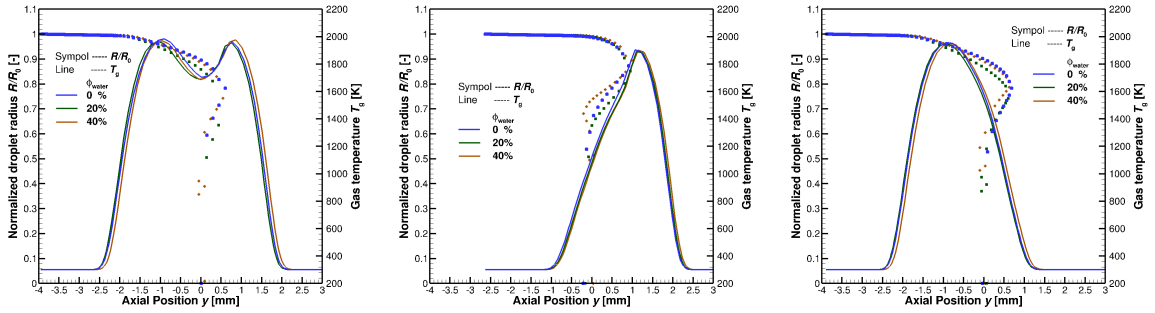

(a) Two reaction zones (b) Gas-sided reaction zone (c) Spray-sided reaction zone

Figure 3.43: Different flame structures for $R_0 = 30\,\mu m$, $T_{l,0} = T_{g,0} = 300$ K, $E_{-\infty} = 1.2$, and $a_{-\infty} = 200$/s, for various ethanol droplet sprays with different water volume fractions (a): 0%; (b) 20%; (c): 40%.

The impact of the concentration of component water in the hydrous ethanol droplet on the transitional behavior of flame structures is analyzed. Figure 3.43 presents the temperature profiles and normalized droplet radii in physical space for an initial droplet size of 30 µm, an equivalence ratio of 1.2 and a gas strain rate of 200/s across various volume fractions of the water component. The analysis is conducted across different volume fractions of water: 0%; 20%; 40%. Notably, the water fraction appears to have minimal impact on the width of the flame, the maximum flame temperatures, and the depth to which droplets penetrate the flame. The most significant effect of varying the water fraction is observed in hydrous ethanol droplet spray behavior, specifically in terms of reversal and oscillation at the stagnation position, indicating that alterations in water fraction affect evaporation characteristics, particularly nearing total evaporation. The observed behavior of droplet evaporation can be attributed to the varying evaporation characteristics of its components. This phenomenon is demonstrated already in both pure heating and evaporation processes, as shown in Fig. 3.33. Furthermore, variations in water fraction impact the minimum temperature and the associated vaporization dynamics in the double flame structure.

In the subsequent section, the extended model for laminar spray flames of multicomponent systems is applied to explore the behavior of TTIP/*p*-xylene precursor solution droplets.

3.3 TTIP/p-xylene Spray Flames

This study focuses on the numerical simulation of heating, evaporation, and combustion of a monodisperse, laminar TTIP/p-xylene precursor solution spray in a counterflow configuration. This discussion is adapted from Ying and Gutheil [141], with the exception of the findings in Subsection 3.3.3. An advanced chemical reaction mechanism, which accounts for both the combustion of the mixture and the thermal decomposition of TTIP, is considered alongside the various physical properties of the precursor solution. These properties are detailed in Subsection 2.2.5. Using the validated model from Section 3.2, this analysis incorporates the unique physical properties of the precursor solution and employs a sophisticated chemical reaction mechanism to accurately capture the thermal decomposition of TTIP and the combustion process. Special attention is given to the thermophysical properties of the multicomponent droplet and gas-phase species to ensure precise representation under reactive conditions. These simulations enhance the understanding of precursor solution modeling and combustion within the context of nanoparticle formation in FSP and aid in creating spray flamelet libraries for turbulent combustion simulations.

In this study, the typical flame structure of a bi-component TTIP/p-xylene precursor solution is initially examined and compared with a pure p-xylene spray flame structure to assess the general impact of the precursor solution on spray flame dynamics. Following this, a detailed parameter study of monodisperse TTIP/p-xylene spray flames in air is conducted. Under specific conditions, the analysis reveals the presence of multiple spray flame structures, providing insights into the complex interactions between the physical and chemical processes influencing flame behavior.

3.3.1 Structures of p-Xylene and TTIP/p-xylene Spray Flames

The monodisperse precursor solution spray flames within a counterflow configuration were numerically investigated, with the system maintained at atmospheric pressure and both the initial gas and spray temperatures set at 300 K. The specific conditions evaluated in this study are outlined in Table 3.1. Note that the equivalence ratios ($E_{-\infty}$, cf. Eq. 2.56) listed in the table are based on the fuel p-xylene in air, using its global reaction. This approach is adopted because the thermal decomposition and chemical reaction of the TTIP are not assumed to be complete within the scope of this investigation. Initially, the study conducts a comparative analysis between a pure p-xylene spray flame (case #1) and a spray flame from a bi-component precursor solution (case #2). This comparison aims to elucidate the general effects that the precursor solution exerts on the structure of spray flames. Subsequently, a detailed parameter study is performed to investigate the impact of various factors

Table 3.1: Simulation conditions [28].

Case #	R_0 [µm]	$E_{-\infty}$ [-]	$a_{-\infty}$ [1/s]	$Y_{p\text{-xylene},0}$ [-]	$Y_{\text{TTIP},0}$ [-]
1	25	0.8	100	1.0	0.0
2	25	0.8	100	0.975	0.025
3	25	1.0	100	0.975	0.025
4	10	0.8	100	0.975	0.025
5	50	0.8	100	0.975	0.025
6	25	0.8	1,200	0.975	0.025
7	25	0.8	1,235	0.975	0.025
8	25	0.8	100	0.845	0.155
9	25	0.8	100	0.750	0.250

on spray flame behavior. These factors include different initial gas strain rates, droplet radii, equivalence ratios, and mass loadings of the precursor in the solution. This comprehensive examination helps in understanding the dynamic interactions and modifications in flame characteristics due to changes in these key parameters.

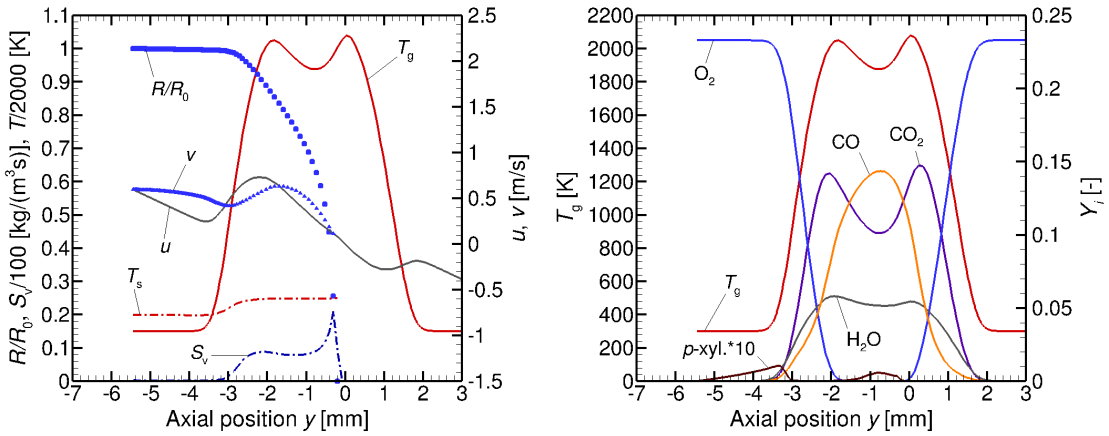

(a) Spray characteristics (b) Mass fractions of major species

Figure 3.44: Case #1. Pure *p*-xylene spray flame structure. $R_0 = 25\,\mu\text{m}$, $E_{-\infty} = 0.8$, $T_{l,0} = T_{g,0} = 300$ K, $a_{-\infty} = 100$/s, $Y_{p\text{-xylene}} = 1.0$, $Y_{\text{TTIP}} = 0.0$ [28].

Figures 3.44 and 3.45 illustrate the spray flame structures of a monodisperse *p*-xylene spray and a TTIP/*p*-xylene precursor solution spray, respectively, within a counterflow configuration. The latter features an initial composition of $Y_{p\text{-xylene}} = 0.975$ and $Y_{\text{TTIP}} = 0.025$ as detailed in Table 3.1. In this setup, the precursor solution, carried by air, is injected from one side and meets an opposing air stream, establishing a spray-sided gas strain rate of

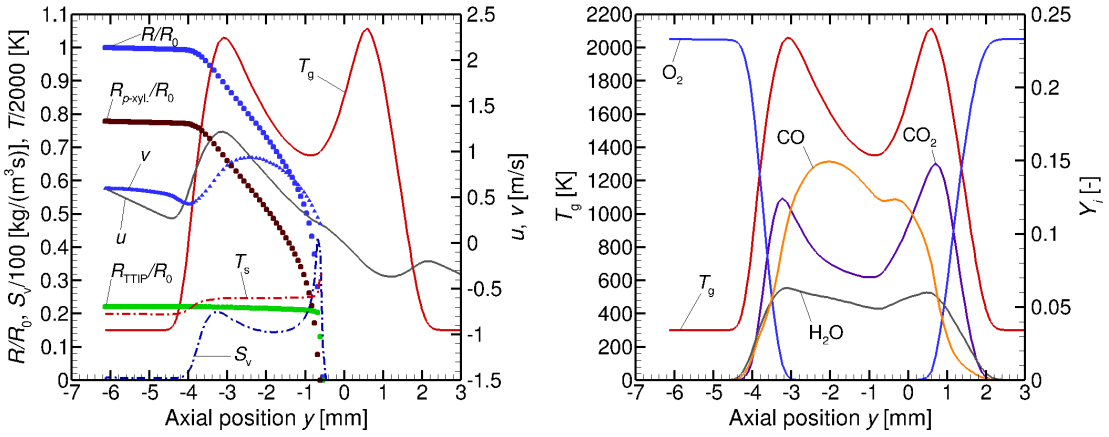

(a) Spray characteristics (b) Mass fractions of major species

Figure 3.45: Case #2. TTIP/p-xylene spray flame structure. $R_0 = 25\,\mu$m, $E_{-\infty} = 0.8$, $T_{\mathrm{l},0} = T_{\mathrm{g},0} = 300$ K, $a_{-\infty} = 100$/s, $Y_{p\text{-xylene}} = 0.975$, $Y_{\mathrm{TTIP}} = 0.025$ [28].

$a_{-\infty} = 100$/s. Both the initial gas and liquid temperatures are maintained at 300 K, with an initial droplet radius of 25 µm and an equivalence ratio $E_{-\infty} = 0.8$ at atmospheric pressure. The axial position $y = 0$ mm marks the gas stagnation plane, denoting the point of zero net flow where the opposed air streams interact.

The left parts of Figs. 3.44 and 3.45 illustrate the outer flame structures, emphasizing the liquid phase characteristics of monodisperse sprays of p-xylene and a TTIP/p-xylene precursor solution, respectively. In the depiction of the precursor solution in Fig. 3.45a, the normalized droplet radii for TTIP (R_{TTIP}/R_0) and p-xylene ($R_{p-\mathrm{xyl.}}/R_0$) are shown, as referenced in Eq. (2.57). A significant difference observed between the flame structures—with and without the precursor—concerns the gas temperature profiles. In both scenarios, two peaks are visible, indicating the presence of two chemical reaction zones with a noticeable dip occurring in the region of major vaporization of the spray. For the pure p-xylene spray flame, the gas temperature in the dip reaches 1876 K, while for the precursor solution flame, it drops to 1352 K. The flame incorporating the precursor solution extends further toward the spray side of the configuration. This extension is attributed to the faster evaporation of the more volatile component, p-xylene, as evident in the profile of the mass evaporation rate (S_{v}), allowing combustion to occur closer to the spray side. Furthermore, major evaporation of TTIP, which has a higher boiling point than p-xylene, predominantly occurs near the stagnation plane, contributing to the substantial reduction in flame temperature in that region. The droplet surface temperature (T_{s}) profile exhibits a second rise in the case of precursor solution evaporation, indicative of the complex evaporation dynamics typical for such multicomponent liquids as discussed by Narasu et al. [111].

In Figs. 3.44b and 3.45b, the chemical species profiles for H_2O, CO_2, and CO are pre-

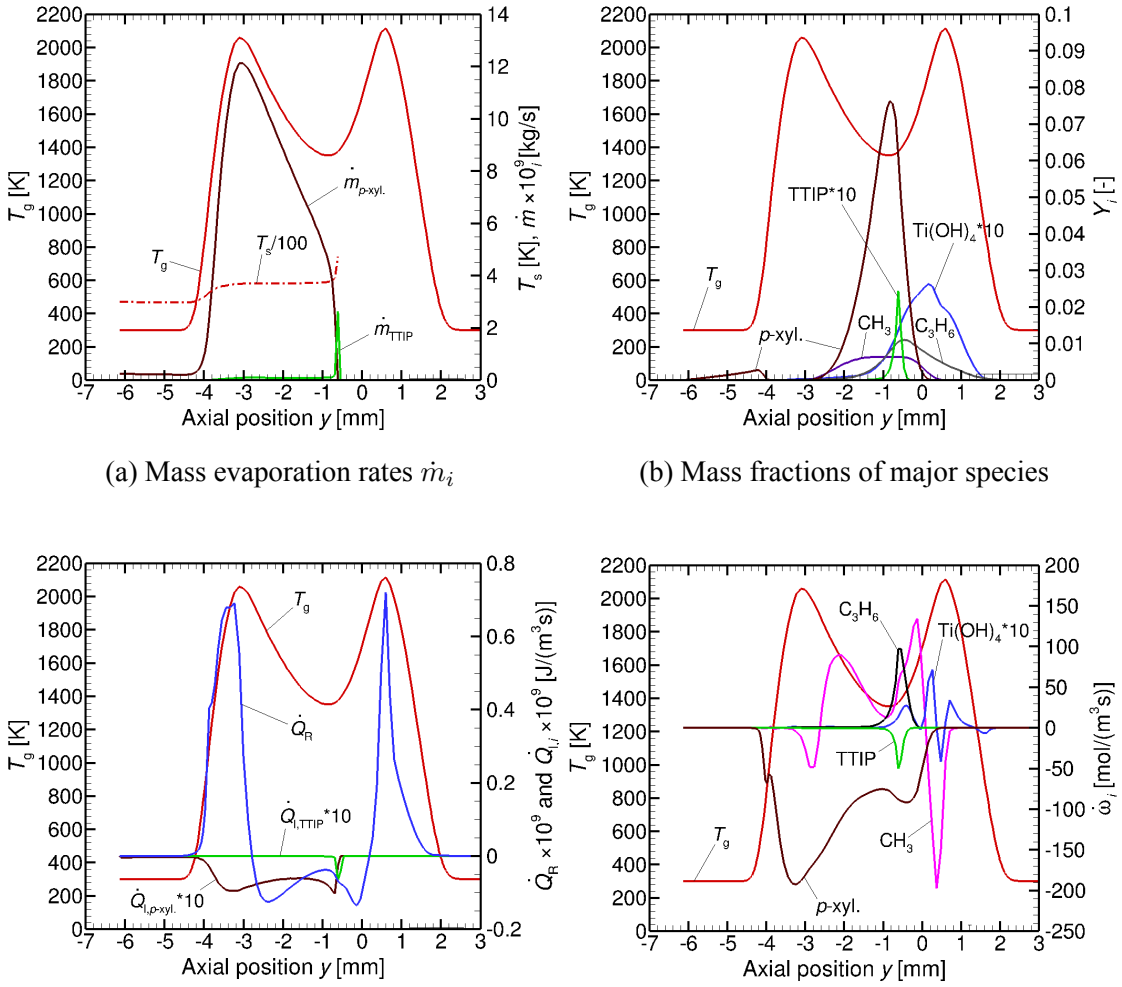

(a) Mass evaporation rates $\dot{m}_i$

(b) Mass fractions of major species

(c) Heat release rate $\dot{Q}_R$ and energy transfer $\dot{Q}_{l,i}$

(d) Reaction rates

Figure 3.46: Case #2. TTIP/*p*-xylene spray flame structure for $R_0 = 25$ µm, $E_{-\infty} = 0.8$, $T_{l,0} = T_{g,0} = 300$ K, $a_{-\infty} = 100$/s, $Y_{p\text{-xylene}} = 0.975$, $Y_{TTIP} = 0.025$ [28].

sented, with additional focus on *p*-xylene in Fig. 3.44b. The different evaporation characteristics between the *p*-xylene spray flame and the TTIP/*p*-xylene precursor solution flame are particularly evident in the CO profiles. For the *p*-xylene spray flame, a single peak is observed, whereas the precursor solution flame shows two peaks, with the major peak positioned between -3 mm and -2 mm and a smaller one just prior to the stagnation plane, where all droplets evaporate. A dip between these peaks is noted, attributable to the low gas temperature in this region. Figure 3.46 delves deeper into the characteristics of the TTIP/*p*-xylene spray flame. The evaporation characteristics of the two liquid components are detailed in Fig. 3.46a, where the individual mass evaporation rates for *p*-xylene and TTIP are displayed alongside the droplet surface temperature (T_s) and the gas temperature for reference. The evaporation of the more volatile component, *p*-xylene, occurs near the spray injection on the spray side of the configuration within the spray-sided reaction zone.

This region is where the droplet surface temperature reaches the wet-bulb temperature of p-xylene, facilitating quasi-steady evaporation of this component [111]. Subsequently, as the droplet surface temperature increases, reaching approximately $y = 0.62$ mm, TTIP undergoes rapid evaporation, reflecting the complex interplay of thermal properties and chemical kinetics in the spray flame.

Figure 3.46b presents the profile of the mass fraction of p-xylene vapor, highlighting a prominent peak in the low-temperature region of the flame. This contrasts with the pure p-xylene spray flame, where higher temperatures facilitate chemical reactions. The differential evaporation characteristics of TTIP and p-xylene are further elucidated in Figs. 3.46a and 3.46c, which depict their contributions to the mass evaporation rate ($\dot{m}_i$) and energy transfer ($\dot{Q}_{l,i}$), as detailed in Eqs. (2.57) and (2.30). The heat release rate primarily follows the gas temperature profile but turns negative in regions of intense evaporation. While the evaporation of the more volatile component, p-xylene, spans the spray-sided chemical reaction zone, TTIP's rapid evaporation is confined to a narrow area around -0.3 mm, where the droplet surface temperature is sufficiently high to sustain its evaporation. The vaporization characteristics of the precursor solution spray influence the chemical reactions, as demonstrated in Figs. 3.45b and 3.46b. Profiles of combustion products such as CO, CO_2, H_2O, and notably $Ti(OH)_4$ and species like C_3H_6 and CH_3 (involved in its formation) are displayed in Fig. 3.46d. The profiles of these chemical reaction products generally track the gas temperature, exhibiting two local maxima except for CO, which peaks in the cooler region between the two chemical reaction zones where the gas temperature is insufficient to convert CO into CO_2.

Both TTIP and p-xylene are not fully consumed and exhibit peaks in the cooler flame regime. This is particularly problematic for TTIP, as its presence in this region can negatively impact the efficiency of TiO_2 nanoparticle formation. Conversely, p-xylene is predominantly consumed in the spray-sided chemical reaction zone, as its vaporization occurs closer to the spray injection. Spray flame structures with two chemical reaction zones typically persist in conditions of high strain rates or large droplet sizes, potentially adversely affecting nanoparticle production in these settings. The upcoming parameter study will provide more detailed insights into these phenomena.

3.3.2 Parameter Study

A comprehensive parameter study is conducted on monodisperse TTIP/p-xylene spray flames in air, exploring a range of variables that influence flame behavior. This study includes adjustments to the equivalence ratio ($E_{-\infty}$), the initial droplet radius (R_0), the initial gas strain rate ($a_{-\infty}$), and the mass loading of the precursor (Y_{TTIP}).

Equivalence ratio

The influence of the equivalence ratio ($E_{-\infty}$) on TTIP/*p*-xylene spray flames is initially explored.

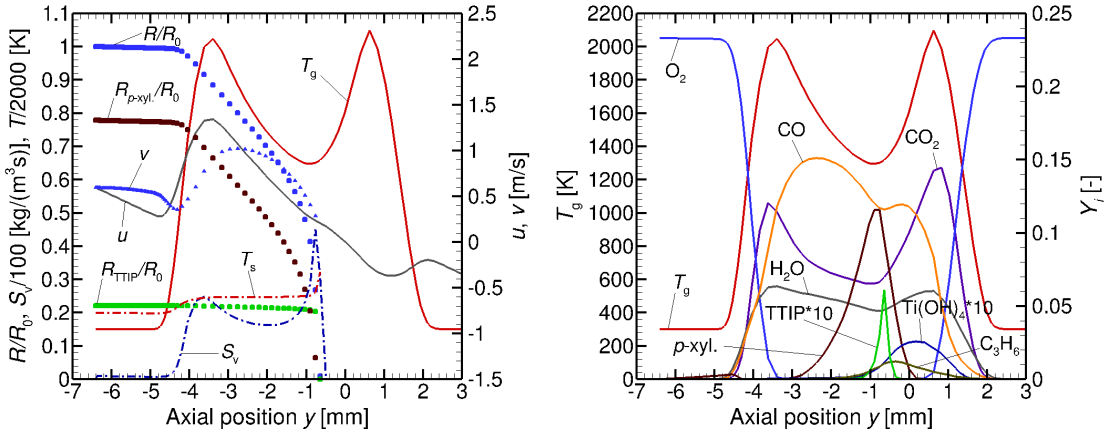

(a) Spray characteristics (b) Outer flame structure

Figure 3.47: Case #3. TTIP/*p*-xylene spray flame structure for $R_0 = 25$ µm, $E_{-\infty}$ = 1.0, $T_{l,0} = T_{g,0}$ = 300 K, $a_{-\infty}$ = 100/s, $Y_{p\text{-xylene}}$ = 0.975, Y_{TTIP} = 0.025 [28].

The equivalence ratio $E_{-\infty}$ is increased from 0.8 to 1.0, where all other conditions are fixed, see case #3. The results are shown in Fig. 3.47, which should be compared to Figs. 3.45 and 3.46 (case #2). The principal flame characteristics are the same with the exception of the peak values of the vaporized *p*-xylene mass fraction in the region where the dip in the gas temperature profile resides: the maximum value increases from about 0.077 to about 0.162. At higher equivalence ratios, more mass has to be evaporated which is reflected in the higher peak of the evaporation rate S_v on the spray side of the configuration, and the gas temperature of the right wing of the spray-sided reaction zone is somewhat bended to lower temperature values. The dip in the gas temperature profile is about 55 K lower at the higher equivalence ratio, and therefore, the mass fraction of the TTIP is higher due to its higher evaporation rate, causing a lower peak in the mass fraction of the $Ti(OH)_4$ in that region because of a retardation of chemical reactions associated with the lower gas temperature.

As part of a detailed parameter study, the equivalence ratio ($E_{-\infty}$) is adjusted from 0.8 to 1.0, while all other conditions remain constant (case #3). The effects of this adjustment are illustrated in Fig. 3.47, which should be compared with Figs. 3.45 and 3.46 (case #2). While the fundamental flame characteristics remain largely unchanged, notable differences are observed in the peak values of the vaporized *p*-xylene mass fraction, particularly in the region corresponding to the dip in the gas temperature profile. Specifically, the maximum value

of the vaporized *p*-xylene mass fraction increases significantly from approximately 0.077 to about 0.162. At the higher equivalence ratio of 1.0, there is a greater mass of fuel that needs to be evaporated, which is reflected in a heightened peak in the evaporation rate (S_v) on the spray side of the configuration. This increase in the evaporation rate consequently causes a slight bending of the gas temperature profile on the right wing of the spray-sided reaction zone towards lower temperatures. The dip in the gas temperature profile is approximately 55 K lower at the higher equivalence ratio, which enhances the mass fraction of TTIP due to its increased evaporation rate. This elevated rate of evaporation leads to a lower peak in the mass fraction of $Ti(OH)_4$ in that region, as the accelerated evaporation rate is coupled with a retardation of chemical reactions due to the cooler gas temperature. Thus, increasing the equivalence ratio can result in higher amounts of evaporated TTIP. However, this does not necessarily translate into a higher yield of TiO_2 nanoparticles.

Droplet size

The impact of varying the initial droplet radius in monodisperse spray flames is explored in cases #4, #1, and #5, as detailed in Table 3.1, which respectively examine droplet radii of 10 µm, 25 µm, and 50 µm. Figures 3.48 and 3.49 illustrate the spray flame structures for the smallest and largest droplet sizes considered. As established in prior research [28, 133], the size of the droplet plays a critical role in determining its penetration depth into the chemical reaction zone and whether it traverses this zone entirely. Larger droplets, possessing greater momentum, are able to travel further across the mixing layer and deeper into the counterflow configuration. This enhanced penetration leads to reversal and oscillation behaviors due to the opposing air stream and the intrinsic counterflow dynamics, which are characteristic features of these flames [47, 178].

In the current situation of the precursor solution spray, the behavior of droplets with different initial radii shows significant variation in evaporation and chemical reaction dynamics. For the spray with an initial droplet radius of 10 µm, evaporation occurs rapidly within a mere 2 mm from the point of injection, which is then followed by a broad chemical reaction zone spanning approximately 8 mm where $Ti(OH)_4$ is synthesized. Conversely, in the spray flame involving the largest initial droplet radius of 50 µm, the zone of $Ti(OH)_4$ production is considerably more compact, covering only about 5 mm. This observation raises intriguing questions about the potential effects this could have on the particle formation of TiO_2, which warrants further investigation. It can be concluded that in the case of the spray with the smaller droplet radius, chemical reactions primarily shape the flame structure, resulting in a situation akin to pre-vaporization, where reactants are almost entirely converted before reaching the central reaction zone. On the other hand, for sprays with the largest droplet radius, vaporization processes are predominant. Due to the oscillation and reversal

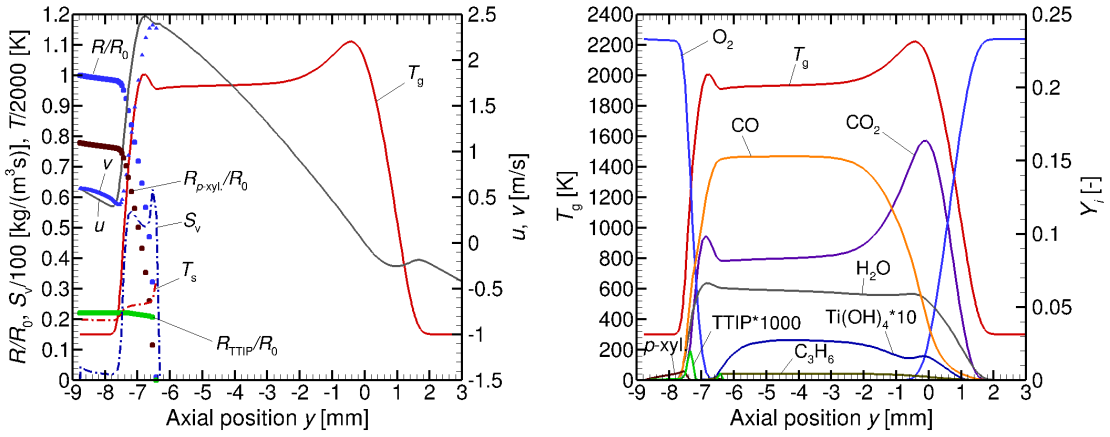

(a) Spray characteristics (b) Outer flame structure

Figure 3.48: Case #4. TTIP/*p*-xylene spray flame structure for $R_0 = 10\,\mu\text{m}$, $E_{-\infty} = 0.8$, $T_{\text{l},0} = T_{\text{g},0} = 300$ K, $a_{-\infty} = 100/\text{s}$, $Y_{p\text{-xylene}} = 0.975$, $Y_{\text{TTIP}} = 0.025$ [28].

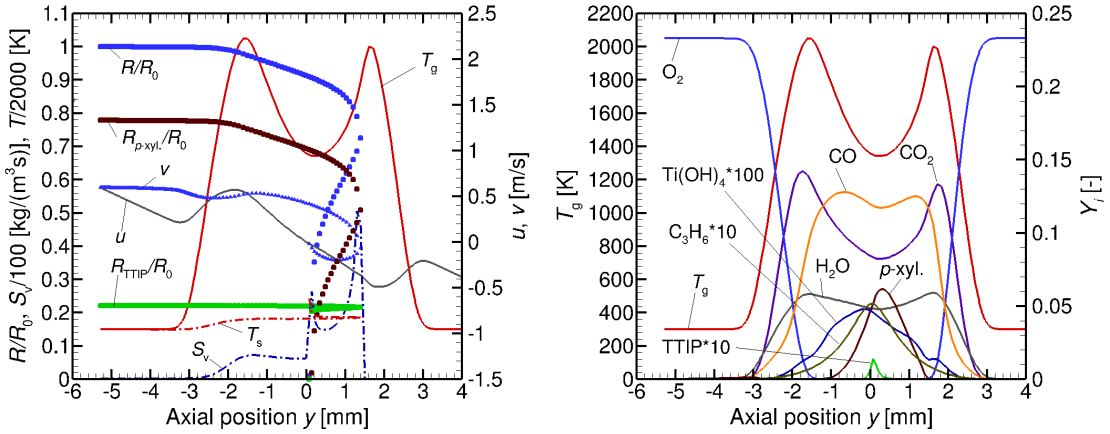

(a) Spray characteristics (b) Outer flame structure

Figure 3.49: Case #5. TTIP/*p*-xylene spray flame structure for $R_0 = 50\,\mu\text{m}$, $E_{-\infty} = 0.8$, $T_{\text{l},0} = T_{\text{g},0} = 300$ K, $a_{-\infty} = 100/\text{s}$, $Y_{p\text{-xylene}} = 0.975$, $Y_{\text{TTIP}} = 0.025$ [28].

behaviors of these larger droplets, their complete evaporation occurs close to the stagnation plane, leading to a noticeable dip in the gas temperature profile. This cooling effect retards the chemical reactions in this region, causing both TTIP and *p*-xylene vapor to be incompletely consumed, thereby introducing some inefficiencies into the process. This distinction highlights the critical interplay between droplet size, vaporization dynamics, and chemical reaction kinetics, all of which crucially influence the overall efficiency and outcome of the nanoparticle synthesis process.

Gas strain rate

To explore the impact of increased gas strain rates on the spray side of the counterflow configuration, the rate $a_{-\infty}$ is increased from 100/s as shown in Fig. 3.45 (case #2) to 1,200/s in Fig. 3.50 (case #6) and further to 1,235/s as represented in Fig. 3.51 (case #7). The spray flame ceases to exist at gas strain rates beyond 1,235/s. Comparing the flame structures at 1,200/s and 1,235/s reveals significant changes in both spray and gas flame characteristics due to the increase in strain rate. At the higher strain rate of 1,200/s, the droplets move out of the chemical reaction zone and are located on the gas side of the counterflow configuration, within the cold flame region. In this zone, no vaporization occurs except at the turning point on the gas side, where the prolonged residence time of the droplets facilitates vaporization. This leads to an extinction of the gas-sided chemical reaction zone. At a strain rate of 1,235/s, the dynamics shift such that the characteristic behavior of the droplet surface temperature (T_s)—indicative of the evaporation of high and low volatile components of the precursor solution—is lost due to the droplets crossing and exiting the chemical reaction zone. Monitoring the Lagrangian (temporal) development of T_s, it is observed that at approximately -0.4 mm, the wet-bulb temperature of the p-xylene is reached, enabling quasi-steady vaporization of p-xylene, followed by a decrease in T_s as the droplets remain within the low-temperature zone on the gas side. Upon reversing and re-entering the hot reaction zone, T_s rises again, promoting further evaporation. After the second droplet reversal, T_s escalates beyond the boiling temperature of p-xylene, facilitating the evaporation of TTIP. This sequence is visualized in Fig. 3.52a, which shows the profile of energy transfer to the droplet, $\dot{Q}_{l,TTIP}$. At a gas strain rate of 1,200/s, the dip in the gas temperature profile

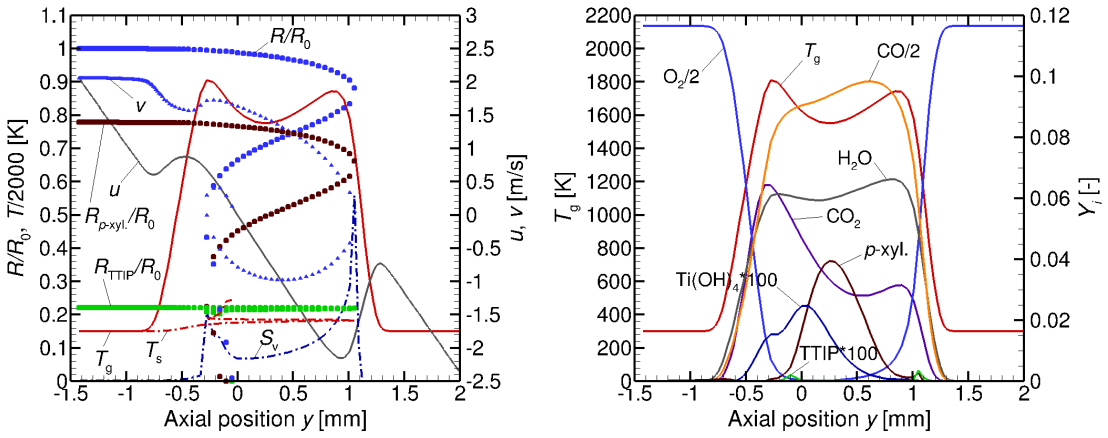

(a) Spray characteristics (b) Outer flame structure

Figure 3.50: Case #6. Extended grid case: TTIP/p-xylene spray flame structure for R_0 = 25 µm, $E_{-\infty}$ = 0.8, $T_{l,0}$ = $T_{g,0}$ = 300 K, $a_{-\infty}$ = 1200/s, $Y_{p\text{-xylene}}$ = 0.975, Y_{TTIP} = 0.025 [28].

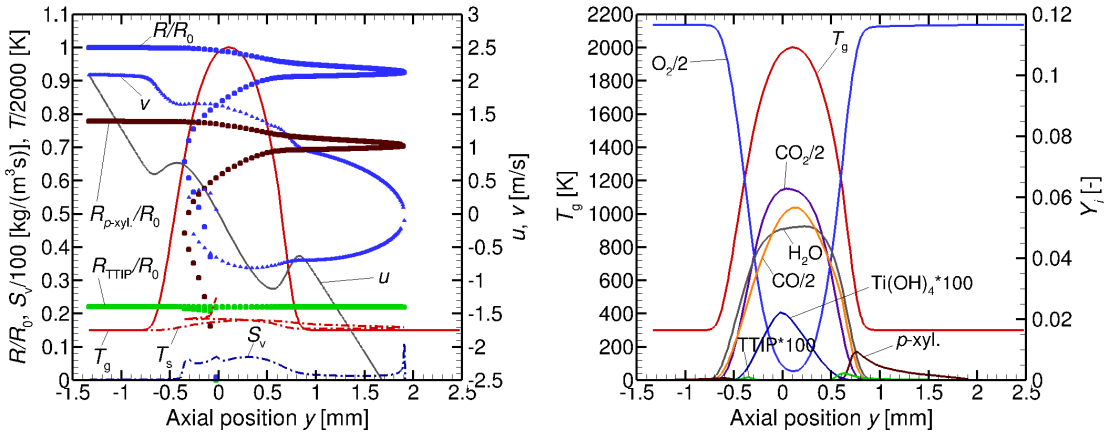

(a) Spray characteristics (b) Outer flame structure

Figure 3.51: Case #7. TTIP/*p*-xylene spray flame structure for $R_0 = 25$ µm, $E_{-\infty} = 0.8$, $T_{l,0} = T_{g,0} = 300$ K, $a_{-\infty} = 1235$/s, $Y_{p\text{-xylene}} = 0.975$, $Y_{TTIP} = 0.025$ [28].

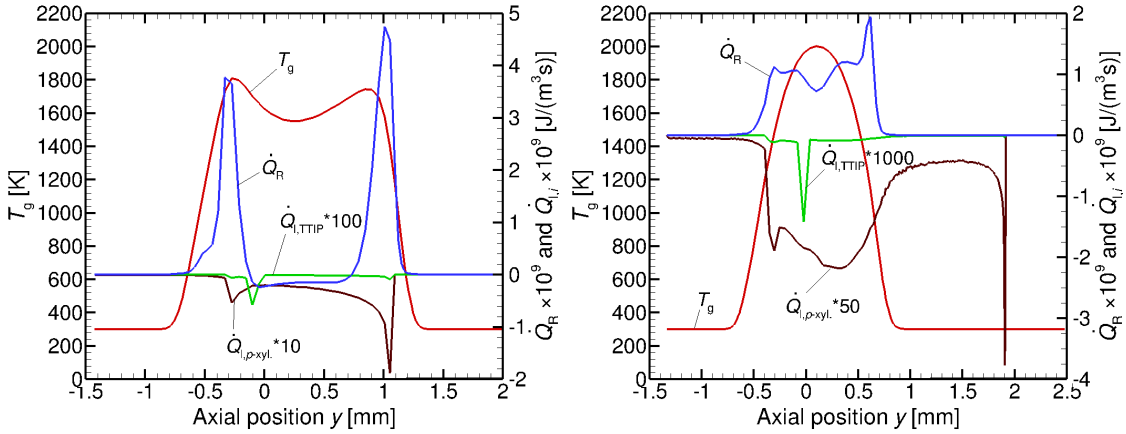

(a) $a_{-\infty} = 1{,}200$/s, case #6 (b) $a_{-\infty} = 1{,}235$/s, case #7

Figure 3.52: TTIP/*p*-xylene spray flame structure for $R_0 = 25$ µm, $E_{-\infty} = 0.8$, $T_{l,0} = T_{g,0} = 300$ K, $Y_{p-\text{xylene}} = 0.975$, $Y_{TTIP} = 0.025$ [28].

is not as pronounced as in cases with larger droplets, yet the thermal decomposition of TTIP still proceeds in this region.

As the gas strain rate increases to 1,235/s, as shown in Figs. 3.51 and 3.52b, the chemical reaction zone significantly narrows, and only a single chemical reaction zone on the spray side of the configuration remains viable; the zone on the gas side fails to sustain itself due to the low gas temperatures observed in Fig. 3.50, and the intense vaporization of the *p*-xylene, as detailed in Fig. 3.52b. Within this remaining chemical reaction zone, the heat release rate is minimized, constrained by the substantial energy demands of the ongoing vaporization processes. From this analysis, it may be concluded that a higher gas strain rate

is less unfavorable to the thermal decomposition process than a high initial droplet radius, even at low strain rates. This observation is based on the analysis of the mass fraction of $Ti(OH)_4$ and the temperature dip values discussed in Fig. 3.49 in the discussion on droplet size, compared with those in Fig. 3.51 in the Subsection 3.3.2.

Mass loadings

Finally, the impact of the initial mass loading of the precursor, TTIP, in the solution is investigated by varying the mass fraction Y_{TTIP}. Initially set at 0.025 in cases illustrated by Figs. 3.45 and 3.46 (case #2), Y_{TTIP} is increased to 0.155 in Fig. 3.53 (case #8) and further to 0.25 in Fig. 3.54 (case #9).

As the mass fraction of the precursor, TTIP is increased, the preferential evaporation of *p*-xylene becomes more pronounced. This alteration in the evaporation dynamics causes the combustion zone to shift toward the spray side of the configuration. This shift is evidenced by the position of the peak of the *p*-xylene vapor moving closer to the spray side. Moreover, the gas temperature within the dip of its profile decreases as the precursor loading is increased, correlating with the location of significant TTIP evaporation. This cooling effect due to enhanced TTIP evaporation retards chemical reactions and thermal decomposition processes, resulting in higher residual mass fractions of both TTIP and *p*-xylene in this region. However, the analysis of Figs. 3.46b, 3.53b, and 3.54b reveals that the peak of the mass fractions of $Ti(OH)_4$ still resides within the chemical reaction zone on the gas side of the configuration. Notably, an increased amount of this species is observed, which is advantageous for the formation of TiO_2 nanoparticles. This observation suggests that while higher precursor loadings can impede some thermal processes due to cooling effects, they

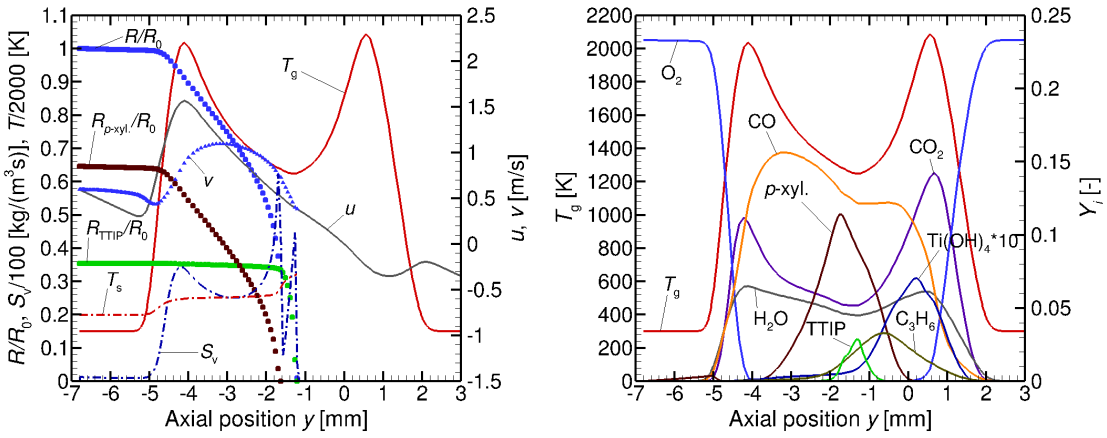

(a) Spray characteristics

(b) Mass fractions

Figure 3.53: Case #8. TTIP/*p*-xylene spray flame structure for $R_0 = 25\,\mu\mathrm{m}$, $E_{-\infty} = 0.8$, $T_{\mathrm{l},0} = T_{\mathrm{g},0} = 300$ K, $a_{-\infty} = 100/\mathrm{s}$, $Y_{p\text{-xylene}} = 0.845$, $Y_{\mathrm{TTIP}} = 0.155$ [28].

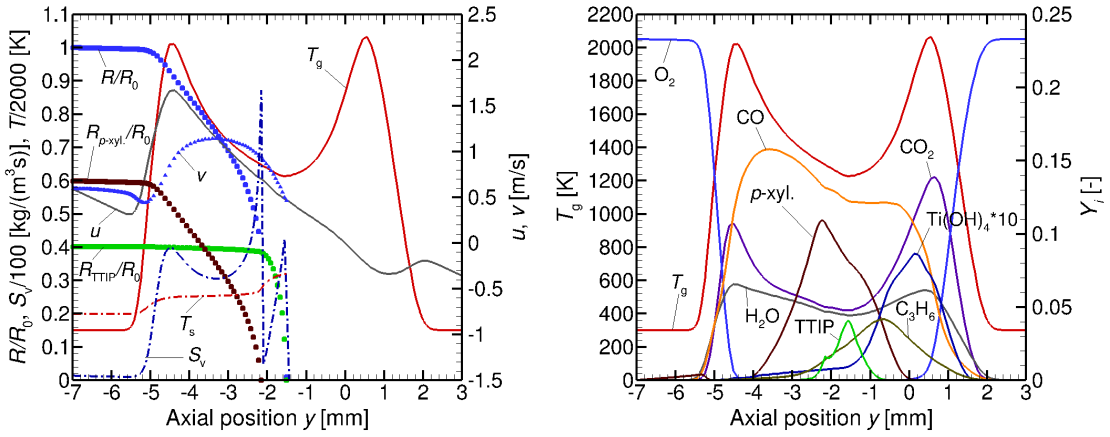

(a) Spray characteristics (b) Mass fractions

Figure 3.54: Case #9. TTIP/*p*-xylene spray flame structure for $R_0 = 25$ µm, $E_{-\infty} = 0.8$, $T_{l,0} = T_{g,0} = 300$ K, $a_{-\infty} = 100$/s, $Y_{p\text{-xylene}} = 0.75$, $Y_{TTIP} = 0.25$ [28].

can also enhance the production of key intermediates necessary for nanoparticle synthesis. Therefore, it is crucial to carefully evaluate and optimize the boundary conditions and precursor mass loading. The goal is to balance these conditions to avoid excessively retarding vaporization while ensuring sufficient precursor presence to achieve optimal yields of nanoparticles. Integrating the formation of nanoparticles into the current model could provide deeper insights into the complex interplay between vaporization dynamics and chemical reactions in this setup. Such an enhancement would allow for a more detailed study of how these factors influence the yield, size, and distribution of TiO_2 nanoparticles, facilitating the development of more efficient and controlled synthesis processes in FSP.

3.3.3 Multiple Spray Flames Structures

As discussed in Subsection 3.2.3, the existence of triple structures within hydrous ethanol laminar spray flames was identified and analyzed under consistent initial and boundary conditions. It was demonstrated that the concentration of a secondary component in the fuel mixture droplet does not influence the transition between multiple flame structures. Similarly, for TTIP/*p*-xylene spray flames configured in counterflow, up to three distinct flame structures were identified under identical conditions, underscoring the complexity of their behavior.

The gas strain rate is proven to be the most critical factor influencing the multiple flame structures in a counterflow spray flame, surpassing the initial droplet radius and equivalence ratio, as discussed in Subsections 3.1.1 and 3.1.2, as well as the mass fraction of components in multicomponent droplet sprays in Subsection 3.2.3. This study, therefore, investigates the

impact of varying strain rates on the multiple flame structures of TTIP/p-xylene spray in a counterflow configuration, with a particular emphasis on the mechanisms driving transitions between these structures. Table 3.2 presents a summary of the various conditions under

Table 3.2: Simulation cases with varying strain rates under the condition: $R_0 = 25\,\mu$m, $E_{-\infty} = 0.8$, $Y_{p\text{-xylene}} = 0.845$, $Y_{\text{TTIP}} = 0.155$.

Case	$a_{-\infty}$ [1/s]	Structure(s) type	Fig. number
10	100	Twopeak/ Gas-sided/ Spray-sided	Fig. 3.55
11	500	Twopeak/ Spray-sided	Fig. 3.56
12	600	Spray-sided	Fig. 3.57

which multiple flame structures are observed. The impact of gas strain rate is considered, other conditions are the same, namely $R_0 = 25\,\mu$m, $E_{-\infty} = 0.8$, $T_{\text{l},0} = T_{\text{g},0} = 300$ K, $Y_{p\text{-xylene}} = 0.845$, $Y_{\text{TTIP}} = 0.155$. As shown in the table, when the strain rate increases, first there are triple flame structures in case #10, followed by double flame structures at 500/s in case #11. When the strain rate increases to 600/s in case #12, the double flame structures merge to the one with only a reaction zone. The following discussion explores the transition mechanisms of these multiple flame structures, accompanied by relevant figures.

The specific flame structures under conditions of case #10 are visualized in Fig. 3.55. The monodisperse spray flame structures characterized by a relatively small initial droplet radius of 25 µm reveal a vaporization zone confined entirely to the spray side of the configuration, with droplets that do not traverse the stagnation plane at the axial position of $y = 0$ mm. The gas temperature profile exhibits a significant decrease just before reaching the stagnation plane, which is simultaneously the location where a peak in the profile of S_{v} is observed. This peak marks the point where all droplets completely evaporate, resulting in substantial energy absorption due to the evaporation process. Furthermore, the profile of the fuel vapor is in alignment with that of S_{v}, indicating the consumption of fuel p-xylene in the hotter regions of the flame. This correlation highlights the dynamic interplay between fuel vaporization and temperature variations within the flame structure, emphasizing the thermal effects induced by spray evaporation in these environments. Both gas and droplet velocities, denoted as u and v respectively, are identical at the spray boundary, highlighting the substantial influence of drag force on the droplets. As the droplets evaporate and reduce in size, their velocities increasingly align with that of the gas, demonstrating the interplay between drag and evaporative dynamics. Additionally, distinct spray flame structures featuring single chemical reaction zones are identified. In Figs. 3.55c and 3.55d, the single reaction zone is positioned on the spray side of the configuration, whereas in Figs. 3.55e and 3.55f,

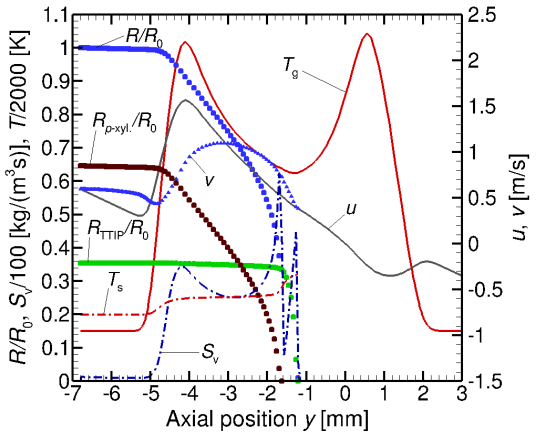

(a) Spray characteristics of twopeak

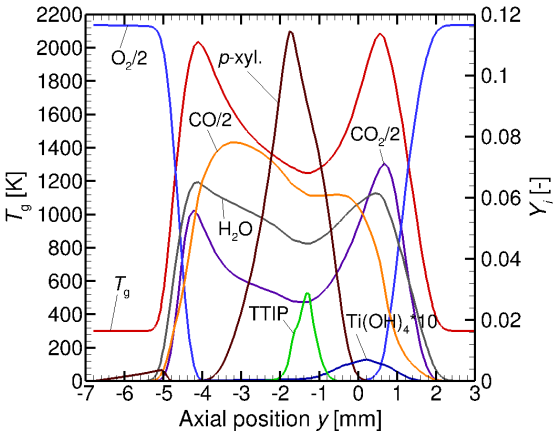

(b) Outer flame structure of twopeak

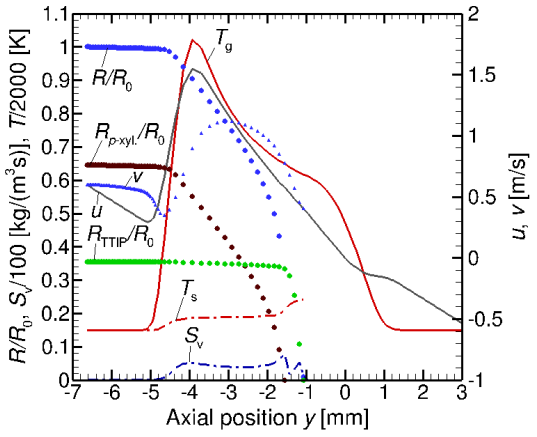

(c) Spray characteristics of spray-sided

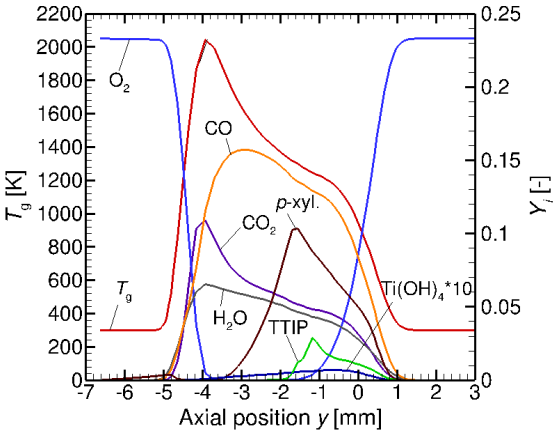

(d) Outer flame structure of spray-sided

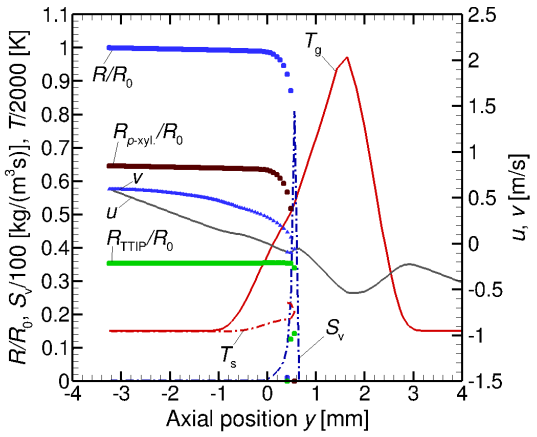

(e) Spray characteristics of gas-sided

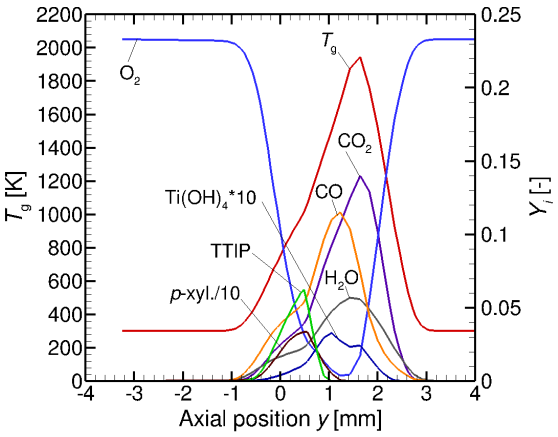

(f) Outer flame structure of gas-sided

Figure 3.55: Case #10. Multiple TTIP/*p*-xylene spray flame structures for $R_0 = 25\,\mu$m, $E_{-\infty} = 0.8$, $T_{l,0} = T_{g,0} = 300$ K, $a_{-\infty} = 100$/s, $Y_{p\text{-xylene}} = 0.845$, $Y_{TTIP} = 0.155$. (a-b) Twopeak; (c-d) spray-sided; (e-f) gas-sided.

it is located on the gas side. This structure, featuring distinct evaporation and combustion zones, demonstrates a close correlation between the combustion and vaporization processes. The evaporation zone sustains combustion by delivering gaseous fuel, while the separated chemical reaction zone supports evaporation through heat release. This interaction may help explain specific characteristics of micro-explosions in precursor solution droplets near liquid fuel injection in FSP, as experimentally identified by Li et al. [108, 172]. A comparative analysis of the spray flame structures shown in Figs. 3.55 reveals that the structures on the spray side closely resemble a twopeak configuration. In contrast, the structures on the gas side are qualitatively different. These observations are in alignment with the discussions presented in Subsection 3.1.2. This alignment underscores the consistency of flame behavior across both monocomponent and multicomponent droplet spray flames, highlighting similar dynamical features despite the variation in spray composition. This comparative analysis thus contributes to a deeper understanding of the behavior and stability of different spray flame structures under varied conditions.

The transition mechanism from three to two different spray flame structures at an initial droplet radius (R_0) of 25 µm is analyzed within the context of Figs. 3.55 and 3.56. Figure 3.56 illustrates the two remaining structures at a strain rate of 500/s, with the structure featuring the gas-sided chemical reaction zone no longer present. As the similar mechanism stated in the Subsection 3.1.2, the strain rate increases, chemical reaction times decrease, leading to chemical extinction, and a comparison of the maximum gas temperatures across different spray flame structures indicates the lowest temperature occurs in the gas-sided chemical reaction zone, highlighting its instability.

Further increasing the gas strain rate to 600/s results in the collapse of the second spray flame structure, leaving only the structure with a spray-sided chemical reaction zone, as depicted in Fig. 3.57. This breakdown is different from what is discussed in Subsection 3.1.1 and 3.1.2, namely the flame structure with two chemical reaction zones mostly stable. This time, only the spray-sided flame structure exists as the other one breaks down due to low gas temperature on the gas side of the configuration resulting in the extinction of the right part flame. Beyond a gas strain rate of 500/s, only the spray flame structure featuring a single chemical reaction zone on the spray side of the counterflow configuration is sustained, as illustrated in Fig. 3.57 for a strain rate of 600/s. While the qualitative outcomes for gas strain rates of 500/s and 600/s are similar, there is a noticeable decrease in the right peak of the spray vaporization rate profile, which subsequently exits the chemical reaction zone, leading to its non-existence at strain rates exceeding 600/s [28]. It is important to note that the disintegration of this spray flame structure is not attributed to chemical extinction, which is common in gas combustion [32], but rather to a failure in the vaporization process [28, 137]. This distinction highlights the critical role of physical processes, such as vaporization, in

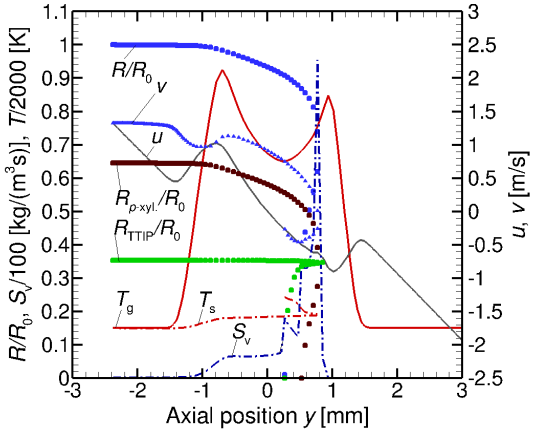

(a) Spray characteristics of twopeak

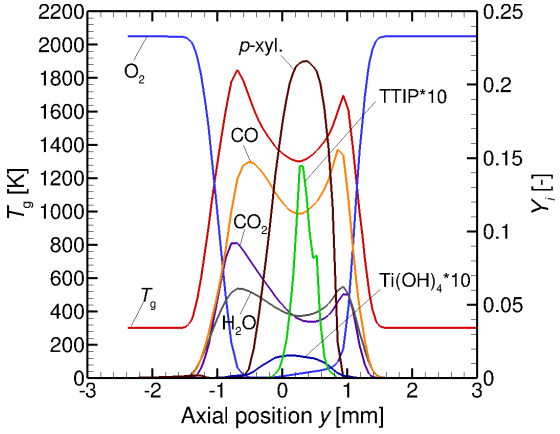

(b) Outer flame structure of twopeak

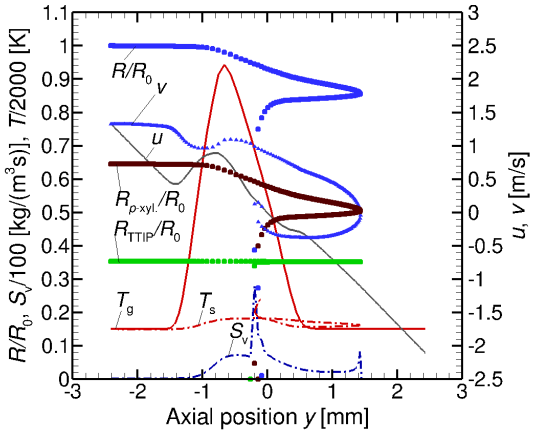

(c) Spray characteristics of spray-sided

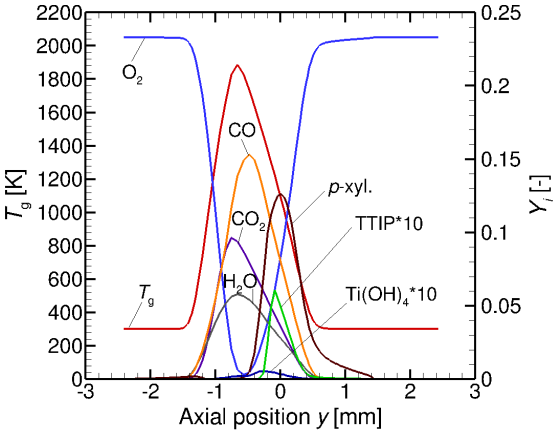

(d) Outer flame structure of spray-sided

Figure 3.56: Case #11. Double TTIP/*p*-xylene spray flame structures for $R_0 = 25\,\mu\text{m}$, $E_{-\infty} = 0.8$, $T_{l,0} = T_{g,0} = 300$ K, $a_{-\infty} = 500/\text{s}$, $Y_{p\text{-xylene}} = 0.845$, $Y_{\text{TTIP}} = 0.155$. (a-b) Twopeak; (c-d) spray-sided.

determining the stability and sustainability of spray flame structures under high strain rate conditions.

As previously analyzed for monocomponent ethanol droplet spray flames in a counterflow configuration in Subsection 3.1.2, the transition in multicomponent precursor solution droplet spray flames to fewer and ultimately singular spray flame structures is driven by the increased momentum of larger droplets. This momentum increase leads to droplet reversal and potential oscillation around the stagnation plane. This dynamic facilitates deeper penetration of the droplets into the chemical reaction zone and towards the gas side of the configuration, thereby enhancing the combustion process by feeding the flame with additional fuel vapor. This interaction illustrates the critical relationship between vaporization and combustion within spray flames: vaporization not only demands energy from the com-

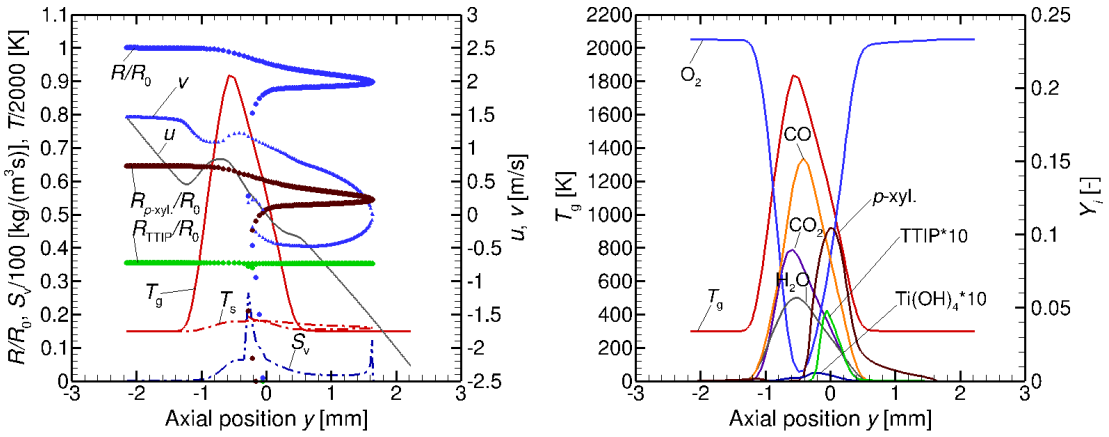

(a) Spray characteristics of spray-sided (b) Outer flame structure of spray-sided

Figure 3.57: Case #12. TTIP/*p*-xylene spray flame structure for $R_0 = 25$ µm, $E_{-\infty}$ = 0.8, $T_{\mathrm{l},0} = T_{\mathrm{g},0}$ = 300 K, $a_{-\infty}$ = 600/s, $Y_{p\text{-xylene}}$ = 0.845, Y_{TTIP} = 0.155. (a-b) Spray-sided.

bustion zone but also supplies fuel vapor to it, while the chemical reactions consume this vapor and generate the necessary energy for further vaporization. Moreover, the motion and positioning of droplets within the counterflow configuration are pivotal in determining the spatial distribution of vaporization and combustion zones. The behavior of droplets, and hence the structure and stability of the spray flames, vary significantly depending on the initial droplet radius in monodisperse sprays. This variation underscores the complex interplay between physical spray properties and combustion dynamics, which governs the transition among different spray flame structures.

4. Summary and Outlook

Spray combustion is integral to numerous energy conversion systems, involving complex interactions among fluid dynamics, heat transfer, chemical kinetics, and phase transitions. Understanding these interactions is essential for enhancing combustion efficiency and reducing pollutant emissions. Laminar flame structures in counterflow configurations are crucial for developing spray flamelet libraries, facilitating the integration of detailed chemical reaction mechanisms into turbulent spray combustion simulations. Therefore, a comprehensive numerical investigation of laminar spray flames was conducted for both monocomponent and multicomponent droplet sprays within a counterflow configuration. Initially, the research employed the Eulerian-Lagrangian framework to analyze monocomponent ethanol spray flames under local fuel-rich conditions. Subsequently, the study extended to multicomponent scenarios of hydrous ethanol spray flames, incorporating the droplet heating and evaporation model by Brenn et al. [116] and a modified gas-liquid phase source term. Furthermore, the study explored precursor solution sprays, TTIP mixed with p-xylene, analyzing the thermal decomposition and resulting combustion characteristics which are significant for applications in FSP. The research illustrated the complex interaction between precusor solution droplet evaporation, chemical kinetics, and flame dynamics. This dissertation aims to advance the foundational understanding of numerical simulations for monocomponent and multicomponent droplet spray flames in the context of the spray flamelet model.

From the results of numerical studies on monocomponent ethanol spray flames under local fuel-rich conditions, multiple laminar fuel-rich spray flame structures within a counterflow configuration are systematically analyzed. These structures are characterized by a single chemical reaction zone on the gas side or double zones on both sides of the configuration. As strain rates increase, they merge into a structure with two reaction zones. Further increases in strain rates result in flame extinction, caused by the breakdown of spray evaporation as droplets exit the reaction zone, rather than by reduced chemical reaction times. The critical role of chemical timescales—specifically those of OH radicals and fuel vapor, which equal at a crossover gas temperature of approximately 1104 K—was identified as essential in the merging of these flame structures. At the highest strain rates, the physical displacement of droplets out of the chemical reaction zone and subsequent temperature drops below

the crossover threshold prevent the maintenance of stable spray flames. This study also uncovered a structure featuring distinct evaporation and combustion zones, demonstrating how evaporation processes support combustion by supplying gaseous fuel, while the heat release from separate chemical reaction zones promotes ongoing evaporation. These findings have significant implications for understanding the dynamics within spray flames, such as the potential for micro-explosions near the point of liquid fuel injection and the occurrence of flame pulsations. Triple flame structures appeared exclusively under conditions of low initial droplet radii ranging from $R_0 = 10\,\mu\text{m}$ to $R_0 = 30\,\mu\text{m}$ and moderate strain rates. In cases of large initial droplet sizes with $R_0 = 50\,\mu\text{m}$, the dynamic momentum of the droplets causes them to bypass the chemical reaction zone, resulting in predominately gas-sided evaporation. The research has advanced the understanding of the transition mechanisms vital for the development or loss of these spray flame structures, highlighting the significant interactions between energy-consuming vaporization processes, droplet positioning within the counterflow setup, and the exothermic nature of the chemical reactions involved. Notably, stable spray flame structures with two reaction zones were observed across all tested scenarios. Furthermore, the impact on spray flamelet modeling from these multiple structures is complex. While the spray-sided zones of double reaction structures resemble those of single-zone configurations, the discovery of a novel single-zone structure with a gas-sided reaction zone necessitates additional consideration for accurate modeling. This study's identification of triple spray flame structures under specific fuel-rich conditions adds a new dimension to the theoretical and practical understanding of spray combustion dynamics, offering a framework for future investigations into optimizing combustion efficiency and reducing emissions in industrial applications.

A detailed numerical analysis of hydrous ethanol laminar spray flames within a counterflow configuration is presented, addressing a significant gap in the current understanding of hydrous ethanol spray combustion. The methodology used for simulating the hydrous ethanol spray flames is carefully outlined, including validation of the computational model employed. The research illustrates the distinctive flame structures observed in hydrous ethanol compared to anhydrous ethanol, with a comprehensive comparison of their characteristics such as flame temperature, mass fractions and chemical reaction rates of critical species, heat release rates, and mass evaporation rates. The findings reveal that hydrous ethanol spray flames demonstrate more rapid droplet evaporation and increased heat release during chemical reactions compared to their anhydrous counterparts. The study also explores the extinction behaviors of both anhydrous and hydrous ethanol spray flames, linking the mechanisms of extinction to the breakdown of spray evaporation. Notably, the hydrous ethanol flames exhibit consistently lower peak temperatures and local minima across all examined strain rates and equivalence ratios, suggesting altered thermal characteristics due to

the presence of water. Furthermore, the investigation identifies multiple flame structures under the same operational conditions for hydrous ethanol sprays. This identification of multiple flame structures under identical conditions underscores the complex interaction of physical and chemical processes in spray combustion, insignificantly influenced by the presence of water in ethanol. These insights are pivotal for advancing the design and optimization of combustion systems that utilize hydrous ethanol, contributing to the broader field of sustainable energy solutions.

A detailed numerical investigation on TTIP/p-xylene spray flames explores the multicomponent heating, evaporation, and motion of the liquid, alongside the thermal decomposition and chemical reactions involved, excluding the actual nanoparticle formation. The extended model, validated for multicomponent droplet spray flames in a counterflow configuration, was utilized. The simulation incorporates the complex thermophysical properties of the bicomponent droplets and encompasses a comprehensive chemical reaction network involving 213 reactions among 52 species, with a particular focus on TTIP's thermal decomposition. A comparative study between a pure p-xylene spray and a TTIP/p-xylene mixture emphasizes the influence of the precursor on evaporation and combustion dynamics. This research identifies that p-xylene, being more volatile, evaporates preferentially, providing the necessary gaseous fuel for sustained combustion. Simultaneously, the thermal decomposition of TTIP occurs in a relatively cooler zone, resulting in a clear separation of reaction zones. The study further observes that larger droplet sizes with $R_0 = 50\,\mu\text{m}$ lead to oscillation and reversal phenomena, creating two distinct reaction zones. In this configuration, the spray-sided zone is responsible for vaporizing the droplets, supported by the energy released from p-xylene combustion, whereas the evaporation of TTIP predominantly happens in the cooler zone, consuming energy critical for its own phase change. The decomposition products of gaseous TTIP, such as C_3H_6 and CH_3, are noted particularly in the gas-sided flame zone. The findings also reveal that smaller initial droplet sizes with $R_0 = 10\,\mu\text{m}$ are advantageous as they reduce the temperature dip associated with larger sizes, enhancing the stability of the combustion process. An increase in the gas strain rate similarly affects the system but has a lesser impact on the formation of $Ti(OH)_4$. Multiple flame structures are identified during the simulations, with the analysis showing that the single reaction zone on the spray side remains the most stable as strain rates increase, differing from the behavior observed in monocomponent ethanol spray flames. This study not only enhances understanding of the underlying physical and chemical mechanisms in FSP processes but also provides valuable insights into optimizing conditions for efficient and stable flame synthesis of advanced materials.

The discovery of new spray flame structures, particularly the coexistence of multiple configurations under identical conditions, offers substantial opportunities for advancing re-

search on both monocomponent and multicomponent droplet spray flames within the framework of the spray flamelet model. To fully understand the implications of these findings on predictive models, an in-depth study focusing on the impact of these structures on spray flamelet modeling is essential. This should include a thorough examination of different extinction mechanisms within the framework of spray flamelet modeling, which may reveal critical insights into the behaviors of these complex flame systems. Looking ahead, a systematic exploration of the multiple structures observed in hydrous ethanol spray flames is crucial. This research will not only delve deeper into the fundamental characteristics of these flames but also explore the transition mechanisms responsible for spray flame instabilities [94]. Such studies are expected to provide valuable insights that could lead to improved control and stability of combustion processes, particularly in industrial applications where efficiency and emission reduction are significant. Additionally, future investigations will expand into the realm of nanoparticle synthesis via FSP. Models incorporating the formation mechanisms of TiO_2 nanoparticles will be developed, focusing on the role of titanium hydroxide $Ti(OH)_4$ as a precursor in the detailed particle model. This approach aims to enhance the understanding of nanoparticle morphology and its dependence on the thermal decomposition pathways of TTIP. Moreover, the application of laminar multicomponent spray flame structures in spray flamelet models of turbulent combustion presents a promising research direction [141]. The impact of the component fraction must be considered in the context of flamelet models for multicomponent spray combustion. This integration could significantly advance the modeling accuracy and predictive capabilities of turbulent combustion processes, potentially leading to breakthroughs in combustion technology and material synthesis.

Bibliography

[1] P. Durand, M. Gorokhovski, and R. Borghi. An application of the probability density function model to diesel engine combustion. *Combustion science and technology*, 144(1-6):47–78, 1999.

[2] R. Mueller, L. Mädler, and S. E. Pratsinis. Nanoparticle synthesis at high production rates by flame spray pyrolysis. *Chemical Engineering Science*, 58(10):1969–1976, 2003.

[3] S. Pokhrel and L. Mädler. Flame-made particles for sensors, catalysis, and energy storage applications. *Energy & Fuels*, 34(11):13209–13224, 2020.

[4] K. Luo, C. Shao, M. Chai, and J. Fan. Level set method for atomization and evaporation simulations. *Progress in Energy and Combustion Science*, 73:65–94, 2019.

[5] A. H. Lefebvre and V. G. McDonell. *Atomization and sprays*. CRC press, 2017.

[6] J. Lasheras, E. Villermaux, and E. Hopfinger. Break-up and atomization of a round water jet by a high-speed annular air jet. *Journal of Fluid Mechanics*, 357:351–379, 1998.

[7] G. Faeth. Evaporation and combustion of sprays. *Progress in Energy and Combustion Science*, 9(1-2):1–76, 1983.

[8] W. A. Sirignano. *Fluid dynamics and transport of droplets and sprays*. Cambridge university press, 2010.

[9] E. Mastorakos. Ignition of turbulent non-premixed flames. *Progress in energy and combustion science*, 35(1):57–97, 2009.

[10] P. Jenny, D. Roekaerts, and N. Beishuizen. Modeling of turbulent dilute spray combustion. *Progress in Energy and Combustion Science*, 38(6):846–887, 2012.

[11] S. Sazhin. *Droplets and sprays*, volume 345. Springer, 2014.

[12] A. L. Sánchez, J. Urzay, and A. Liñán. The role of separation of scales in the description of spray combustion. *Proceedings of the Combustion Institute*, 35(2):1549–1577, 2015.

[13] A. Z. Mendiburu, C. H. Lauermann, T. C. Hayashi, D. J. Mariños, R. B. R. da Costa, C. J. Coronado, J. J. Roberts, and J. A. de Carvalho Jr. Ethanol as a renewable biofuel: Combustion characteristics and application in engines. *Energy*, 257:124688, 2022.

[14] A. Demirbas. Progress and recent trends in biofuels. *Progress in energy and combustion science*, 33(1):1–18, 2007.

[15] A. K. Agarwal. Biofuels (alcohols and biodiesel) applications as fuels for internal combustion engines. *Progress in energy and combustion science*, 33(3):233–271, 2007.

[16] P. S. Nigam and A. Singh. Production of liquid biofuels from renewable resources. *Progress in energy and combustion science*, 37(1):52–68, 2011.

[17] J. M. Bergthorson and M. J. Thomson. A review of the combustion and emissions properties of advanced transportation biofuels and their impact on existing and future engines. *Renewable and sustainable energy reviews*, 42:1393–1417, 2015.

[18] S. Jain and S. Kumar. A comprehensive review of bioethanol production from diverse feedstocks: Current advancements and economic perspectives. *Energy*, 296:131130, 2024.

[19] R. F. Association. Global ethanol production by country or region. `https://afdc.energy.gov/data/10331`. [Online; accessed 16-May-2024].

[20] P. Research. Bioethanol market. `https://www.precedenceresearch.com/bioethanol-market`, 2022. [Online; accessed 16-May-2024].

[21] O. Awogbemi and D. V. Von Kallon. Valorization of agricultural wastes for biofuel applications. *Heliyon*, 8(10), 2022.

[22] R. Lemaire, E. Therssen, and P. Desgroux. Effect of ethanol addition in gasoline and gasoline–surrogate on soot formation in turbulent spray flames. *Fuel*, 89(12): 3952–3959, 2010.

[23] D. Turner, H. Xu, R. F. Cracknell, V. Natarajan, and X. Chen. Combustion performance of bio-ethanol at various blend ratios in a gasoline direct injection engine. *Fuel*, 90(5):1999–2006, 2011.

[24] C. Chevalier. *Entwicklung eines detallierten Reaktionmechanismus zur Modellierung der Verbrennungsprozesse von Kohlenwasserstoffen bei Hoch- und Niedertemperaturbedingungen*. PhD thesis, Universität Stuttgart, 1993.

[25] E. Gutheil. Numerical analysis of the autoignition of methanol, ethanol, n-heptan and n-octane sprays with detailed chemistry. *Combustion Science and Technology*, 105: 265–278, 1995.

[26] E. Gutheil. Structure and extinction of laminar ethanol-air spray flames. *Combustion Theory and Modelling*, 5(2):131–145, 2001.

[27] H. A. Olguín Astudillo. *Theoretical and Numerical Analysis of Laminar Spray Flames for Use in Turbulent Spray Combustion Modeling*. PhD thesis, Heidelberg University, 2015.

[28] Z. Ying, H. Olguin, and E. Gutheil. Multiple structures of laminar fuel-rich spray flames in the counterflow configuration. *Combustion and Flame*, 243:111997, 2022.

[29] Z. Ying and E. Gutheil. Multiple structures and transition mechanisms of laminar fuel-rich ethanol/air counterflowing spray flames. *International Journal of Spray and Combustion Dynamics*, 15(4):197–206, 2023.

[30] O. Awogbemi and D. V. Von Kallon. Recent advances in the application of nanomaterials for improved biodiesel, biogas, biohydrogen, and bioethanol production. *Fuel*, 358:130261, 2024.

[31] N. Peters. Laminar diffusion flamelet models in non-premixed turbulent combustion. *Progress in energy and combustion science*, 10(3):319 – 339, 1984.

[32] N. Peters. *Turbulent Combustion*. Cambridge University Press, 2000.

[33] F. Williams. *Combustion Theory*. Oxford University Press, 1985.

[34] D. Carbonell, C. D. Perez-Segarra, P. Coelho, and A. Oliva. Flamelet mathematical models for non-premixed laminar combustion. *Combustion and Flame*, 156(2):334–347, 2009.

[35] H. Xu, F. Hunger, M. Vascellari, and C. Hasse. A consistent flamelet formulation for a reacting char particle considering curvature effects. *Combustion and flame*, 160 (11):2540–2558, 2013.

[36] H. Barths, C. Hasse, and N. Peters. Computational fluid dynamics modelling of non-premixed combustion in direct injection diesel engines. *International Journal of Engine Research*, 1(3):249–267, 2000.

[37] G. M. Corcos and F. S. Sherman. Vorticity concentration and the dynamics of unstable free shear layers. *Journal of Fluid Mechanics*, 73(2):241–264, 1976.

[38] C. Edwards and R. Rudoff. Structure of a swirl-stabilized spray flame by imaging, laser doppler velocimetry, and phase doppler anemometry. In *Symposium (International) on Combustion*, volume 23, pages 1353–1359. Elsevier, 1991.

[39] I. K. Purl and P. A. Libby. Droplet behavior in counterflowing streams. *Combustion science and technology*, 66(4-6):267–292, 1989.

[40] G. Chen and A. Gomez. Counterflow diffusion flames of quasi-monodisperse electrostatic sprays. In *Symposium (international) on combustion*, volume 24, pages 1531–1539. Elsevier, 1992.

[41] S. Li, P. Libby, and F. Williams. Spray structure in counterflowing streams with and without a flame. *Combustion and flame*, 94(1-2):161–177, 1993.

[42] M. Massot, M. Kumar, M. D. Smooke, and A. Gomez. Spray counterflow diffusion flames of heptane: Experiments and computations with detailed kinetics and transport. In *Symposium (International) on Combustion*, volume 27, pages 1975–1983. Elsevier, 1998.

[43] S. Li and F. Williams. Counterflow heptane flame structure. *Proceedings of the Combustion Institute*, 28(1):1031–1038, 2000.

[44] V. S. Santoro and A. Gomez. Extinction and reignition in counterflow spray diffusion flames interacting with laminar vortices. *Proceedings of the Combustion Institute*, 29 (1):585–592, 2002.

[45] M. Mikami, S. Miyamoto, and N. Kojima. Counterflow diffusion flame with polydisperse sprays. *Proceedings of the Combustion Institute*, 29(1):593–599, 2002.

[46] G. Continillo and W. Sirignano. Counterflow spray combustion modeling. *Combustion and Flame*, 81(3-4):325–340, 1990.

[47] E. Gutheil and W. Sirignano. Counterflow spray combustion modeling with detailed transport and detailed chemistry. *Combustion and Flame*, 113(1-2):92–105, 1998.

[48] D. Schlotz and E. Gutheil. Modeling of laminar mono-and bidisperse liquid oxygen/hydrogen spray flames in the counterflow configuration. *Combustion science and technology*, 158(1):195–210, 2000.

[49] H. Watanabe, R. Kurose, S.-M. Hwang, and F. Akamatsu. Characteristics of flamelets in spray flames formed in a laminar counterflow. *Combustion and Flame*, 148(4): 234–248, 2007.

[50] H. Watanabe, R. Kurose, S. Komori, and H. Pitsch. Effects of radiation on spray flame characteristics and soot formation. *Combustion And Flame*, 152(1-2):2–13, 2008.

[51] R. J. Kee, K. Yamashita, H. Zhu, and A. M. Dean. The effects of liquid-fuel thermophysical properties, carrier-gas composition, and pressure, on strained opposed-flow non-premixed flames. *Combustion and flame*, 158(6):1129–1139, 2011.

[52] J. Hayashi, H. Watanabe, R. Kurose, and F. Akamatsu. Effects of fuel droplet size on soot formation in spray flames formed in a laminar counterflow. *Combustion and Flame*, 158(12):2559–2568, 2011.

[53] H. Zhu, R. J. Kee, L. Chen, J. Cao, M. Xu, and Y. Zhang. Vaporisation characteristics of methanol, ethanol and heptane droplets in opposed stagnation flow at low temperature and pressure. *Combustion Theory and Modelling*, 16(4):715–735, 2012.

[54] C. Wang, A. M. Dean, H. Zhu, and R. J. Kee. The effects of multicomponent fuel droplet evaporation on the kinetics of strained opposed-flow diffusion flames. *Combustion and Flame*, 160(2):265–275, 2013.

[55] H. Olguin and E. Gutheil. Theoretical and numerical study of evaporation effects in spray flamelet modeling. In *Experiments and Numerical Simulations of Turbulent Combustion of Diluted Sprays: TCS 3: Third International Workshop on Turbulent Spray Combustion*, pages 79–106. Springer, 2014.

[56] A. Vié, B. Franzelli, Y. Gao, T. Lu, H. Wang, and M. Ihme. Analysis of segregation and bifurcation in turbulent spray flames: A 3d counterflow configuration. *Proceedings of the Combustion Institute*, 35(2):1675–1683, 2015.

[57] W. Xie, P. B. Govindaraju, Z. Ren, and M. Ihme. Structural analysis and regime diagrams of laminar counterflow spray flames with low-temperature chemistry. *Proceedings of the Combustion Institute*, 38(2):3193–3200, 2021.

[58] Z. Ying and E. Gutheil. Numerical investigation of triple structures of laminar fuel-rich ethanol/air spray flames in the counterflow configuration. In *Proceedings of 16th International Conference on Heat Transfer, Fluid Mechanics and Thermodynamics*, 2022.

[59] Z. Ying and E. Gutheil. Multiple numerical solutions of laminar fuel-rich spray flame structures in the counterflow configuration. In *Proceedings of 31st Conference on Liquid Atomization and Spray Systems, ILASS–Europe*, 2022.

[60] M. Bonanni and M. Ihme. Interaction of preferential evaporation and low-temperature chemistry in multicomponent counterflow spray flames. *Proceedings of the Combustion Institute*, 39(2):2565–2573, 2023.

[61] Z. Ying and E. Gutheil. Numerical simulation of TTIP/*p*-xylene precursor solution spray flames in the counterflow configuration. *Applications in Energy and Combustion Science*, 15:100161, 2023.

[62] Z. Ying and E. Gutheil. Multiple structures and transition mechanisms of laminar fuel-rich ethanol/air counterflowing spray flames. In *Proceedings of 12th Mediterranean Combustion Symposium*, 2023.

[63] Z. Ying and E. Gutheil. Numerical simulation of laminar counterflowing ttip/*p*-xylene spray flames in air. In *Proceedings of 2023 Fall Technical Meeting of the Western States Section of The Combustion Institute*, 2023.

[64] Z. Ying and E. Gutheil. Numerical simulation of laminar precursor solution spray flames in the counterflow configuration. In *Proceedings of 32nd Conference on Liquid Atomization and Spray Systems*, 2023.

[65] S. K. Aggarwal. A review of spray ignition phenomena: present status and future research. *Progress in Energy and Combustion Science*, 24(6):565–600, 1998.

[66] A. J. Marchese, F. L. Dryer, and V. Nayagam. Numerical modeling of isolated n-alkane droplet flames: initial comparisons with ground and space-based microgravity experiments. *Combustion and flame*, 116(3):432–459, 1999.

[67] M. C. Heine and S. E. Pratsinis. Droplet and particle dynamics during flame spray synthesis of nanoparticles. *Industrial & engineering chemistry research*, 44(16): 6222–6232, 2005.

[68] T. Kitano, J. Nishio, R. Kurose, and S. Komori. Evaporation and combustion of multicomponent fuel droplets. *Fuel*, 136:219–225, 2014.

[69] P. B. Govindaraju and M. Ihme. Group contribution method for multicomponent evaporation with application to transportation fuels. *International journal of heat and mass transfer*, 102:833–845, 2016.

[70] A. Stagni, L. Esclapez, P. Govindaraju, A. Cuoci, T. Faravelli, and M. Ihme. The role of preferential evaporation on the ignition of multicomponent fuels in a homogeneous spray/air mixture. *Proceedings of the Combustion Institute*, 36(2):2483–2491, 2017.

[71] P. B. Govindaraju, T. Jaravel, and M. Ihme. Coupling of turbulence on the ignition of multicomponent sprays. *Proceedings of the Combustion Institute*, 37(3):3295–3302, 2019.

[72] V. Shastry, Q. Cazeres, B. Rochette, E. Riber, and B. Cuenot. Numerical study of multicomponent spray flame propagation. *Proceedings of the Combustion Institute*, 38(2):3201–3211, 2021.

[73] X. Wang, J. Gao, Z. Chen, H. Chen, Y. Zhao, Y. Huang, and Z. Chen. Evaluation of hydrous ethanol as a fuel for internal combustion engines: A review. *Renewable energy*, 194:504–525, 2022.

[74] A. Loyte, J. Suryawanshi, G. Bhiogade, Y. Devarajan, and G. Subbiah. Recent developments in utilizing hydrous ethanol for diverse engine technologies. *Chemical Engineering and Processing-Process Intensification*, 177:108985, 2022.

[75] C. A. Cardona and Ó. J. Sánchez. Fuel ethanol production: process design trends and integration opportunities. *Bioresource technology*, 98(12):2415–2457, 2007.

[76] B. Abdollahipoor, S. A. Shirazi, K. F. Reardon, and B. C. Windom. Near-azeotropic volatility behavior of hydrous and anhydrous ethanol gasoline mixtures and impact on droplet evaporation dynamics. *Fuel processing technology*, 181:166–174, 2018.

[77] B. Gainey, Z. Yan, J. Gohn, M. R. Boldaji, and B. Lawler. Tsci with wet ethanol: an investigation of the effects of injection strategy on a diesel engine architecture. Technical report, SAE Technical Paper, 2019.

[78] R. Munsin, Y. Laoonual, S. Jugjai, and Y. Imai. An experimental study on performance and emissions of a small si engine generator set fuelled by hydrous ethanol with high water contents up to 40%. *Fuel*, 106:586–592, 2013.

[79] W. Ambrós, T. Lanzanova, J. Fagundez, R. Sari, D. Pinheiro, M. Martins, and N. Salau. Experimental analysis and modeling of internal combustion engine operating with wet ethanol. *Fuel*, 158:270–278, 2015.

[80] J. Fagundez, R. Sari, M. Martins, and N. Salau. Comparative analysis of different heat transfer correlations in a two-zone combustion model applied on a SI engine fueled with wet ethanol. *Applied Thermal Engineering*, 115:22–32, 2017.

[81] A. A. Martins, R. A. D. Rocha, and J. R. Sodré. Cold start and full cycle emissions from a flexible fuel vehicle operating with natural gas, ethanol and gasoline. *Journal of Natural Gas Science and Engineering*, 17:94–98, 2014.

[82] M. M. Koupaie, A. Cairns, H. Vafamehr, and T. D. M. Lanzanova. A study of hydrous ethanol combustion in an optical central direct injection spark ignition engine. *Applied Energy*, 237:258–269, 2019.

[83] I. Schifter, L. Diaz, J. Gómez, and U. Gonzalez. Combustion characterization in a single cylinder engine with mid-level hydrated ethanol–gasoline blended fuels. *Fuel*, 103:292–298, 2013.

[84] X. Deng, Z. Chen, X. Wang, H. Zhen, and R. Xie. Exhaust noise, performance and emission characteristics of spark ignition engine fuelled with pure gasoline and hydrous ethanol gasoline blends. *Case Studies in Thermal Engineering*, 12:55–63, 2018.

[85] T. Venugopal, A. Sharma, S. Satapathy, A. Ramesh, and M. Gajendra Babu. Experimental study of hydrous ethanol gasoline blend (E10) in a four stroke port fuel-injected spark ignition engine. *International Journal of Energy Research*, 37(6):638–644, 2013.

[86] A. B. Dempsey, B. Das Adhikary, S. Viswanathan, and R. D. Reitz. Reactivity controlled compression ignition using premixed hydrated ethanol and direct injection diesel. *The Journal of Engineering for Gas Turbines and Power*, 134:1–11, 2012.

[87] M. R. Boldaji, B. Gainey, P. O'Donnell, J. Gohn, and B. Lawler. Investigating the effect of spray included angle on thermally stratified compression ignition with wet ethanol using computational fluid dynamics. *Applied Thermal Engineering*, 170: 114964, 2020.

[88] P. C. O'Donnell, M. R. Boldaji, B. Gainey, and B. Lawler. Varying intake stroke injection timing of wet ethanol in LTC. Technical report, SAE Technical Paper, 2020.

[89] J. Liang, G. Li, Z. Zhang, Z. Xiong, F. Dong, and R. Yang. Experimental and numerical studies on laminar premixed flames of ethanol–water–air mixtures. *Energy Fuels*, 28(7):4754–4761, 2014.

[90] L. van Treek, M. L. Lavadera, L. Seidel, F. Mauss, and A. A. Konnov. Experimental and modelling study of laminar burning velocity of aqueous ethanol. *Fuel*, 257: 116069, 2019.

[91] C. Xu, W. Liu, C. Xie, L. Wei, Y. Li, C. Gong, C. Xu, and C. Wang. Accelerating laminar flame speed of hydrous ethanol via oxygen-rich combustion. *BioEnergy Research*, 14:634–644, 2021.

[92] F. L. Sacomano Filho, A. C. Santos, A. Vié, J. A. van Oijen, et al. Impact of multicomponent description of hydrophilic fuel droplets in propagating spray flames. *Combustion and Flame*, 263:113415, 2024.

[93] K. M. Rahman, N. Kawahara, K. Tsuboi, and E. Tomita. Combustion characteristics of wet ethanol ignited using a focused Q-switched Nd: YAG nanosecond laser. *Fuel*, 165:331–340, 2016.

[94] L. F. M. G. Lama, L. Pizzuti, J. Sotton, and C. A. Martins. Experimental investigation of hydrous ethanol/air flame front instabilities at elevated temperature and pressures. *Fuel*, 287:119555, 2021.

[95] F. Schneider, S. Suleiman, J. Menser, E. Borukhovich, I. Wlokas, A. Kempf, H. Wiggers, and C. Schulz. SpraySyn—a standardized burner configuration for nanoparticle synthesis in spray flames. *Review of Scientific Instruments*, 90(8):085108, 2019.

[96] W.-N. Wang, I. W. Lenggoro, Y. Terashi, T. O. Kim, and K. Okuyama. One-step synthesis of titanium oxide nanoparticles by spray pyrolysis of organic precursors. *Materials Science and Engineering: B*, 123(3):194–202, 2005.

[97] H. Teisala, M. Tuominen, M. Aromaa, J. M. Mäkelä, M. Stepien, J. Saarinen, M. Toivakka, and J. Kuusipalo. Development of superhydrophobic coating on paperboard surface using the liquid flame spray. *Surface and Coatings Technology*, 205(2):436–445, 2010.

[98] C. Weise, J. Menser, S. Kaiser, A. Kempf, and I. Wlokas. Numerical investigation of the process steps in a spray flame reactor for nanoparticle synthesis. *Proceedings of the Combustion Institute*, 35(2):2259–2266, 2015.

[99] M. Y. Manuputty, J. A. Dreyer, Y. Sheng, E. J. Bringley, M. L. Botero, J. Akroyd, and M. Kraft. Polymorphism of nanocrystalline TiO_2 prepared in a stagnation flame: formation of the TiO_2 – II phase. *Chemical science*, 10(5):1342–1350, 2019.

[100] M. Y. Manuputty, C. S. Lindberg, M. L. Botero, J. Akroyd, and M. Kraft. Detailed characterisation of TiO_2 nano-aggregate morphology using tem image analysis. *Journal of Aerosol Science*, 133:96–112, 2019.

[101] J. G. Hill, K. B. Sharpless, C. M. Exon, and R. Regenye. Enantioselective epoxidation of allylic alcohols:(2S, 3S)-3-propyloxiranemethanol. *Organic Syntheses*, 63:66–66, 2003.

[102] D. Bradley, R. C. Mehrotra, I. Rothwell, and A. Singh. *Alkoxo and aryloxo derivatives of metals*. Elsevier, 2001.

[103] H. Chang, S. J. Kim, H. D. Jang, and J. W. Choi. Synthetic routes for titania nanoparticles in the flame spray pyrolysis. *Colloids and Surfaces A: Physicochemical and Engineering Aspects*, 313:282–287, 2008.

[104] M. Gonchikzhapov and T. Kasper. Decomposition reactions of $Fe(CO)_5$, $Fe(C_5H_5)_2$, and TTIP as precursors for the spray-flame synthesis of nanoparticles in partial spray evaporation at low temperatures. *Industrial & Engineering Chemistry Research*, 59 (18):8551–8561, 2020.

[105] L. G. Bettini, M. V. Dozzi, F. Della Foglia, G. L. Chiarello, E. Selli, C. Lenardi, P. Piseri, and P. Milani. Mixed-phase nanocrystalline TiO_2 photocatalysts produced by flame spray pyrolysis. *Applied Catalysis B: Environmental*, 178:226–232, 2015.

[106] A. Abdelsamie, F. E. Kruis, H. Wiggers, and D. Thévenin. Nanoparticle formation and behavior in turbulent spray flames investigated by DNS. *Flow, Turbulence and Combustion*, 105:497–516, 2020.

[107] A. Abdelsamie, H. Wiggers, F. E. Kruis, and D. Thévenin. Direct numerical simulation of spraysyn burner: Impact of liquid solvent. *International Journal of Spray and Combustion Dynamics*, 15(4):237–247, 2023.

[108] H. Li, C. D. Rosebrock, N. Riefler, T. Wriedt, and L. Mädler. Experimental investigation on microexplosion of single isolated burning droplets containing titanium tetraisopropoxide for nanoparticle production. *Proceedings of the Combustion Institute*, 36(1):1011–1018, 2017.

[109] H. Torabmostaedi and T. Zhang. Numerical simulation of TiO_2 nanoparticle synthesis by flame spray pyrolysis. *Powder Technology*, 329:426–433, 2018.

[110] A. Keller, I. Wlokas, M. Kohns, and H. Hasse. Thermophysical properties of mixtures of titanium (IV) isopropoxide (TTIP) and *p*-Xylene. *Journal of Chemical & Engineering Data*, 65(2):869–876, 2020.

[111] P. Narasu, M. Nanjaiah, I. Wlokas, and E. Gutheil. Numerical simulation and parameterization of the heating and evaporation of a titanium (IV) isopropoxide/*p*-xylene

precursor/solvent droplet in hot convective air. *International Journal of Multiphase Flow*, 150:104006, 2022.

[112] P. Narasu and E. Gutheil. A new model for puffing and micro-explosion of single titanium(IV) isopropoxide/*p*-xylene precursor solution droplets. *International Journal of Heat and Mass Transfer*, 202:123647, 2023.

[113] B. Kunstmann, I. Wlokas, M. Kohns, and H. Hasse. Simulation study of superheating in evaporating droplets of (TTIP+ *p*-xylene) in spray flame synthesis. *Applications in Energy and Combustion Science*, 15:100156, 2023.

[114] C. S. Lindberg, M. Y. Manuputty, P. Buerger, J. Akroyd, and M. Kraft. Numerical simulation and parametric sensitivity study of titanium dioxide particles synthesised in a stagnation flame. *Journal of Aerosol Science*, 138:105451, 2019.

[115] C. S. Lindberg, M. Y. Manuputty, J. Akroyd, and M. Kraft. A two-step simulation methodology for modelling stagnation flame synthesised aggregate nanoparticles. *Combustion and Flame*, 202:143–153, 2019.

[116] G. Brenn, L. Deviprasath, F. Durst, and C. Fink. Evaporation of acoustically levitated multi-component liquid droplets. *International journal of heat and mass transfer*, 50 (25-26):5073–5086, 2007.

[117] T. Poinsot and D. Veynante. *Theoretical and Numerical Combustion, Second Edition*. R.T. Edwards, Inc., 2005.

[118] H. Pitsch and N. Peters. A consistent flamelet formulation for non-premixed combustion considering differential diffusion effects. *Combustion and Flame*, 114(1–2): 26 – 40, 1998.

[119] E. Knudsen and H. Pitsch. A general flamelet transformation useful for distinguishing between premixed and non-premixed modes of combustion. *Combustion and Flame*, 156(3):678 – 696, 2009.

[120] A. Scholtissek, S. Popp, S. Hartl, H. Olguin, P. Domingo, L. Vervisch, and C. Hasse. Derivation and analysis of two-dimensional composition space equations for multi-regime combustion using orthogonal coordinates. *Combustion and Flame*, 218:205 – 217, 2020.

[121] J. van Oijen, A. Donini, R. Bastiaans, J. ten Thije Boonkkamp, and L. de Goey. State-of-the-art in premixed combustion modeling using flamelet generated manifolds. *Progress in Energy and Combustion Science*, 57:30 – 74, 2016.

[122] G. Lodier, L. Vervisch, V. Moureau, and P. Domingo. Composition-space premixed flamelet solution with differential diffusion for in situ flamelet-generated manifolds. *Combustion and Flame*, 158(10):2009 – 2016, 2011.

[123] A. Scholtissek, P. Domingo, L. Vervisch, and C. Hasse. A self-contained progress variable space solution method for thermochemical variables and flame speed in freely-propagating premixed flamelets. *Proceedings of the Combustion Institute*, 37 (2):1529–1536, 2019.

[124] M. E. Mueller. Physically-derived reduced-order manifold-based modeling for multi-modal turbulent combustion. *Combustion and Flame*, 214:287–305, 2020.

[125] C. Hollmann and E. Gutheil. Modeling of turbulent spray diffusion flames including detailed chemistry. 26(1):1731–1738, 1996.

[126] C. Hollmann and E. Gutheil. Diffusion flames based on a laminar spray flame library. *Combustion science and technology*, 135(1-6):175–192, 1998.

[127] H.-W. Ge and E. Gutheil. Probability density function (PDF) simulation of turbulent spray flows. *Atomization and sprays*, 16(5), 2006.

[128] H.-W. Ge and E. Gutheil. Simulation of a turbulent spray flame using coupled PDF gas phase and spray flamelet modeling. *Combustion and Flame*, 153(1):173 – 185, 2008.

[129] H.-W. Ge, I. Düwel, H. Kronemayer, R. Dibble, E. Gutheil, C. Schulz, and J. Wolfrum. Laser-based experimental and monte carlo PDF numerical investigation of an ethanol/air spray flame. *Combustion science and technology*, 180(8):1529–1547, 2008.

[130] Y. Hu and E. Gutheil. Numerical simulations of turbulent poly-disperse acetone spray flows using a transported joint probability density function method. *Atomization and Sprays*, 26(3):275–299, 2016.

[131] Y. Hu, H. Olguin, and E. Gutheil. Transported joint probability density function simulation of turbulent spray flames combined with a spray flamelet model using a transported scalar dissipation rate. *Combustion Science and Technology*, 189(2): 322–339, 2017.

[132] Y. Hu, H. Olguin, and E. Gutheil. A spray flamelet/progress variable approach combined with a transported joint PDF model for turbulent spray flames. *Combustion Theory and Modelling*, 21(3):575–602, 2017.

[133] H. Olguin and E. Gutheil. Influence of evaporation on spray flamelet structures. *Combustion and Flame*, 161(4):987 – 996, 2014.

[134] H. Olguin and E. Gutheil. Derivation and evaluation of a multi-regime spray flamelet model. *Zeitschrift für Physikalische Chemie*, 229(4):461–482, 2015.

[135] H. Olguin, A. Scholtissek, S. Gonzalez, F. Gonzalez, M. Ihme, C. Hasse, and E. Gutheil. Closure of the scalar dissipation rate in the spray flamelet equations through a transport equation for the gradient of the mixture fraction. *Combustion and Flame*, 208:330–350, 2019.

[136] E. Gutheil. Multiple solutions for structures of laminar counterflow spray flames. *Progress in Computational Fluid Dynamics, an International Journal*, 5(7):414–419, 2005.

[137] J. Carpio, D. Martínez-Ruiz, A. Liñán, A. L. Sánchez, and F. A. Williams. Hysteresis in the vaporization-controlled inertial regime of nonpremixed counterflow spray combustion. *Combustion Science and Technology*, 192(3):433–456, 2019.

[138] W. Xie, P. B. Govindaraju, Z. Ren, and M. Ihme. Structural analysis and regime diagrams of laminar counterflow spray flames with low-temperature chemistry. *Proceedings of the Combustion Institute*, 38(2):3193–3200, 2021.

[139] Q. Hu and L. Wang. Structure and similarity properties of the laminar counterflow spray flame. *Combustion Theory and Modelling*, 27(6):768–786, 2023.

[140] X. Zhang, R. Yi, and C. P. Chen. Development of a multiphase flamelet generated manifold for spray combustion simulations. *Journal of Engineering for Gas Turbines and Power*, 143(6):061009, 2021.

[141] R. Yi and C. Chen. Spray flamelet modeling of turbulent two-phase reacting flows with multi-component fuel in a lean direct injection combustor. *Combustion Science and Technology*, pages 1–43, 2023.

[142] N. M. Marinov. A detailed chemical kinetic model for high temperature ethanol oxidation. *International journal of chemical kinetics*, 31(3):183–220, 1999.

[143] C. Olm, T. Varga, É. Valkó, S. Hartl, C. Hasse, and T. Turányi. Development of an ethanol combustion mechanism based on a hierarchical optimization approach. *International Journal of Chemical Kinetics*, 48(8):423–441, 2016.

[144] F. L. Sacomano Filho, A. C. Santos, A. Vié, and G. C. Krieger Filho. A new robust modeling strategy for multi-component droplet heat and mass transfer in general

ambient conditions. *International Journal of Heat and Mass Transfer*, 194:123102, 2022.

[145] P. Narasu. *Numerical Simulation of the Heating, Evaporation, Thermal Decomposition, Puffing, and Micro-Explosion of Single Alcohol/Water and Precursor/Solvent Droplets for Nanoparticle Synthesis in Spray Flames*. PhD thesis, Heidelberg University, 2022.

[146] H. Torabmostaedi, T. Zhang, P. Foot, S. Dembele, and C. Fernandez. Process control for the synthesis of ZrO_2 nanoparticles using FSP at high production rate. *Powder technology*, 246:419–433, 2013.

[147] H. Torabmostaedi and T. Zhang. Effect of nozzle geometry and processing parameters on the formation of nanoparticles using FSP. *Chemical Engineering Research and Design*, 92(11):2470–2478, 2014.

[148] Y. Ren, J. Cai, and H. Pitsch. Theoretical single-droplet model for particle formation in flame spray pyrolysis. *Energy & Fuels*, 35(2):1750–1759, 2021.

[149] A. Abdelsamie, C. Chi, M. Nanjaiah, I. Skenderović, S. Suleiman, and D. Thévenin. Direct numerical simulation of turbulent spray combustion in the spraysyn burner: impact of injector geometry. *Flow, Turbulence and Combustion*, 106:453–469, 2021.

[150] S.-J. Baik, P. Wollny, M. Nanjaiah, I. Wlokas, and A. Kempf. Large eddy simulation of iron (iii) oxide nanoparticle synthesis in spray flames. *Applications in Energy and Combustion Science*, 15:100185, 2023.

[151] B. Franzelli, A. Vié, M. Boileau, B. Fiorina, and N. Darabiha. Large eddy simulation of swirled spray flame using detailed and tabulated chemical descriptions. *Flow, Turbulence and Combustion*, 98:633–661, 2017.

[152] F. L. Sacomano Filho, A. Hosseinzadeh, A. Sadiki, and J. Janicka. On the interaction between turbulence and ethanol spray combustion using a dynamic wrinkling model coupled with tabulated chemistry. *Combustion and Flame*, 215:203–220, 2020.

[153] R. J. Kee, J. Warnatz, and J. A. Miller. A FORTRAN computer code package for the evaluation of gas phase viscosities, heat conductivities, and diffusion coefficients. Technical report, Sandia National Laboratories, Livermore, 1983. Sandia Report SAND83-8209.

[154] S. Gordon. *Computer program for calculation of complex chemical equilibrium compositions, rocket performance, incident and reflected shocks, and Chapman-Jouguet*

detonations, volume 273. Scientific and Technical Information Office, National Aeronautics and Space Administration, 1976.

[155] T. Poinsot and D. Veynante. *Theoretical and numerical combustion*. RT Edwards, Inc., 2005.

[156] A. Fick. On liquid diffusion. *The London, Edinburgh, and Dublin Philosophical Magazine and Journal of Science*, 10(63):30–39, 1855.

[157] B. Abramzon and W. Sirignano. Droplet vaporization model for spray combustion calculations. *International Journal of Heat and Mass Transfer*, 32(9):1605–1618, 1989.

[158] O. Noreña and E. Gutheil. Structures of ethanol spray flames under CO_2 dilution of the oxidizer in the counterflow configuration under mild combustion conditions. *Fluids*, 5(4):194, 2020.

[159] P. Narasu, S. Boschmann, P. Pöschko, F. Zhao, and E. Gutheil. Modeling and simulation of single ethanol/water droplet evaporation in dry and humid air. *Combustion Science and Technology*, 192(7):1233–1252, 2020.

[160] B. Poling, J. Prausnitz, and J. O'Connel. *The properties of gases and liquids, Fifth Edition*. McGraw-Hill, New York, 2001.

[161] M. Kleiber and R. Joh. D1 berechnungsmethoden für thermophysikalische stoffeigenschaften. *VDI-Wärmeatlas: Fachlicher Träger VDI-Gesellschaft Verfahrenstechnik und Chemieingenieurwesen*, pages 157–200, 2019.

[162] M. Nanjaiah and I. Wlokas. Personal communication, 2022.

[163] E. Ranzi, A. Frassoldati, R. Grana, A. Cuoci, T. Faravelli, A. Kelley, and C. Law. Hierarchical and comparative kinetic modeling of laminar flame speeds of hydrocarbon and oxygenated fuels. *Progress in Energy and Combustion Science*, 38(4):468–501, 2012.

[164] C. Ji, E. Dames, Y. Wang, H. Wang, and F. Egolfopoulos. Propagation and extinction of premixed C_5–C_{12} n-alkane flames. *Combustion and Flame*, 157:277–87, 2010.

[165] P. Buerger, D. Nurkowski, J. Akroyd, and M. Kraft. A kinetic mechanism for the thermal decomposition of titanium tetraisopropoxide. *Proceedings of the Combustion Institute*, 36(1):1019–1027, 2017.

[166] E. N. Fuller, P. D. Schettler, and J. C. Giddings. New method for prediction of binary gas-phase diffusion coefficients. *Industrial & Engineering Chemistry*, 58(5):18–27, 1966.

[167] W. M. Haynes, D. R. Lide, and T. J. Bruno. *CRC Handbook of Chemistry and Physics*. CRC press, 2016.

[168] E. D. Nikitin, A. P. Popov, Y. G. Yatluk, and V. A. Simakina. Critical properties of some tetraalkoxysilanes and tetraalkoxytitaniums with branched alkyl radicals. *Fluid Phase Equilibria*, 331:1–5, 2012.

[169] NIST Chemistry WebBook. `https://webbook.nist.gov/chemistry/name-ser/`, 2021.

[170] H. K. Versteeg. *An introduction to computational fluid dynamics the finite volume method, 2/E*. Pearson Education India, 2007.

[171] S. Karaminejad, S. M. Dupont, M. Bieber, M. A. Reddemann, R. Kneer, T. Dreier, T. Endres, and C. Schulz. Characterization of spray parameters and flame stability in two modified nozzle configurations of the spraysyn burner. *Proceedings of the Combustion Institute*, 39(2):2673–2682, 2023.

[172] H. Li, C. D. Rosebrock, Y. Wu, T. Wriedt, and L. Mädler. Single droplet combustion of precursor/solvent solutions for nanoparticle production: Optical diagnostics on single isolated burning droplets with micro-explosions. *Proceedings of the Combustion Institute*, 37(1):1203–1211, 2019.

[173] J. Greenberg and R. Cohen. Dynamics of a pulsating spray-diffusion flame. *Journal of engineering mathematics*, 31:397–409, 1997.

[174] L. Ma, Y. Chou, X. Cui, and Z. Zheng. Research on double-component droplets evaporation properties. *Industrial Heating*, 43(1):13–16, 2014.

[175] L. Qiu, Y. Zheng, Y. Hua, Y. Zhuang, Y. Qian, and X. Cheng. Effects of water vapor addition on the flame structure and soot formation in a laminar ethanol/air coflow flame. *Combustion Science and Technology*, 193(4):626–642, 2021.

[176] J. Greenberg and N. Sarig. An analysis of multiple flames in counterflow spray combustion. *Combustion and Flame*, 104(4):431 – 459, 1996.

[177] C. Xu, S. Wu, Y. Li, S. Chu, and C. Wang. Explosion characteristics of hydrous bio-ethanol in oxygen-enriched air. *Fuel*, 271:117604, 2020.

[178] A. Liñán, D. Martinez-Ruiz, A. L. Sánchez, and J. Urzay. Regimes of spray vaporization and combustion in counterflow configurations. *Combustion Science and Technology*, 187(1-2):103–131, 2015.

Abbreviations and Symbols

Abbreviation	Meaning
CFD	computational fluid dynamics
FSP	flame spray pyrolysis
Gas-sided	a chemical reaction zone on the gas side of the configuration
H_2O	water
ICE	internal combustion engines
LSE	large eddy simulations
NOx	nitrogen oxides
p-xyl.	*p*-xylene
RCCI	reactivity controlled compression ignition
Spray-sided	a chemical reaction zone on the spray side of the configuration
TDMA	Tri-Diagonal Matrix Algorithm
TiO_2	titanium dioxide
$Ti(OH)_4$	titanium hydroxide
TTIP	titanium(IV) isopropoxide
Twopeak	two chemical reaction zones on both sides of the configuration
UNIFAC	universal quasichemical functional group activity coefficients
USD	United States dollar
VLE	vapor liquid equilibrium
vol%	volume fraction

Variables	**Unit**	**Meaning**
a	[s^{-1}]	gas strain rate
A	[-]	pre-exponential factor
B_M	[-]	Spalding mass transfer number
B_T	[-]	Spalding heat transfer number
C	[-]	concentration
c_p	[J $kg^{-1}K^{-1}$)]	specific heat capacity
C_p	[J K^{-1})]	heat capacity
D	[m^2 s^{-1}]	diffusivity
E	[kJ mol^{-1}]	activation energy
$E_{-\infty}$	[-]	equivalence ratio
f	[kg $m^{-2}s^{-1}$]	stream function
g	[m s^{-2}]	gravity acceleration
h	[J]	enthalpy
k	[-]	number of different droplet size groups
L	[J kg^{-1}]	latent heat of vaporization
Le	[-]	Lewis Number
m	[kg]	droplet mass
$\dot{m}$	[kg s^{-1}]	mass evaporation rate
M	[kg mol^{-1}]	molar mass
M	[-]	total reaction number
$\bar{M}$	[Da]	mean molecular weight of the gas
n	[m^{-3}]	droplet number density
N	[-]	total species number
Nu	[-]	Nusselt number
$\widetilde{\text{Nu}}$	[-]	modified Nusselt number
p	[N m^{-2}]	pressure
Pr	[-]	Prandtl number
Q	[J]	heat transfer

Variables	**Unit**	**Meaning**
$\dot{q}$	[J m^{-2}s]	energy flux into the droplet interior
r	[m]	radial coordinate
R	[J mol^{-1}K^{-1}]	universal gas constant
R	[m]	droplet radius
Re	[-]	Reynolds number
S	[-]	source term
Sc	[-]	Schmidt number
Sh	[-]	Sherwood number
$\widetilde{\text{Sh}}$	[-]	modified Sherwood number
t	[s]	time
T	[K]	temperature
u	[m s^{-1}]	velocity component in x direction
v	[m s^{-1}]	velocity component in y direction
V	[m s^{-1}]	diffusion velocity
$\bar{W}$	[Da]	mean molecular weight of the mixture
$\dot{w}$	[mol m^{-3}s^{-1}]	molar chemical reaction rate
x	[m]	coordinate in x direction
X	[-]	mole fraction
y	[m]	coordinate in y direction
Y	[-]	mass fraction
z	[-]	fictive variable

Greek symbols	**Unit**	**Meaning**
α	[-]	0 or 1 for the planar or axisymmetric counterflow
β	[-]	constant in Arrhenius equation
δ	[-]	Kronecker delta
η	[kg m^{-2}]	similarity variable
μ	[kg m^{-1}s^{-1}]	dynamic viscosity
ν'_{kj}, ν''_{kj}	[-]	molar stoichiometric coefficients of species k in reaction j
θ	[-]	non-dimensional temperature
λ	[W m^{-1}K^{-1}]	thermal conductivity
ρ	[kg m^{-3}]	density
ξ	[-]	transformed radial coordinate
τ	[-]	transformed time coordinate, viscous stress

Subscript	**Meaning**
atm	atmospheric
e	energy source term
evap	evaporation
f	film
F	fuel
i	component, i direction
j	j direction, reaction number
k	species number, droplet group
l	liquid
m	momentum source term
M	mass transfer
p	pressure
s	surface
sp	spray
st	stoichiometric
T	heat transfer
v	mass source term
V	vaporization
vap	vapor
$-\infty$	conditions at the spray inlet
∞	conditions at the gas inlet
0	initial value

Superscript	Meaning
$'$	derivative
$''$	second derivative
*	reference value

Acknowledgements

The research work presented in this dissertation was primarily conducted at the Interdisciplinary Center for Scientific Computing (IWR) at Heidelberg University, under the supervision of Prof. Dr. Eva Gutheil, from 01/11/2020 to 31/10/2023. This study was supported by funding from the German Research Foundation (DFG) through the priority program SPP 1980, grant GU 255/13-2, and HGS-MathComp.

First and foremost, I would like to express my great gratitude to Prof. Dr. Eva Gutheil, head of the research group of Multiphase Flows and Combustion at Heidelberg University. Then, I also extend my sincere thanks to my colleagues, Dr. Maximilian Herrmann, Dr. Praveen Narasu, Chandra Singh, and Jiawei Wan, for all the help extended to me during my time in the group led by Prof. Dr. Eva Gutheil. I am also grateful to Ellen Vogel for her timely help with all administrative matters. Additionally, I would like to thank Cederbaum Astrid and Felicitas Hirsch for their administrative support after Ellen Vogel left. Special thanks also go to Manfred Trunk for providing all the required technical support.

I owe an invaluable debt to all the staff of Heidelberg University for their support, suggestions, and cooperation, without which I could not have executed this project. I am thankful to the Interdisciplinary Center for Scientific Computing (IWR) and Heidelberg University for providing me with all the necessary facilities. Special thanks go to a never long enough list of individuals: Raphaela Antimisaris, Dr. Ali Farnod, Dr. Haiwen Ge, Prof. Dr. Roland Herzog, Prof. Dr. Dr. Hans-Jörg Himmel, Prof. Dr. Gerald Linti, Chiara Rottaro, Prof. Dr. Filip Sadlo, Susanne Sandbrink, Dr. Chen Song, Prof. Dr. Michael Wink, and Dr. Michael Winckler. Without their encouragement and help, this dissertation may not have been possible.

I sincerely thank Prof. Dr.-Ing. Irenäus Wlokas and Monika Nanjaiah at Universität Duisburg-Essen for providing the chemical kinetics of titanium(IV) isopropoxide/p-xylene. I also acknowledge with gratitude the temperature-dependent thermophysical properties of water provided by Dr. Michael Kleiber at Thyssenkrupp Uhde GmbH. I deeply appreciate the fruitful discussions with Prof. Dr. Boshu He from Beijing Jiaotong University, China; Prof. Dr. Junfeng Yang from the University of Leeds, UK. Their insights and expertise have been invaluable to my research. I am grateful to all the collaborators and co-authors of my

research papers for their valuable expertise, which has significantly enhanced the quality of my research work. Additionally, I would like to thank all the members of the DFG priority program SPP 1980 for their valuable input.

I wish to express my sincere thanks to the panel members for being part of the evaluation process. I am deeply grateful to Prof. Dr. Oriol Vendrell and Prof. Dr. Ing. Andreas Kempf for agreeing to be the reviewer. Additionally, I am indebted to Dr. Maximilian Herrmann and Chatrchyan Viktoria for their meticulous translation of the abstract into German, and to Dr. Niklas Jüngst and Robin Kugler for their thorough review. Also, I deeply thank Dr. Praveen Narasu and Jiawei Wan for thoroughly reviewing this dissertation.

I extend my deepest gratitude to my beloved family members, especially my mother (Zuyu Ye) and my father (Shouyuan Ying), for their constant support and endless love. I am forever grateful to them for their vital roles as advisors, mentors, teachers, and constant motivators throughout the entirety of my PhD study. I would also like to express special thanks to my girlfriend (Zixing Tian), who has been a tremendous source of motivation and support over the past five years. I deeply miss my grandmother (Aizhen Ye), who has unfortunately been suffering from a serious illness in the past few months. Although my grandfather (Qijia Ying) passed away and I was unable to bid him farewell after moving to Germany, I am accompanied by his spirit. It is their love and support that have inspired me to overcome every challenge and grow stronger.

Finally, I would like to express my sincere gratitude to my dearest friends for their unwavering support and assistance. Their care and dedication ensured that I was never alone during the tough times, significantly contributing to my ability to thrive in Germany. My friends truly became my family, far from home.

Last but not least, I am immensely grateful for the financial support provided by the DFG through the priority program SPP 1980, grant GU 255/13-2, and HGS-MathComp.

NATURWISSENSCHAFTLICH-MATHEMATISCHE GESAMTFAKULTÄT

COMBINED FACULTY OF NATURAL SCIENCES AND MATHEMATICS

RUPRECHT-KARLS-
UNIVERSITÄT
HEIDELBERG

Eidesstattliche Versicherung gemäß § 8 der Promotionsordnung für die Naturwissenschaftlich-Mathematische Gesamtfakultät der Universität Heidelberg / Sworn Affidavit according to § 8 of the doctoral degree regulations of the Combined Faculty of Natural Sciences and Mathematics

1. Bei der eingereichten Dissertation zu dem Thema / The thesis I have submitted entitled
   Numerical Simulation of Monocomponent and Multicomponent Droplet Spray Flames in the Counterflow Configuration
   handelt es sich um meine eigenständig erbrachte Leistung / is my own work.

2. Ich habe nur die angegebenen Quellen und Hilfsmittel benutzt und mich keiner unzulässigen Hilfe Dritter bedient. Insbesondere habe ich wörtlich oder sinngemäß aus anderen Werken übernommene Inhalte als solche kenntlich gemacht. / I have only used the sources indicated and have not made unauthorised use of services of a third party. Where the work of others has been quoted or reproduced, the source is always given.

3. Die Arbeit oder Teile davon habe ich wie folgt/bislang nicht[1)] an einer Hochschule des In- oder Auslands als Bestandteil einer Prüfungs- oder Qualifikationsleistung vorgelegt. / I have not yet/have already[1)] presented this thesis or parts thereof to a university as part of an examination or degree.

   Titel der Arbeit / Title of the thesis:

   Hochschule und Jahr / University and year:

   Art der Prüfungs- oder Qualifikationsleistung / Type of examination or degree:

4. Die Richtigkeit der vorstehenden Erklärungen bestätige ich. / I confirm that the declarations made above are correct.

5. Die Bedeutung der eidesstattlichen Versicherung und die strafrechtlichen Folgen einer unrichtigen oder unvollständigen eidesstattlichen Versicherung sind mir bekannt. / I am aware of the importance of a sworn affidavit and the criminal prosecution in case of a false or incomplete affidavit

Ich versichere an Eides statt, dass ich nach bestem Wissen die reine Wahrheit erklärt und nichts verschwiegen habe. / I affirm that the above is the absolute truth to the best of my knowledge and that I have not concealed anything.

Heidelberg, 05/06/2024 ..... Zhaoping Ying

Ort und Datum / Place and date — Unterschrift / Signature

[1)] Nicht Zutreffendes streichen. Bei Bejahung sind anzugeben: der Titel der andernorts vorgelegten Arbeit, die Hochschule, das Jahr der Vorlage und die Art der Prüfungs- oder Qualifikationsleistung. / Please cross out what is not applicable. If applicable, please provide: the title of the thesis that was presented elsewhere, the name of the university, the year of presentation and the type of examination or degree.

The German text is legally binding.